# Effect of piezoelectric strain on the magnetic properties of Pt/Co thin films

Philippa Mary Shepley

School of Physics and Astronomy

University of Leeds

Submitted in accordance with the requirements for the degree of

*Doctor of Philosophy*

August 2015

# DON'T PANIC [1]

## Intellectual Property Statement

The candidate confirms that the work submitted is her own, except where work which has formed part of jointly authored publications has been included. The contribution of the candidate and the other authors to this work has been explicitly indicated below. The candidate confirms that appropriate credit has been given within the thesis where reference has been made to the work of others.



Work from the following jointly authored publication is presented in chapters four and six of this thesis:
P.M. Shepley, A.W. Rushforth, M. Wang, G. Burnell, T. A. Moore. "Modification of perpendicular magnetic anisotropy and domain wall velocity in Pt/Co/Pt by voltage-induced strain." *Scientific Reports* **5**, 7921 (2015). **Work attributable to candidate:** Experimental measurements, analysis of data and preparation of manuscript. **Work attributable to others:** A.W. Rushforth, M. Wang, G. Burnell and T. A. Moore discussed results and A.W. Rushforth and T.A. Moore edited the manuscript.

# Acknowledgements

As my supervisors, Dr Tom Moore and Dr Gavin Burnell have contributed many ideas to this project. I am grateful to Tom for giving me the opportunity to do this research in the first place, for many discussions, for help with interpreting results, and for helping me to get the most out of my project. Thank you for always being ready to talk through problems with me, whilst giving me the freedom to take control of my research and pursue my ideas. I'd like to thank Gavin for his advice on experiments and the world of academia, for introducing me to Python and for writing a lot of the software that I've used for MR measurements. Resistance to the One Code is futile.

Thanks go to Dr Andrew Rushforth from the University of Nottingham, who gave me much needed guidance on using piezoelectric transducers, helped with patterning Hall bars and contributed to interpreting the results, particularly at the start of the project. I owe a lot of what I now know about MOKE to Dr Mannan Ali: thank you for training me in the lab and teaching me so much about many of the experimental techniques I've used. Thank you to the technical staff in Physics who've made, fixed and maintained equipment. I also want to thank my transfer assessor, Professor Chris Marrows, for useful discussions. I want to thank Aleš, Kowsar, Risalat and Adam for our "DMI club" sessions over the past few months.

I owe a great deal of thanks to many others in the Leeds CM group who have help me to learn new techniques and been a great source of ideas for solving problems or for thinking about results in new ways. The group has been great environment to work in, and I've gained and learned about so much more than just the experimental skills and physics I've needed for my project. I want to thank my friends in the CM group for making the last four years enjoyable. Thank you all for the group trips, Friday nights in the Fenton, lunchtime crosswords and tea breaks. I want to especially thank my office-mate Nathan, and Rowan, May, Joe, Priya and Sophie, who have especially shared PhD trials and tribulations with me. The solution to many a problem has come at the bottom of a mug of tea, and for this I want to thank the people who've given advice and drank the tea with me, and the producers and blenders of the tea (Yorkshire Tea in particular). I'm not sure I'd have got this far without you!

Last but not least, a few words of thanks to my family, who've patiently listened to me going on about tiny magnets for four years. To my parents, Fliss and Rob: thank you for encouraging me, for passing on your sense of curiosity about the world and for your love and support. To my sister, Rosie: thank you for being my best friend and for always being there, regardless of distance. To my partner, Aaron: thank you for your love, patience and understanding, and for sharing the highs and lows with me.

# Abstract

The effect of strain from piezoelectric transducers on the perpendicular magnetic anisotropy (PMA), magnetic domain wall energy and domain wall creep motion of Pt/Co thin films has been investigated. Thin films of Pt/Co/X, where X is Pt, Ir/Pt or Ir, were deposited by sputtering onto thin glass substrates, which were bonded to piezoelectric transducers. Applying a voltage of up to 150 $V$ to the transducers caused tensile out-of-plane strain in the Pt/Co/X thin films for the case of biaxial transducers, and a uniaxial in-plane tensile strain in the case of uniaxial transducers. Measurements of magnetic anisotropy showed that tensile out-of-plane strain lowered the PMA of Pt/Co/Pt, while uniaxial in-plane strain induced an in-plane magnetic anisotropy.

To understand the effect of strain on the magnetic domain walls in Pt/Co/X thin films, the Dzyaloshinskii-Moriya interaction (DMI) field was measured. The DMI field varied between Pt/Co/X films, from close to zero in some Pt/Co/Pt films, indicating domain walls with a Bloch structure, to values large enough to give domain walls a strong Néel component. The DMI field did not change significantly under tensile out-of-plane strain, meaning changes in the domain wall energy were due only to the change in PMA.

Magnetic hysteresis loops of Pt/Co/X thin films showed that the coercive field was reduced by the change in PMA under strain. The magnetisation reversal was investigated further by measurements of the velocity of magnetic domain walls in the creep regime. The domain wall velocity increased by between 10 and 90 % under tensile out-of-plane strain. No measurable changes were seen in the pinning energy of the films, showing that while the height of the barrier to magnetisation reversal is reduced, the anisotropy energy landscape is not distorted significantly. The highest changes in domain wall velocity were seen in the Pt/Co/Pt films with very low DMI fields, from which it is concluded that the creep velocity of Bloch domain walls is more sensitive to strain than that of walls with a Néel component.

# Contents

# Abbreviations

| | |
|---|---|
| bcc | Body centred cubic |
| BTO | Barium titanate |
| DMI | Dzyaloshinskii-Moriya interaction |
| EHE | Extraordinary Hall effect |
| fcc | Face centred cubic |
| hcp | Hexagonal close packed |
| IP | In-plane |
| LHS | Left-hand side |
| MOKE | Magneto-Optical Kerr effect |
| OOP | Out-of-plane |
| PMA | Perpendicular magnetic anisotropy |
| PMN-PT | Lead magnesium niobate-lead titanate |
| PZT | Lead zirconate titanate |
| RHS | Right-hand side |
| SQUID | Superconducting quantum interference device |
| VSM | Vibrating sample magnetometry |
| XRR | X-ray reflectivity |

# Chapter 1

Introduction

Thin films with perpendicular magnetic anisotropy (PMA) have proved interesting both from the perspective of technological applications and for fundamental physics. Pt/Co multilayers have been the system of choice for many studies, showing a high level of versatility, particularly for studying domain wall creep motion. Mechanically coupling thin films to piezoelectric materials offers a way of reversibly straining the film and changing the material properties. This work exploits the dependence of the magnetic anisotropy of Co on strain from a piezoelectric transducer. Tuning the PMA gives control of the structure and energy of domain walls in Pt/Co, which modifies the velocity in the creep regime.

## 1.1 Applications of perpendicular magnetic anisotropy

Materials with PMA have been used for technological applications in data storage devices. Out-of-plane anisotropy tends to be strong, so that the energy barrier to magnetisation is high and data encoded as up and down magnetisation states has good stability. High anisotropy also leads to narrow domain walls, which allows for higher storage density, whether in hard disk drive platters [2] or domain wall racetrack devices [3], where PMA materials also promise efficient current-induced domain wall motion [4].

The high anisotropy of PMA materials presents challenges as well as benefits. To write data, magnetic states must be reversed, requiring large amounts of energy from switching fields or currents to overcome the high anisotropy energy barrier. For technological applications that use current-induced domain wall motion, a large PMA limits the threshold current density [5]. Controlling magnetisation reversal or modifying PMA using electric fields provides a route to lowering the energy barrier to magnetisation reversal, reducing unwanted heating effects and lowering energy use [6].

## 1.2 Magnetisation reversal and domain walls

In a film of ultra-thin Pt/Co with PMA, magnetisation reversal usually takes place by nucleation of very few reverse domains, with domain walls separating the reversed and unreversed regions. Applying a magnetic field provides the driving force to move the domain walls and increase the size of the reversed regions. Below a critical field, the domain walls act as elastic strings that can become pinned by peaks in the magnetic anisotropy energy landscape of the film. Fluctuations in thermal energy allow the domain walls to overcome

the pinning barriers. The velocity of a magnetic domain wall in this case is described by the creep law.

Creep occurs in many physical systems, and is defined as a one dimensional elastic interface driven through a two dimensional weakly disordered landscape [7]. At finite temperature, magnetic domain walls in thin films exhibit creep motion below a driving force threshold, and have become a model system for studying the phenomenon [8]. The motion of magnetic domain walls can be driven by magnetic field [9] or electric current [5] and spans orders of magnitude in velocity, from the low velocity creep regime where walls can move at just a few $\mu m/s$ to the flow regime where velocities are measured in $m/s$.

While magnetic domain walls are generally modelled as one-dimensional when they are in motion, these interfaces between domains do, in fact, have a width and spin structure. Conventionally, the energy and structure of domain walls in PMA thin films have been determined by the strength of the magnetic anisotropy energy, the film thickness, and the exchange stiffness. More recently, a phenomenon known as the Dzyaloshinskii-Moriya interaction (DMI) [10; 11] has been of interest in relation to domain walls [12–16]. The DMI is a chiral exchange favouring non-collinear spin arrangements, which has consequences for the energy and structure of domain walls in PMA thin films.

## 1.3 Pt/Co thin films

PMA in Pt/Co thin films was first demonstrated in sputtered Pt/Co multilayers at the end of the 1980s [17; 18]. Since then, Pt/Co multilayers have become important as a PMA system. The PMA of Pt/Co emerges from orbital hybridisation and spin-orbit coupling at the interfaces [19]. The interfaces in Pt/Co/Pt are not symmetric and contribute differently to the PMA, which may be due to differences in the degree of intermixing at the top and bottom Pt interfaces [20]. Theoretical simulations of the density of states of Pt/Co predict that strain modifies the PMA [21]. The theoretical study shows that the PMA increases as the interatomic in-plane distances increase.

The first experimental demonstration of domain wall creep motion used Pt/Co/Pt trilayers [8], and they have continued to be an ideal system for studying domain wall dynamics in the creep regime [9; 22–27]. The behaviour of a domain wall in the creep regime is modelled as a one-dimensional elastic string moving through a two-dimensional energy landscape [7; 8]. Pt/Co/Pt trilayers with ultra-thin magnetic Co provide a good system for realising this model. Pt/Co thin films also offer great tunability. The strength of the PMA and

the domain wall pinning energy landscape, along with other phenomena such as the DMI [16; 20; 28], can be engineered by controlling parameters such as the layer thicknesses or repeats [23; 29], the growth temperatures and pressures [29–31], the materials used for capping or interlayers [16; 28], or by using implantation of charged ions [32]. These methods already provide a great degree of control over Pt/Co, however the properties are set by growth conditions or are irreversible. Using piezoelectric materials to induce strain opens the way for reversible tuning of some of the properties of Pt/Co thin films.

## 1.4 Voltage control of magnets via strain

Multiferroic heterostructures allow the properties of a ferromagnetic thin film to be controlled by a voltage, often with strain as an intermediary. Ferromagnets have an electric analogue in the form of ferroelectric materials, which can hold a remanent polarisation. Many ferroelectrics are also piezoelectric: a voltage develops across them when they are deformed and, conversely, applying a voltage will induce strain. Ferroelectric materials often employed in multiferroic heterostructures include barium titanate (BTO), lead magnesium niobate-lead titanate (PMN-PT) and lead zirconate titanate (PZT), which is often used in transducers. Making layered structures of materials with different ferroic ordering allows a wider range of properties to be exploited. Reviews on multiferroics and multiferroic heterostructures [33; 34] give an overview of the range of approaches and coupling mechanisms employed. Strain control has been used to modify magnetic properties in a range of magnetic materials, and while the majority of work in multiferroic heterostructures has used magnets with in-plane anisotropy, strain control has also been demonstrated in a few examples of systems with PMA.

### 1.4.1 Ferromagnets with in-plane magnetic anisotropy under piezoelectric strain

Magnetic anisotropy and domain walls in in-plane magnetic materials can be manipulated by strain. BTO exhibits a ferroelectric domain structure, which alters when an electric field is applied. The changing domain pattern is associated with changes in the lattice parameters of the material, thus a ferromagnet coupled to the BTO can be strained in order to change magnetic anisotropy [35]. Applying an electric field to BTO with CoFe grown on top, such that the stripe domains in the ferroelectric induced the same pattern

in the ferromagnetic domains, caused rotation of the magnetisation, allowing removal and reinstatement of the magnetic domain pattern and movement of domain walls [36]. Control of domain wall motion via strain coupling has also been observed in FeGa on BTO [37] and in FeGa coupled to piezoelectric transducers [38]. The magnetisation of spin valves grown on a piezoelectric layer was controlled with electric fields via strain. By injecting a single domain wall it was found that straining the spin valve increased the coercive field and propagation field of the free layer [39]. Since the structure behaved like a domain wall gate, the concept could be used to construct low power magnetic logic [39], or to pin and de-pin DWs in racetrack memory [3].

Switching of small magnetic elements can be achieved using strain. Memory devices using multiferric heterostructures with magnetic islands at the intersections of a grid of ferroelectric material have been proposed [40]. Ni nanostructures grown on PMN-PT can be switched by $90^o$ through applied strain [41]. Strain control of small magnetic elements may be useful for multiferroic data storage applications.

Progress has been made towards non-volatile control of magnetisation states in in-plane magnetic systems. Electric fields applied to a PMN-PT/CoFeB structure can cause magnetisation changes with loop-shaped hysteresis that remains after the field is removed [42]. Non-volatile and reversible changes to in-plane magnetic anisotropy have been found in PMN-PT/Ni, when the piezoelectric is operated in a regime with a remanent strain-state [43]. Non-volatile systems where a strain-induced state persists without continued voltage input to the ferroelectric could find applications as memory and data storage devices.

### 1.4.2 Ferromagnets with perpendicular magnetic anisotropy under piezoelectric strain

Some of the multiferroic heterostructures studied have been engineered to have PMA. CoPd alloys grown on PMN-PT exhibited changes in the shapes of hysteresis loops when voltage was applied [44], show that straining the CoPd reduced its PMA. The nucleation and coercive fields measured from hysteresis loops have also been shown to change in Pd/Co/CoFeB structures on PZT under strain [39]. Changes in domain wall motion have been measured in ferromagnetic semiconductors on piezoelectric transducers. In (Ga,Mn)(As,P) with PMA at 90 $K$ [45], the mobility of current-driven domain walls was found to vary by 500 %. These results show clear changes in the properties of PMA systems under strain from piezoelectric materials. Given their widespread use as a model PMA system, particularly for domain wall

motion studies, Pt/Co thin films have been chosen for this work. Piezoelectric transducers provide a convenient route of inducing strain in order to tune the PMA of Pt/Co and to allow for direct measurements of modifications to domain wall motion.

## 1.5 Thesis overview

This thesis describes experiments which measure magnetic properties of Pt/Co thin films and how those properties change when strain is applied from a piezoelectric transducer. This chapter has set out the motivation for this work along with the current state-of-the-art. The following chapters will expand on this background by explaining the relevant theoretical concepts (Chapter 2) and the experimental methods (Chapter 3) required for this work. Chapter 4 describes the magnetic anisotropy measurements and results of the change in magnetic anisotropy in Pt/Co/Pt under strain from biaxial and uniaxial piezoelectric transducers. Chapter 5 gives details of the DMI measurements on Pt/Co thin films and investigates the effect of strain on the DMI field. Chapter 6 shows how domain wall motion in the creep regime is modified by strain, and explains the changes in the context of the domain wall energy and structure. A summary of these results along with suggestions for how the project might continue are given in Chapter 7.

# Chapter 2

Theoretical background

## 2.1 Introduction

In this chapter the physical concepts that underpin this work will be outlined. The concept of magnetic anisotropy, which is central to the experimental results presented in later chapters will be discussed, with particular emphasis on magnetoelastic anisotropy and the magnetocrystalline anisotropy that gives rise to PMA in Pt/Co thin films. The structure and energy of domain walls, along with domain wall motion in the creep regime will be described.

## 2.2 Magnetic anisotropy

Magnetic materials are often easier to magnetise in some directions than others; less field needs to be applied to saturate a magnet along an 'easy axis' than along a 'hard axis'. This phenomenon is referred to as magnetic anisotropy.

The simplest form this takes is uniaxial anisotropy, where there is a single axis along which the magnetisation preferentially points, and an additional energy cost for magnetisation pointing in any other direction. The angular dependence of the magnetic anisotropy energy density of such a system is given by

$$E_k = K_1 \sin^2\theta + K_2 \sin^4\theta + K_3 \sin^6\theta + ..., \tag{2.1}$$

where $K_1$,$K_2$ and $K_3$ are the first, second and third order anisotropy constants and $\theta$ is the angle of the magnetisation from an appropriate crystallographic axis or the normal of a thin film [46] (see Figure 2.1a). Limiting the expression to the lowest order term gives

$$E_k = K \sin^2\theta, \tag{2.2}$$

which is sufficient to describe a uniaxial system with single easy axis ($K > 0$) or easy plane ($K < 0$). Higher order terms can be included to describe other uniaxial magnetic energy landscapes such as easy cone anisotropy ($K_1 < 0$, $K_2 > K_1/2$). Figure 2.1 shows the shapes of the magnetic energy landscapes for isotropic (Figure 2.1b) and uniaxial systems (Figures 2.1 c and d). A more general form of the energy density can be used to describe systems with a principal anisotropy axis out-of-plane ($K_z$) and an additional in-plane anisotropy ($K_{IP}$)

$$E_k = K_z \sin^2\theta + K_{IP} \sin^2\theta \cos(2\phi), \tag{2.3}$$

where $\phi$ is the in-plane angle (see Figure 2.1a).

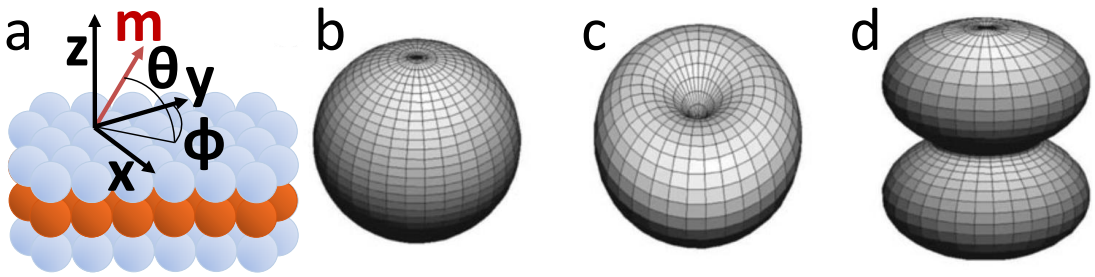


**Figure 2.1:** a) Schematic showing the geometry of PMA in a thin film (e.g. Pt/Co/Pt). Magnetic anisotropy energy landscapes for b) an isotropic system, c) a single easy axis and d) an easy plane. Parts b,c and d of this figure are reproduced from Ref. [46].

Contributions to magnetic anisotropy can come from a number of sources which include: the geometry of the sample (shape anisotropy), the crystal structure (magnetocrystalline anisotropy) and strain in the material (magnetoelastic anisotropy).

Shape anisotropy comes from the magnetic dipolar interaction. For most thin film magnets, this results in the magnetisation preferentially lying in the plane of the film. Magnetocrystalline anisotropy relates to the symmetry of the crystal structure in a material and its physical origin is the interaction of the crystal field and the spin orbit interaction, which couples the spin and orbital motion of electrons. For bulk hcp cobalt, the magnetisation tends to align along the c-axis, giving a uniaxial anisotropy as described by Equation 2.2. For a material with a cubic structure, such as iron, the anisotropy takes on a cubic symmetry with more than one easy axis.

### 2.2.1 Magnetoelastic anisotropy and magnetostriction

The elastic energy density can be expressed as

$$E_{el} = \frac{-\lambda\varepsilon Y}{2}(3\cos^2\alpha - 1) + \frac{\varepsilon^2 Y}{2} \tag{2.4}$$

for a polycrystalline material. The saturation magnetostriction constant is given by $\lambda$, $\varepsilon$ is the strain, $Y$ is the Young's modulus and $\alpha$ is the angle between the tensile strain axis and the magnetisation. Setting $\alpha = \theta$ (i.e. the easy axis and strain axis are aligned) and equating the uniaxial anisotropy energy given in Equation 2.2 and the angular dependence of the elastic energy gives the elastic contribution to the magnetic anisotropy energy:

$$K\sin^2\theta = \frac{-\lambda\varepsilon Y}{2}(3\cos^2\alpha - 1),$$

which reduces to

$$K_{el} = \frac{3}{2}\lambda\varepsilon Y. \tag{2.5}$$

This is the additional contribution to the magnetic anisotropy constant due to strain [47]. The effect is the inverse of magnetostriction, where magnetising a material along a certain axis distorts the crystal field, causing a deformation. Minimising the elastic energy (Equation 2.4) with respect to strain and setting $\alpha = 0$ gives the spontaneous magnetostriction $\varepsilon = \lambda$ along the magnetisation axis. A magnetostrictive material will extend in the direction of magnetisation if $\lambda$ is positive, or contract if $\lambda$ is negative. Similarly, following from Equation 2.5, an applied tensile strain will increase the magnetic anisotropy along the strain direction in a material with a positive $\lambda$, and reduce the anisotropy for a material with a negative $\lambda$ [46]. The magnetostriction constant is generally of the order of $10^{-5}$ (-50 $\times 10^{-6}$ for Co). The spontaneous strain along the direction of magnetisation will therefore be small compared to the applied strain from piezoelectric transducers ($\sim$1-10 $\times 10^{-4}$).

### 2.2.2 Perpendicular magnetic anisotropy

Some thin films have an easy axis perpendicular-to-plane, which often emerges from effects at the interfaces. Thin film magnetic anisotropy is sometimes split into volume and interface contributions $K_V$ and $K_S$ with the following expression,

$$K = K_V + \frac{2K_S}{t}, \tag{2.6}$$

where $t$ is the thickness of the magnetic film. $K_V$ contains magnetocrystalline and shape anisotropy contributions, which are generally in-plane. For hcp Co the magnetocrystalline anisotropy, defined from the c-axis, is 0.53 $MJ/m^3$ and the shape anisotropy is $-1.2$ $MJ/m^3$, using the value for bulk saturation magnetisation (see Section 2.2.3). $K_S$ is the surface anisotropy, which can be out-of-plane, depending on the interaction of the crystal field and the spin-orbit coupling [46]. The balance of the surface and volume anisotropies determines the strength and direction of the magnetic anisotropy.

In ultra-thin Co films there is an in-plane anisotropy contribution from the Co volume and a perpendicular anisotropy contribution from the interfaces, which is magnetocrystalline in origin. PMA in thin Co multilayers, often Pt/Co or Pd/Co, has been known for several decades [17; 18] and evidence of strong contributions to PMA from the interfaces has been demonstrated through X-ray magnetic circular dichroism (XMCD) studies [19; 48; 49]. Tight-binding models have been used to determine band structures of thin Co films and

calculate the magnetic anisotropy [21; 50]. These calculations show that hybridisation between Co and non-magnetic layers (Pt, Pd, or Au) along with spin-orbit coupling gives rise to a perpendicular component to magnetic anisotropy at the interface. The spin-orbit coupling in 3d transition metals such as Co is small, so it is treated as a perturbation. The spin-orbit Hamiltonian is $H_{SO} = \xi_{Co}\boldsymbol{L} \cdot \boldsymbol{S}$, where $\xi_{Co}$ is the spin-orbit coupling constant for Co, $\boldsymbol{L}$ is the orbital angular momentum and $\boldsymbol{S}$ is the spin angular momentum [50].

In Pt/Co multilayers, the PMA comes from hybridization of the Co 3d and Pt 5d electron orbitals and spin-orbit coupling at the interfaces [19]. The perpendicular orbital moment of interface Co atoms will be enhanced depending on the positions of certain states relative to the Fermi energy. The hybridisation also modifies the band structure of Pt, resulting in an orbital moment for the interface Pt atoms aligned parallel to the enhanced Co orbital moment, further increasing the PMA [19].

### 2.2.3 Shape anisotropy

Shape anisotropy is the result of the magnetostatic interactions between magnetic dipoles. The long-range nature of magnetostatic interactions means that the macroscopic magnetisation direction has an effect on the energy of a magnet. If the magnetisation is aligned uniformly in a material there will be magnetic charges at the surfaces, which cost dipolar energy given by the shape anisotropy energy density [46]

$$K_{sh} = \frac{\mu_0}{4}(1 - 3N)M_s^2, \tag{2.7}$$

where $\mu_0$ is the vacuum permeability, $N$ is the demagnetising factor and $M_s$ is the saturation magnetisation. For a thin films $N = 1$, giving a shape anisotropy of $-\frac{1}{2}\mu_0 M_s^2$, which is equal to $-1.05\ MJ/m^3$ in a thin film of Co where $M_s$ is the value measured in Chapter 3 ($M_s$ =1.29 $MA/m$), or $-1.2\ MJ/m^3$ using the value for bulk saturation magnetisation of Co ($M_s$ =1.4 $MA/m$). The magnetostatic surface charges in a uniformly magnetised material give rise to a demagnetising field $H_D = -NM_s$, which acts in the opposite direction to the magnetisation.

The energy cost associated with magnetostatic interactions can lead to formation of magnetic domains. Breaking a uniformly magnetised thin film into domains with magnetisation in different directions reduces the demagnetising fields and magnetostatic anisotropy energy. The interfaces between the regions of differently orientated magnetisation are domain walls, which have an associated energy cost. Domain formation is therefore a balance between the magnetostatic anisotropy energy and the domain wall energy.

### 2.2.4 The Stoner-Wohlfarth model

The Stoner-Wohlfarth model gives a simple description of the angular dependence of the energy of a magnetic particle where the magnetisation rotates coherently as if it were one macroscopic spin. The model gives a limited description of hysteresis loops and can be applied in magnetic anisotropy measurements [46]. The Stoner-Wohlfarth energy density is

$$E = K_{eff} \sin^2 \theta - \mu_0 M_s H \cos(\phi_H - \theta). \tag{2.8}$$

The first term is the effective anisotropy constant $K_{eff} = (K_1 - \frac{1}{2}\mu_0 M_s^2)$ comprising the first order anisotropy constant and the demagnetising energy, the second term is the interaction of the applied field $H$ and the magnetisation. The angle from the film normal to the magnetisation is $\theta$, the angle from the film normal to the applied field is $\phi_H$ and $M_s$ is the saturation magnetisation. The shape of hysteresis loops can be derived from the Stoner-Wohlfarth model, where the field needed to rotate and saturate the magnetisation along the hard axis is the anisotropy field [51]

$$H_k = \frac{2K_{eff}}{\mu_0 M_s}. \tag{2.9}$$

The anisotropy field can be measured in a film where PMA dominates ($K_{eff} > 0$) by first saturating the magnetisation along the easy axis and then applying a field along the hard axis. So long as the magnetisation rotates coherently, the Stoner-Wohlfarth model can be applied to measure $H_k$. The experimental details of the measurement are described in Chapter 4.

## 2.3 Magnetisation reversal in perpendicular thin films

In a thin film with PMA, magnetisation reversal takes place by nucleation of a few reverse domains, with domain walls separating the reversed and unreversed regions, followed by expansion of the reversed domains. Magnetisation reversal can be studied by sweeping the magnetic field to give a hysteresis loop or by nucleating a reverse domain then applying a field pulse to move a domain wall and measuring its velocity. Magnetisation reversal in a thin film can be characterised by a number of features: the nucleation field is where domains nucleate and the magnetisation starts to reverse, the remanence is the proportion of the saturation magnetisation remaining when no field is applied, and the coercive field is the field at which the average magnetisation in the film is zero. Once reverse domains have

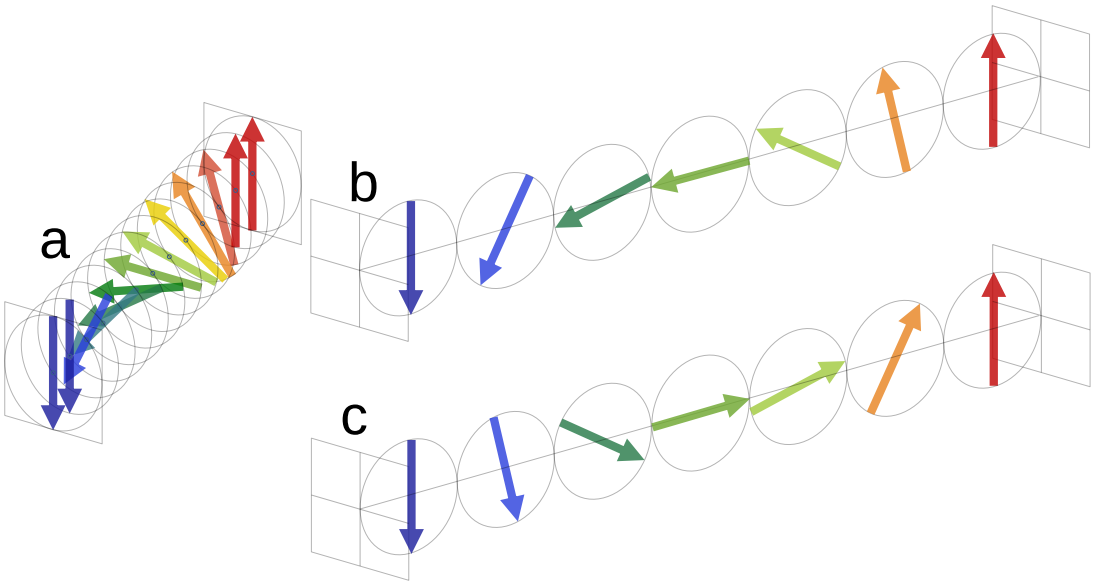


**Figure 2.2:** Diagram showing the structure of a) right-handed Bloch, b) left handed Néel and c) right handed Néel domain walls in PMA thin films.

nucleated in a PMA thin film, a propagation field must be applied in order to continue the motion of domain walls.

### 2.3.1 Domain walls

A domain wall is the region between two domains of different magnetisation direction. In PMA thin films these generally take the form of $180^o$ walls where the orientation of moments changes smoothly between positive and negative out-of-plane magnetisation. Figure 2.2 shows the two forms these walls take: Bloch and Néel.

An understanding of domain walls starts with the magnetic free energy in a uniaxial system, which takes into account the exchange stiffness $A$, the saturation magnetisation, the uniaxial anisotropy energy density and the demagnetising field. Starting from considering the parameters (and their dimensions) that contribute to magnetic free energy, a length emerges from the exchange stiffness and the effective magnetic anisotropy [13] to give the wall-width parameter

$$\delta = \sqrt{\frac{A}{K_{eff}}}. \tag{2.10}$$

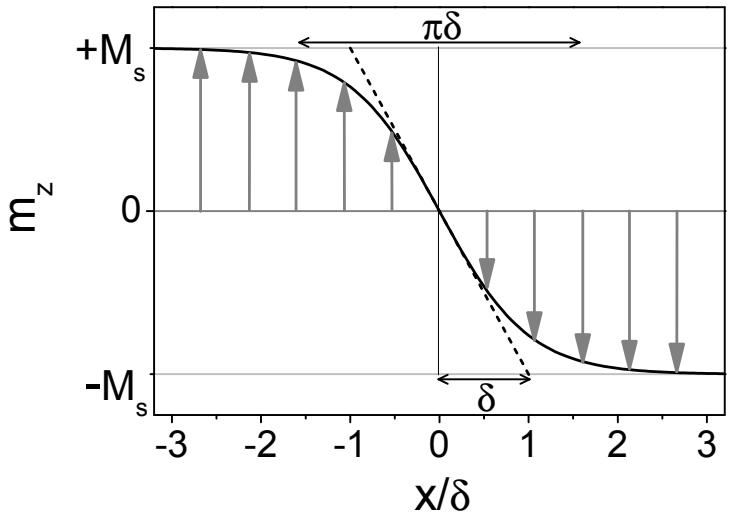


**Figure 2.3:** Plot showing the variation of out-of-plane magnetisation and width parameters of a Bloch domain wall [46].

The actual width of a Bloch wall is better represented by the Bloch wall width

$$\delta_B = \pi\sqrt{\frac{A}{K_{eff}}}. \tag{2.11}$$

Figure 2.3 shows how the out-of-plane component of magnetisation varies through a domain wall $m_z(x/\delta) = -M_s \tanh(x)$ [46], and how this relates to the widths given in Equations 2.10 and 2.11.

The energy density of a Bloch wall is

$$\gamma = 4\sqrt{AK_{eff}}. \tag{2.12}$$

The width and energy of a Bloch wall are determined by the relative sizes of the exchange stiffness and the magnetic anisotropy. The exchange stiffness is related to the exchange energy

$$E_{ex} = -\tfrac{1}{2}\sum_{ij} J_{ij}\boldsymbol{s}_i\cdot\boldsymbol{s}_j = \int A(\nabla \boldsymbol{s})^2 dV, \tag{2.13}$$

where $\boldsymbol{s}_i$ and $\boldsymbol{s}_j$ are adjacent spins, $\boldsymbol{s} = \boldsymbol{M}/M_s$ and $J_{ij}$ is the interatomic exchange constant. The exchange makes magnetic inhomogeneities $\nabla\boldsymbol{s}$, such as domain walls, energetically unfavourable. This has the effect of widening the wall to reduce the angle between adjacent spins. The effect of the anisotropy is to align spins along a certain axis (with no preference to pointing either positive or negative), so a large anisotropy will make a domain

wall narrower to reduce the spins pointing along different axes. This competes with the effect of exchange on the wall width, so further increases the domain wall energy.

### 2.3.2 Chirality in domain walls

Domain walls are chiral structures that can be left handed or right handed. Bloch walls tend to contain sections of both chiralities, separated by so-called Bloch points, although exceptions have been demonstrated where chiral Bloch walls are possible [52]. Néel walls always have a chirality, and are magnetically charged ($\boldsymbol{\nabla} \cdot \boldsymbol{m} \neq 0$). The demagnetising energy associated with Néel walls means that Bloch walls tend to be favoured [13]. This energy is given by the shape anisotropy constant

$$K_D = \tfrac{1}{2}\mu_0 M_s^2 N, \tag{2.14}$$

where $N$ is the wall's demagnetising factor

$$N = \frac{4t \ln 2}{\pi \delta}, \tag{2.15}$$

which depends on the thickness of the magnetic material $t$ [13; 53]. This means that the energy penalty for Néel walls is less for thinner films and lower saturation magnetisation. There is another phenomenon, the Dzyaloshinskii-Moriya interaction, which is now known to affect the domain wall structure and make Néel walls more favourable [12–14].

### 2.3.3 The Dzyaloshinskii-Moriya interaction and domain wall energy

The Dzyaloshinskii-Moriya interaction (DMI) is an anisotropic exchange interaction which, unlike the exchange term in Equation 2.13, gives rise to more complex spin structures by favouring orthogonal alignment of spins [54]. The DMI exchange energy is given by

$$\boldsymbol{E}_{DM} = -\tfrac{1}{2}\sum_{ij} \boldsymbol{D} \cdot \boldsymbol{s}_i \times \boldsymbol{s}_j, \tag{2.16}$$

where $\boldsymbol{s}_i$ and $\boldsymbol{s}_j$ are adjacent spins, and $\boldsymbol{D}$ is the DMI vector. The DMI has been known for some time as the mechanism by which certain magnetic phases arise [10; 11; 55], but its relevance for domain walls in thin films has been recognised more recently [12; 14; 56].

The DMI depends on the spin-orbit interaction, and emerges in magnetic thin film systems with ferromagnet-normal metal interfaces which lack inversion symmetry and include materials with significant spin-orbit coupling. Systems where surface induced DMI

has been identified include layers of Fe on a W (110) surface [12], [Co/Ni] multilayers on Pt (111) surfaces and Pt(111) with Ir interlayers [14], and Pt/Co/Pt [15; 16; 28; 57] and Pt/Co/Ir tri-layers [16]. In perpendicular thin films, the DMI has the effect of an in-plane field $H_{DMI} = \pi D/(2\mu_0 M_s \delta)$ (with D $= |\boldsymbol{D}|$ giving the strength of the DMI) acting within the wall, which works to overcome the shape anisotropy favouring Bloch walls and make Néel walls more favourable [13; 14]. Taking the DMI field and an applied in-plane field $H_x$ into account, the energy of a domain wall is given by

$$\gamma_{DW}(H_x, \psi) = \gamma + 2K_D\delta\cos^2\psi - \pi\delta\mu_0 M_s(H_x + H_{DMI})\cos\psi, \tag{2.17}$$

where $\psi$ is the in-plane angle of the magnetisation from the x-direction and $\gamma$ is the Bloch wall energy given in Equation 2.12. This gives two different energies depending whether the in-plane fields are sufficient to make the domain wall fully Néel, or if there is still some Bloch component. For a DMI constant $D > 4\delta K_D/\pi$ the wall takes the Néel form with an energy of

$$\gamma_{NW} = \gamma + 2K_D\delta - \pi\delta\mu_0 M_s|H_x + H_{DMI}|, \tag{2.18}$$

and for a DMI constant $D < 4\delta K_D/\pi$ the wall can be intermediate, or Bloch if $H_x + H_{DMI} = 0$, and has an energy of

$$\gamma_{BNW} = \gamma - \frac{\delta(\pi\mu_0 M_s)^2}{8K_D}(H_x + H_{DMI})^2. \tag{2.19}$$

The transition to a Néel wall can also be given in terms of a critical field of $H_{crit} = |H_x + H_{DMI}| > 4K_D/(\pi\mu_0 M_s)$ [12; 13; 15].

The structure, width and energy of a stationary domain wall depend on a number of competing factors, including anisotropy and exchange energies and applied in-plane fields. During magnetisation reversal in PMA materials, domain walls are moved by applying out-of-plane fields to grow the reversed domains at the expense of domains with the opposite magnetisation.

### 2.3.4 Domain wall motion

Domain wall motion driven by an applied magnetic field proceeds differently depending on the strength of the driving field. Figure 2.4 shows the velocity regimes. At low fields there are the creep [7; 8] and thermally assisted flux flow (TAFF) regimes [9]. These regimes require thermal energy to move domain walls, so only occur above 0 $K$. At higher fields domain wall motion becomes less dependent on thermal energy in the depinning regime,

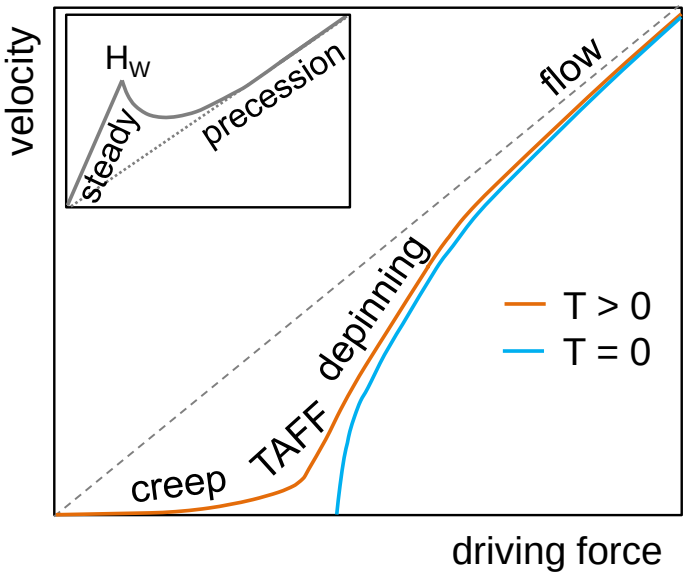


**Figure 2.4:** Domain wall velocity regimes are shown against driving force (magnetic field in the case of magnetic domain walls) [7; 9; 22]. At low fields the motion is thermally assisted and only present at finite temperatures, giving the creep and thermally assisted flux flow (TAFF) regimes. At higher fields domain wall motion becomes less dependent on thermal energy in the depinning regime and eventually shows a linear dependence on the driving field in the flow regime. The inset shows the effect of Walker breakdown, where the magnetisation in the domain wall precesses above the Walker field $H_W$, reducing the velocity.

until it eventually shows a linear dependence on the driving field in the flow regime [7]. There is also a precessional regime above the Walker breakdown field, where the spins in the domain wall precess and the velocity slows [22]. The creep motion regime is studied in this work.

### 2.3.5 Domain wall creep motion

Domain wall creep is a phenomenon that occurs in many physical systems when a one dimensional elastic interface is driven through a two dimensional weakly disordered landscape [7]. Creep motion in ultra thin magnetic films was demonstrated in Pt/Co/Pt in 1998 [8], and this has since provided a model system for studying creep physics [25; 27].

Below a critical field (the depinning field $H_{dep}$) the domain walls act as elastic strings that can become pinned by peaks in the magnetic anisotropy energy landscape of the film,

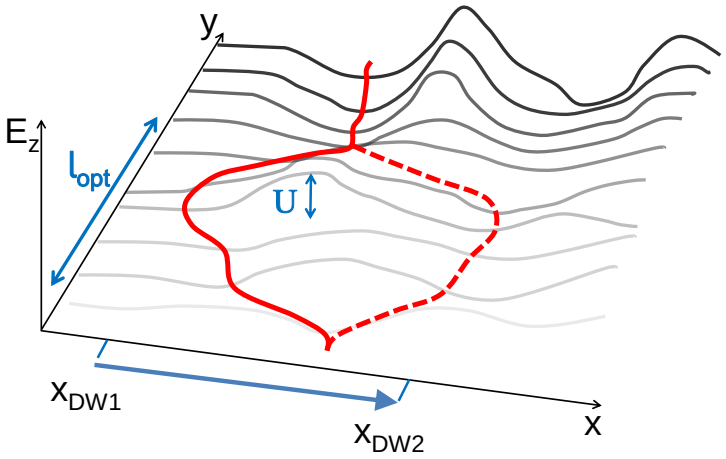


**Figure 2.5:** An energy landscape showing how a domain wall moves from one energy minimum to the next in the creep regime. A small section of domain wall of length $l_{opt}$ moves forward from position $x_{DW1}$ to $x_{DW2}$. The motion is a thermally assisted jump over the local anisotropy energy barrier of height $U$.

described by the pinning energy barrier $U_c$. Fluctuations in thermal energy allow the domain walls to overcome the pinning barriers. The velocity of a magnetic domain wall is described by the creep law [7] as

$$v = v_o \exp\left[-\frac{U_c}{kT}\left(\frac{H_{dep}}{H}\right)^{1/4}\right], \tag{2.20}$$

where kT is the product of Boltzmann's constant and temperature. The numerical prefactor $v_o$ is considered to be proportional to $l_{opt}$ - the lateral length of the small section of wall that undergoes a thermally assisted jump forwards prior to an avalanche where a wider section of wall moves [26; 27]. Figure 2.5 shows a small section of wall moving between two minima in an energy landscape.

The pinning energy $U_c$ gives an average of the energy barriers over the area swept out by a domain wall. It is a measure of the variation of the anisotropy energy across a film and can be used to characterise how magnetically smooth a film is. Typical values of the pinning energy ratio $U_c/kT$ are ~30 - 40 [22], but can be twice that [31] for rougher films or as low as 6 [9] for smooth films with less pinning.

## 2.4 Summary

The theoretical context for understanding the behaviour of the magnetic thin films studied in this work has been introduced. These thin films have a magnetic anisotropy, which can be related to their crystal structure, geometrical shape and mechanical strain. The spin-orbit coupling and crystal field are important for determining the magnetic anisotropy in Pt/Co thin films. Reversal of the magnetisation direction takes place through nucleation of reverse domains and motion of domain walls. The structure and energy associated with domain walls is determined by a balance of exchange, DMI and magnetic anisotropy energy terms. The next chapters describe how some of these parameters can be measured, how they are affected by applied strain, and how strain influences magnetisation reversal.

# Chapter 3

Experimental methods

## 3.1 Introduction

This chapter describes the methods and equipment used to fabricate and characterise the samples studied in this work. Thin films were grown by dc magnetron sputtering. Basic characterisation of the films to determine layer thicknesses, saturation magnetisation and the presence of PMA was carried out using X-ray reflectivity (XRR), superconducting quantum interference device vibrating sample magnetometry (SQUID VSM) and polar magneto-optical Kerr effect (MOKE).

The samples studied in this work were all sputtered thin films of Ta/Pt/Co/X, where X was either Pt, Ir or Ir/Pt. Ta was chosen as a buffer layer because it tends to form in a bcc (111) texture, promoting smooth growth of the first Pt layer as a (111) textured fcc film, which improves the PMA of the stack [19; 58; 59]. Some thin films were patterned into Hall bar structures. Films were mainly deposited onto thin glass cover slips of 150 $\mu m$ thickness, and a few films were deposited onto Si substrates with a thermally oxidised top layer. The thin glass substrates were chosen so that these films could be bonded to piezoelectric transducers and strained. Since glass has no crystalline structure, it should be isotropic and transmit strain equally well for any in-plane axis. The voltage-strain characteristics of the piezoelectric transducers were derived from changes to the resistance of patterned thin films. PMA and domain wall creep velocity were measured as a function of strain using the extraordinary Hall effect (EHE) and Kerr effect imaging respectively.

## 3.2 Sample fabrication and characterisation

### 3.2.1 DC magnetron sputtering

Samples were deposited by dc magnetron sputtering in a system equipped with 8 sources, including two that are suitable for magnetic materials. The base pressure of the sputtering system reaches $10^{-8}$ Torr with use of a cryo-pump and liquid nitrogen shroud. Once the system pressure is sufficiently low, Argon gas is introduced at a partial pressure of $2.4\times10^{-6}$ Torr. A schematic of a magnetron gun is shown in Figure 3.1. The gas is ionised into plasma by an electric field applied between the target and shield and the shape of the plasma is controlled by permanent magnets. Argon ions strike the target, knocking atoms from the material, which then impinge upon the substrate and surrounding areas so that a thin film of the target material builds up [47]. Substrates are attached to a rotatable wheel, which

can be moved between guns containing different target materials to grow multilayer films. Thicknesses of different layers are calibrated to deposition times for each gun by growing bilayer repeats of material and measuring the thickness by X-ray reflectivity.

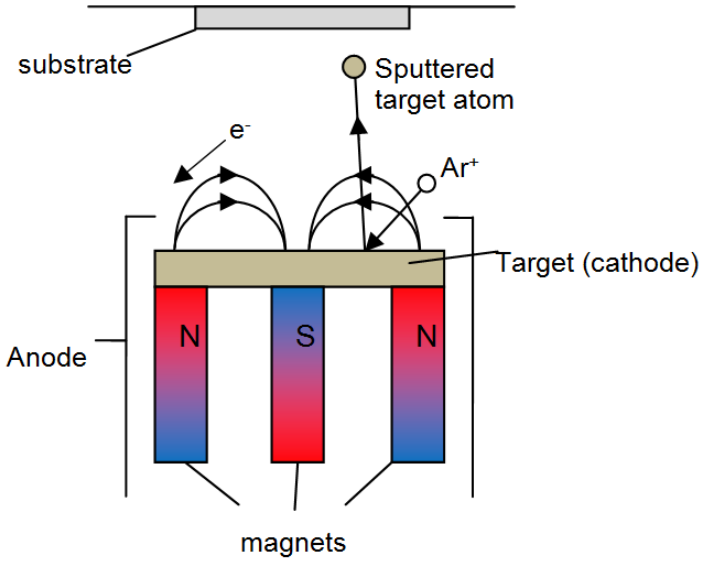


**Figure 3.1:** Schematic showing sputtering of target material onto a substrate using a dc magnetron gun.

### 3.2.2 X-ray reflectivity

X-ray reflectivity (XRR) was used to calibrate the deposition rates of sputtered films. The reflected X-ray intensity is measured over a $2\theta/\omega$ scan at low angles. An example of XRR from a [Co/Pt]×10 multilayer is shown in Figure 3.2. The data from a bilayer repeat multilayer consists of an interference pattern of Bragg peaks with smaller Kiessig fringes between them, which are both due to differences in path lengths of radiation reflected from the interfaces in the multilayer. The position and separation in q space of the Bragg peaks is inversely proportional to the bilayer period of the multilayer. The separation of Kiessig fringes gives the total film thickness, since these fringes are caused by interference between X-rays scattered from the top surface and the interface with the substrate. Knowing the time each layer was deposited for, a rate can be calculated and used to determine the thicknesses of other films.

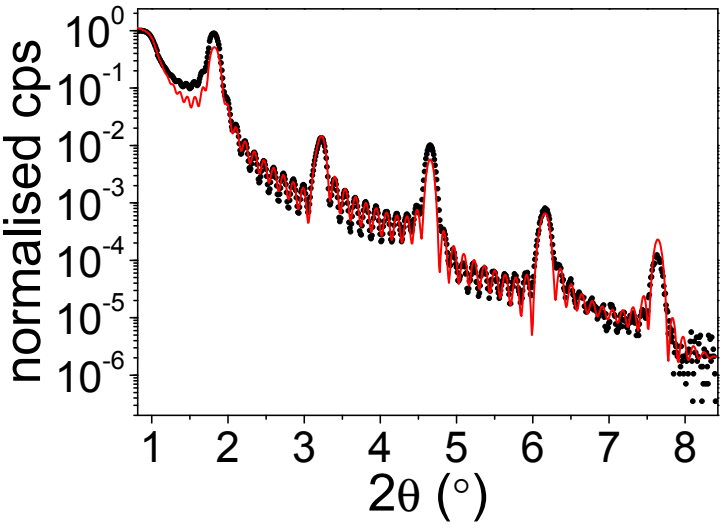


**Figure 3.2:** An example of XRR from a Pt/[Co/Pt]×10 multilayer on a Si/SiOx substrate is shown (black points) along with a fit to the data (red line) perfomed with the GenX fitting algorithm [60]. The thickness of each Pt layer was 3.5 $nm$ and the thickness of each Co layer was 2.3 $nm$. The counts per second (cps), normalised to the highest count rate around the critical edge, are shown on a logarithmic scale.

### 3.2.3 Patterned films

Some of the thin films were patterned into Hall bar structures by optical lithography and lift-off for experiments requiring electron transport measurements. The optical lithography was done by colleagues at the University of Nottingham and the Hall bar structures were deposited into at Leeds in the same manner used for growth of sheet films. The Hall bars consist of a strip of material 50 $\mu$m wide with three cross structures. Gold pads were deposited on top of the ends of each of the arms of magnetic material to make it easier to attach electrical contacts, which were made with aluminium wires by a wedge bonder. An example of a patterned sample is shown in Figure 3.3.

### 3.2.4 SQUID VSM

The magnetisation of a Ta/Pt/Co(1.0nm)/Pt film was measured in an MPMS SQUID VSM [61] at 300 $K$. In the SQUID VSM magnetic fields are applied to magnetise the sample using a superconducting magnet. The sample sits within a set of detection coils, which are inductively coupled to a SQUID. The sample is vibrated up and down within the detection coils, where a current is produced due to the varying magnetic signal from the

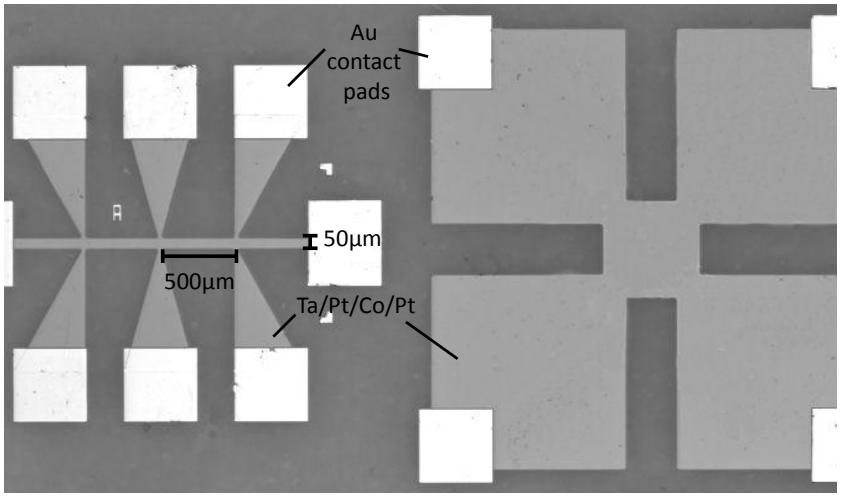


**Figure 3.3:** Light microscope image of a patterned Pt/Co/Pt film. The Hall bar is on the left and the structure on the right is a larger area of material suitable for electrical measurements, but also useful for domain wall motion studies.

sample. The SQUID converts the current in the detection coils into a voltage, which is then amplified. The time-varying voltage has a component that is proportional to the vibrating frequency, which is separated from the signal due to the sample magnetic moment by lock-in amplifier techniques. The SQUID VSM measures the moment of the whole sample. The Si/SiOx substrate gives a diamagnetic signal, which can be removed by subtracting a negative linear component equal to the gradient of the data above the ferromagnetic saturation field. An example of a hysteresis loop before and after the diamagnetic background subtraction is shown in Figure 3.4a. The volume magnetisation is found by dividing the moment of the saturated film by the volume of ferromagnetic material. To minimise the uncertainties, particularly those associated with knowing the area of the film, five pieces of a Ta/Pt/Co(1.0nm)/Pt film were measured individually. All the films were approximately 3 $mm$ x 3 $mm$ and the size was estimated from photographs of the samples against a standard scale. The moment was plotted against the estimated Co volume. The gradient of the least squares fit to the data, shown in Figure 3.4b, gives the magnetisation as (1.29 $\pm$ 0.08) $MA/m$.

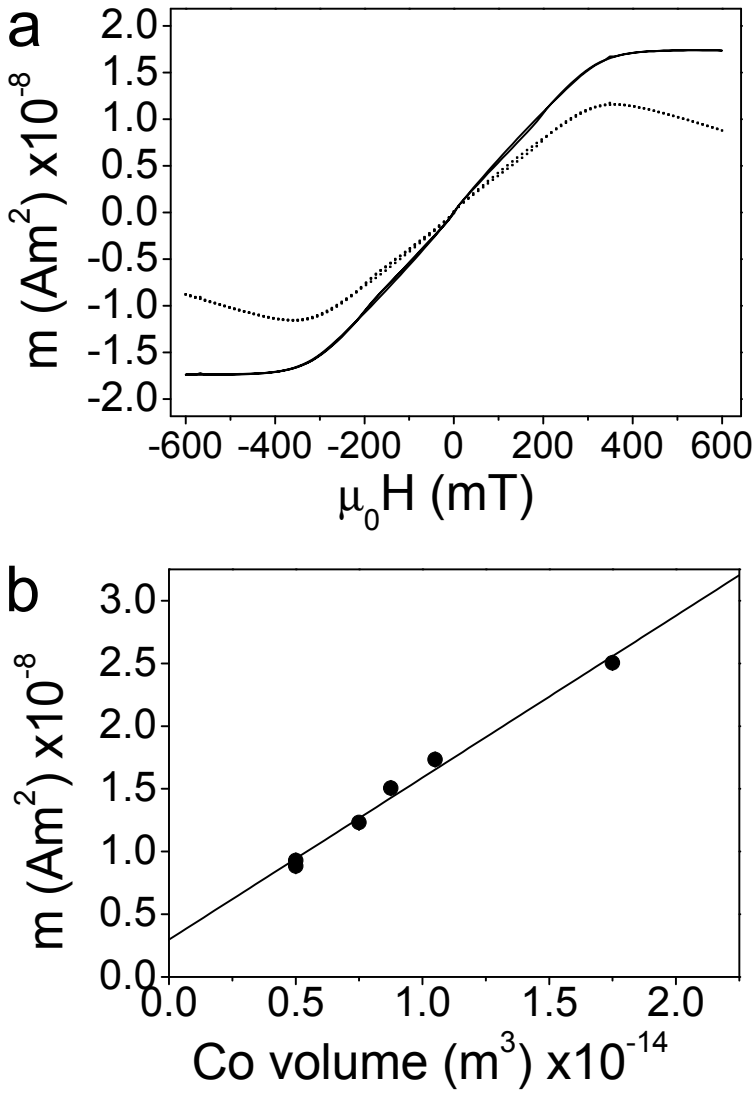


**Figure 3.4:** a) Moment versus applied magnetic field hysteresis loops are shown for a Ta/Pt/Co(1.0nm)/Pt film on a thermally oxidised silicon substrate. The points are the data and the solid line is the data with a linear background due to the diamagnetic substrate subtracted. b) The saturation magnetic moment for films of the Ta/Pt/Co(1.0nm)/Pt film of different areas is plotted against the volume of the Co layer. The magnetisation errors bars are from the standard error in the measurement and are smaller than the data points. The solid line is a least squares fit to the data, where the positive intercept with the moment axis demonstrates that there is an additional magnetic moment due to Pt atoms in proximity to Co, and the gradient gives the Co volume magnetisation as (1.29 $\pm$ 0.08) $MA/m$.

### 3.2.5 Piezoelectric transducers

Once suitable Pt/Co/Pt films deposited on thin glass substrates had been characterised, they were attached to piezoelectric transducers for measurements of magnetic properties under strain. The glass substrates of the thin films or Hall bars were bonded to transducers using a two-part epoxy resin. To cure the resin the samples were heated in an oven to 80 $^oC$ for 90 minutes. Two types of transducers (both available commercially from Piezomechanik GmbH [62]) were used in this work: uniaxial and biaxial. Figure 3.5 is a schematic of the two transducer types with Pt/Co/Pt Hall bars attached.

The transducers are made from PZT, a piezoelectric ceramic which generates a voltage when the structure of the material is distorted [63]. The converse piezoelectric effect is employed to strain the samples studied here; voltage can be applied to the transducers, causing them to expand or contract. The expansion and contraction of the two types of transducer are shown in Figure 3.6. The expansion is approximately linear with applied voltage, so that a voltage can be applied to strain the material, then removed to return the material to its original length. There is, however, a small hysteresis in the voltage strain characteristics which can be seen in Figures 3.7 and 3.8.

The two types of transducer have different structures [64]. Uniaxial transducers are made of thin layers of PZT with individual electrodes glued into a stack. The expansion on application of positive voltage is perpendicular to the stack, along the long axis of the uniaxial transducer. Biaxial transducers are made of a single piece of PZT, with electrodes on two of the shorter sides. The expansion on application of positive voltage is along the short axis of the biaxial transducers (see Figure 3.6).

The specified voltage range of the transducers is -30 $V$ to 150 $V$. The uniaxial transducers are 9 $mm$ long with a maximum expansion $\delta l$ of 9 $\mu m$ at 150 $V$, giving a maximum uniaxial strain $\delta l/l$ of 0.1 %. The biaxial transducers are 2 $mm$ thick and expand by up to 2 $\mu m$ at 150 $V$, giving a maximum uniaxial strain $\delta t/t$ of less than 0.1 %. These values are the strain generated in a free transducer, but bonding the glass substrates to one side of the transducers could have a clamping effect, limiting the maximum expansion. The strain from the transducer might not be effectively transmitted through the layers of epoxy resin, glass substrate and the Ta/Pt of the multilayer film to reach the Co. The next section describes how the piezo-voltage to Pt/Co/Pt strain characteristics of the Hall bar samples were measured.

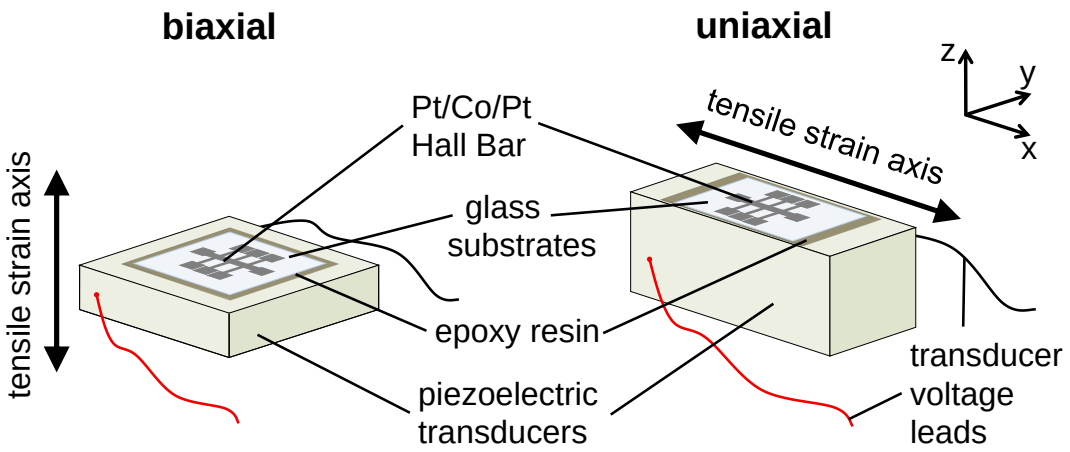


**Figure 3.5:** Schematic of biaxial and uniaxial piezoelectric transducers with Pt/Co/Pt hall bars attached with epoxy resin. The principle strain axes are labelled, showing which directions the transducers extend in under application of positive voltage to the leads.

## 3.3 Strain characterisation

The strain in a metal can be related to its change in resistance. The resistance $R = V/I$ of a Pt/Co/Pt Hall bar sample (shown in Figures 3.3 and 3.5) can be measured by passing a current along the central bar and measuring the voltage between two parallel cross structures. A current of 1 $mA$ was applied from a Keithley 2601 and the voltage was measured using a Keithley 182 nanovoltmeter. If the Hall bar is mounted on a uniaxial transducer, applying a voltage to the piezoelectric increases the length of the central bar, as shown in Figure 3.6a. Since the resistance of a wire of resistivity $\rho$, length $l$ and cross-sectional area $A$ is given by

$$R = \frac{\rho l}{A}, \tag{3.1}$$

a change in the length of the central bar will give a proportional change in its resistance, measured using the geometry shown in Figure 3.6b. However, there are other geometrical and physical effects when the bar is strained: the cross-sectional area may change by an amount determined by Poisson's ratio, $\nu$, and the resistivity may change as the structure of the material is distorted. Starting by differentiating Equation 3.1, an expression relating the dimension change and resistance change can be obtained, which takes account of changes in $\rho$ and $A$. Dividing through by $R$ gives the following expression for the proportional

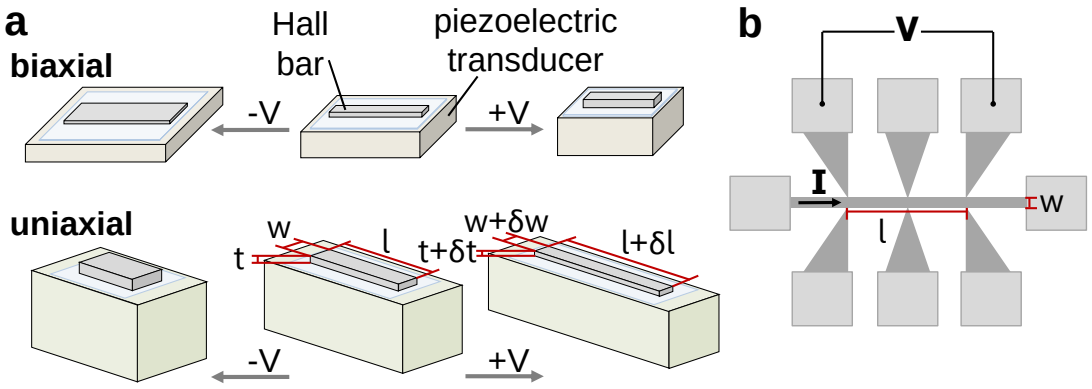


**Figure 3.6:** a) Diagram showing the expansion and contraction of biaxial and uniaxial piezoelectric transducers when voltage is applied. b) Hall bar geometry used for measuring strain from resistance change.

change in resistance:

$$\frac{\delta R}{R} = \frac{\delta l}{l} - \frac{\delta A}{A} + \frac{\delta \rho}{\rho}. \tag{3.2}$$

This can be written in terms of the proportional length change or strain $\varepsilon = \delta l/l$ as

$$\frac{\delta R}{R\varepsilon} = (1 - \frac{\delta A}{A\varepsilon}) + \frac{\delta \rho}{\rho\varepsilon}, \tag{3.3}$$

where the first term on the right is a factor describing the geometrical deformation $C_{geo} = (1 - \delta A/(A\varepsilon))$ and the second term on the the right is the strain coefficient of specific resistivity $C_\rho = (\delta\rho/(\rho\varepsilon))$, which has been measured by Kuczynski [65] as 2.60 for Pt and 0.84 for Co. The strain in a strip of Pt/Co coupled to a transducer can then be found from changes to the resistance

$$\varepsilon = \frac{\delta R}{R} \frac{1}{C_{geo} + C_{\rho Pt/Co}}, \tag{3.4}$$

with $C_{\rho Pt/Co} = 1.72$, taking the average of the Pt and Co values. All that remains is to calculate the geometrical factors for uniaxial and biaxial transducers. The effects of applying voltages to the biaxial and uniaxial transducers are shown in Figure 3.6.

### 3.3.1 Uniaxial transducers

For the uniaxial transducers the geometrical factor is found from

$$\frac{\delta A}{A} = \frac{\delta t}{t} + \frac{\delta w}{w} = \varepsilon_z + \varepsilon_y = -\varepsilon_x(\nu_z + \nu_y), \tag{3.5}$$

$$C_{geo-uni} = (1 - \delta A/(A\varepsilon)) = 1 + \nu_z + \nu_y. \tag{3.6}$$

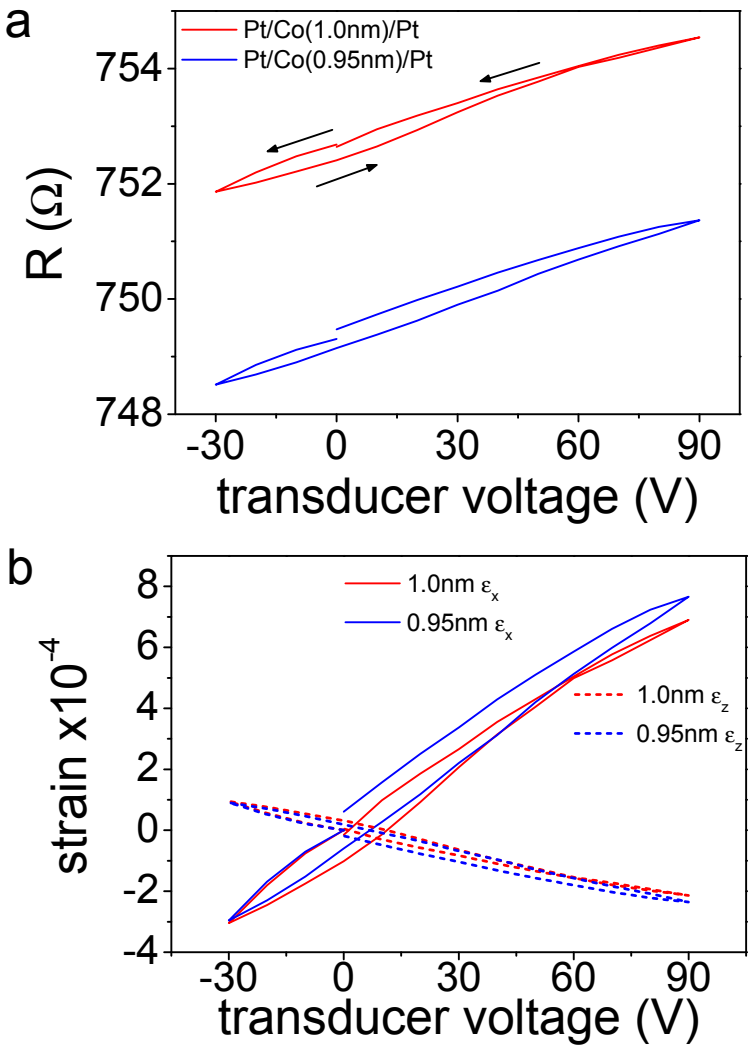


**Figure 3.7:** a) The resistance and b) the strain calculated from the resistance change of Pt/Co/Pt Hall bars on uniaxial transducers is plotted against transducer voltage. The voltage was swept from 0 $V$ to -30 $V$ then to 90 $V$ and back to 0 $V$.

The Poisson ratio of the film is assumed to be $\nu_z = 0.36$, an average between that of bulk Co (0.33) and bulk Pt (0.39). The Poisson ratio of the transducers is assumed to be $\nu_x = \nu_y = 0.5$. This gives an expression for the strain of

$$\varepsilon_x = \frac{\delta R}{R}\left(\frac{1}{(1+0.36+0.5)+1.72}\right) = 0.28\frac{\delta R}{R}. \tag{3.7}$$

The strain in the y and z directions can be obtained from

$$\varepsilon_x = -\frac{1}{\nu_y}\varepsilon_y = -\frac{1}{\nu_z}\varepsilon_z. \tag{3.8}$$

Figure 3.7 shows the resistance and the calculated strain against applied transducer voltage for uniaxial transducers with Ta/Pt/Co(t)/Pt Hall bars (t = 0.95, 1.0 $nm$). The measurements show an elongation along x (the long axis of the transducer) and corresponding compression out-of-plane. There is some small hysteresis in the strain, so that the strain for a given transducer voltage is slightly different depending whether the voltage is being swept up or down. Since the resistance was measured at room temperature with no control over the ambient conditions, the difference in the initial and final resistance at 0 $V$ is due to a small temperature drift, where the size of the drift is consistent with a temperature change of $\sim$0.1 $K$ in Pt at room temperature [66; 67]. The measurements were taken up to 90 $V$, giving a maximum strain of $\varepsilon_x \sim 7 \times 10^{-4}$ (or 0.07%), consistent with an estimated strain in the transducer at this voltage of $\sim 6 \times 10^{-4}$.

### 3.3.2 Biaxial transducers

For the biaxial transducers the geometrical factor is found from

$$\frac{\delta A}{A} = \frac{\delta t}{t} + \frac{\delta w}{w} = \varepsilon_x(1 - \frac{1}{\nu_z}), \tag{3.9}$$

$$C_{geo-bi} = (1 - \delta A/A\varepsilon) = \frac{1}{\nu_z}. \tag{3.10}$$

The strain in the y and z directions can be obtained from

$$-\frac{1}{\nu_z}\varepsilon_x = -\frac{1}{\nu_z}\varepsilon_y = \varepsilon_z. \tag{3.11}$$

Figure 3.8 shows the resistance and the calculated strain against applied transducer voltage for biaxial transducers with Ta/Pt/Co(t)/Pt Hall bars (t = 0.85, 0.95, 1.0 $nm$). The measurements show an elongation along z (out-of-plane) and corresponding compression in-plane, and as with the uniaxial transducers, there is some small hysteresis. All three Co thicknesses have a measured maximum strain of $\varepsilon_z \sim 9 \times 10^{-4}$ (or 0.09 %), consistent with an estimated strain in the transducer at this voltage of $1 \times 10^{-3}$. The closeness of the estimated transducer strain to the measured Hall bar values shows that the strain is transmitted very effectively with hardly any losses in all but one sample (uniaxial t = 0.9 $nm$).

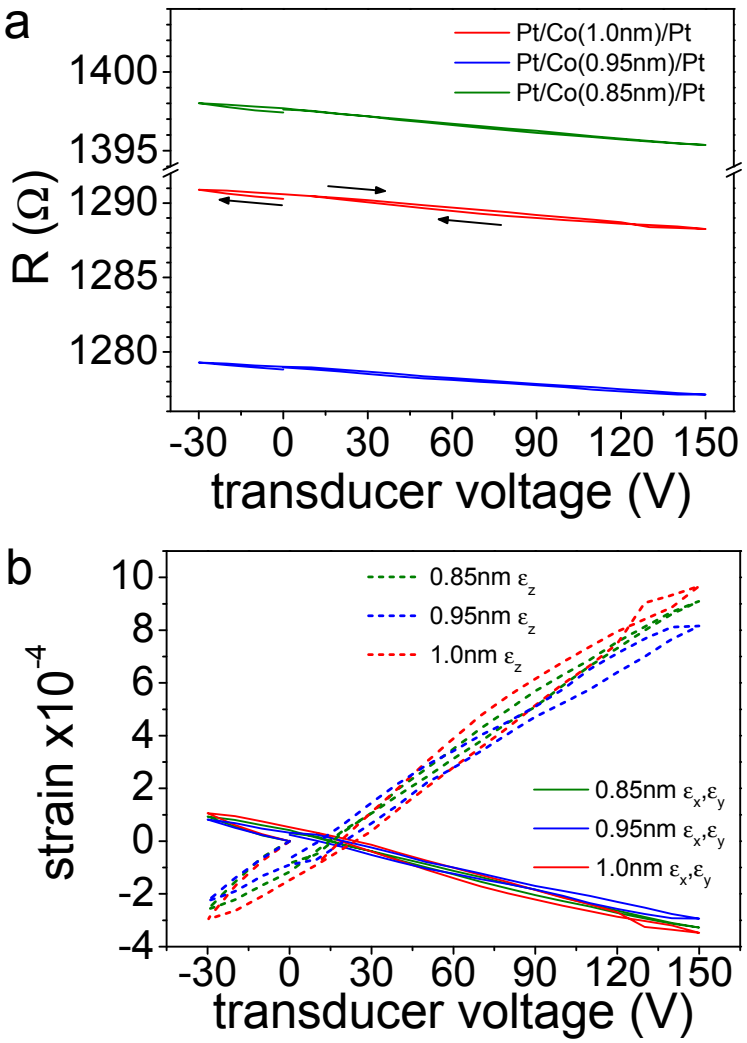


**Figure 3.8:** a) The resistance and b) the strain calculated from the resistance change of Pt/Co/Pt Hall bars on biaxial transducers is plotted against transducer voltage. The voltage was swept from 0 $V$ to -30 $V$ then to 150 $V$ and back to 0 $V$.

## 3.4 Techniques for indirect measurement of perpendicular magnetisation

To measure the change in room temperature magnetic properties of PMA thin films, two techniques with sensitivity to perpendicular magnetisation were employed. The EHE and polar MOKE are both indirect measures of the perpendicular component of magnetisation. Both can be used to measure out-of-plane hysteresis loops and, if an in-plane field is applied

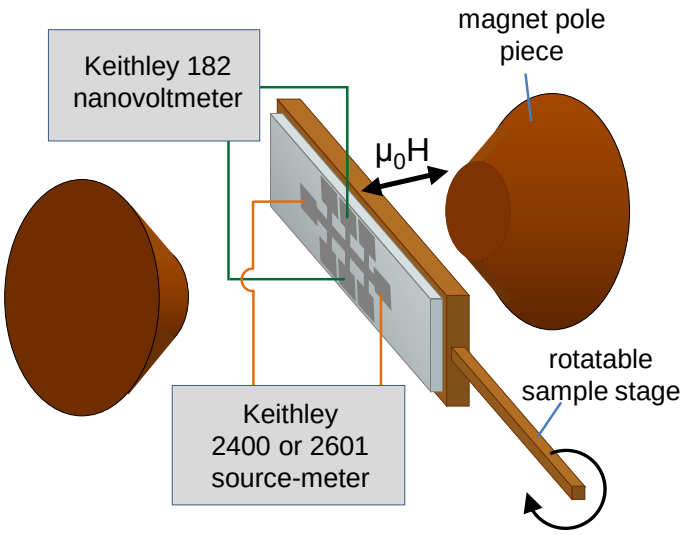


**Figure 3.9:** A schematic of the set-up for EHE measurements. An electromagnet applies a field of up to 0.9 $T$ and the sourcemeter passes a current through the sample while a nanovoltmeter reads the voltage. The sample is mounted on a rotatable stage so that a field can be applied in-plane or out-of-plane.

to rotate the magnetisation from the easy to hard axis, to measure the perpendicular magnetic anisotropy field. MOKE can also be used to image magnetic domains using wide-field Kerr microscopy.

### 3.4.1 Extraordinary Hall effect

The EHE, also called the anomalous Hall effect (AHE) is an electron transport technique. The geometry of Hall measurements requires a current to be passed through a conducting material and the voltage to be measured across the material, perpendicular to the current flow. An out-of-plane magnetic field is applied, perpendicular to both the current flow and voltage measurement. Up and down spins are scattered differently so that charge builds up along the sides of a wire. A diagram of the equipment used to measure the EHE is shown in Figure 3.9. The magnetic field is applied by a water-cooled electromagnet with iron pole pieces, which can reach applied fields of 0.9 $T$. The sample is mounted on a rotatable stage so that the field can be applied out-of-plane or in-plane. The current is sourced by a Keithley 6201 or 2400 sourcemeter and a 182 nanovoltmeter reads the voltage. For each measured point currents of $\pm 1$ $mA$ are passed through the sample and measured voltage,

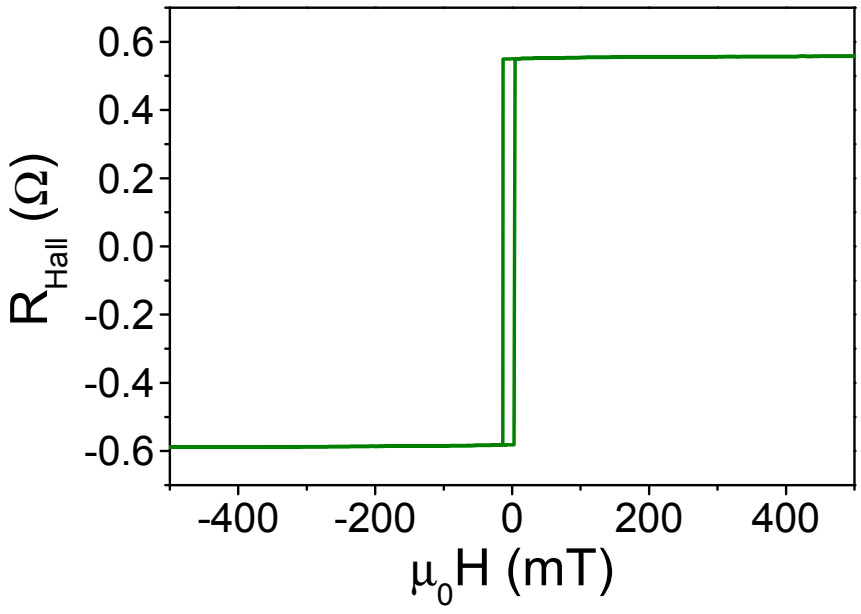


**Figure 3.10:** An extraordinary Hall resistance hysteresis loop of Pt/Co/Pt is plotted against applied magnetic field. Applying fields well above the saturation field shows that the linear ordinary Hall term in Pt/Co/Pt is very small – a least squares linear fit gives a gradient of $(4.7\pm0.2)\times10^{-6}\Omega/mT$.

which is $\sim$0.1-1$mV$ in size, is converted to a resistance.

The Hall resistance can be expressed phenomenologically as

$$R_H = (R_o H_Z + R_E M_z)/t. \tag{3.12}$$

The first term represents the ordinary Hall effect, discovered by Edwin Hall in 1879 [68], where $R_o$ is the ordinary Hall coefficient, which is linear in applied out-of-plane field $H_z$. The second term arises from the EHE, first measured by Hall just a few years later [69], which is proportional to the out-of-plane magnetization $M_z$, where $R_E$ is the EHE coefficient. Figure 3.10 shows an EHE hysteresis loop of a Pt/Co/Pt Hall bar up to large applied fields. The slope due to the ordinary Hall effect is very small compared to the size of the EHE signal, so has been neglected in any analysis [70].

In the ordinary Hall effect, charge carriers are deflected by a Lorentz force as they move through the material in the perpendicular magnetic field. While the ordinary Hall effect depends mainly on carrier density and is not limited to magnetic materials, the EHE only occurs in ferromagnets and is still an area of active research [71]. Charge carriers with opposite spin are scattered in opposite directions. They can be scattered by interactions

related to their Berry's phase curvature, giving an 'intrinsic' contribution, or by interactions related to the disorder in the material, giving rise to the 'extrinsic' contributions of skew-scattering and side-jump. Skew scattering deflects an electron based on its spin-orbit coupling with an impurity, while side-jump deflection is related to the electric fields seen by electrons as they move towards and away from impurities [71]. Although the EHE is a topic of research in its own right, here it has been used simply to give a measure of the component of the magnetisation pointing out-of-plane. The perpendicular anisotropy has been measured by monitoring the EHE signal as the magnetisation is pulled from out-of-plane to in-plane. More details of this technique are given along with results in Chapter 4.

### 3.4.2 Magneto-optical Kerr effect

The Kerr effect, first observed in 1877 [72], is relevant for opaque materials such as metallic thin films from which light can be reflected, but its discovery was preceded by Faraday's measurement of the same effect in transmission in 1845 [73]. These effects are due to weak coupling of the optical properties and magnetism of materials.

There are three possible geometries for measuring the Kerr effect: polar, longitudinal and transverse [74]. The polar Kerr effect is sensitive to the out-of-plane component of magnetisation and is present when light is incident at $0^o$ to the surface normal. The longitudinal and transverse geometries require an angle of incidence $\theta_i > 0^o$ and are sensitive to in-plane magnetisation aligned with the plane of incidence, or perpendicular to it, respectively. In the transverse geometry there is only a change in the reflectivity of the light with magnetisation direction. In the polar and longitudinal geometries the light reflected from a magnet has its polarisation rotated and gains an ellipticity.

Light penetrates a magnetic material to a depth equal to the skin depth - approximately 20 $nm$ for metals. The velocity of light in a material can be expressed as $v = (\mu_0 \epsilon)^{-\frac{1}{2}}$, so depends on the electrical permittivity of a material $\epsilon$. This is a tensor defined from $D_i = \epsilon_{ij} E_j$ (where $E_j$ represents the electric field component). For the case of the polar Kerr effect, where the light is incident along the surface normal and the magnetisation is also out-of-plane, the permittivity tensor is

$$\boldsymbol{\epsilon} = \epsilon \begin{bmatrix} 1 & iQ_V m_z & 0 \\ -iQ_V m_z & 1 & 0 \\ 0 & 0 & 1 \end{bmatrix}, \tag{3.13}$$

where $m_z$ is the out-of-plane component of the magnetisation and $Q_V$ is the Voigt material constant, which is a perturbation on the permittivity related to the refractive index. The small size of $Q_V$ means that Kerr rotation is a small effect.

In a MOKE measurement, linearly polarised light, which can be decomposed into right and left circularly polarised light, reflects from a magnet. The right and left circularly polarised components have different refractive indices so propagate with different velocities and are absorbed differently in the material. As the light propagates in the material, there will be a rotation in the real part and a phase shift (ellipticity) in the imaginary part.

The Kerr effect is a result of spin-orbit coupling, but can be illustrated classically by

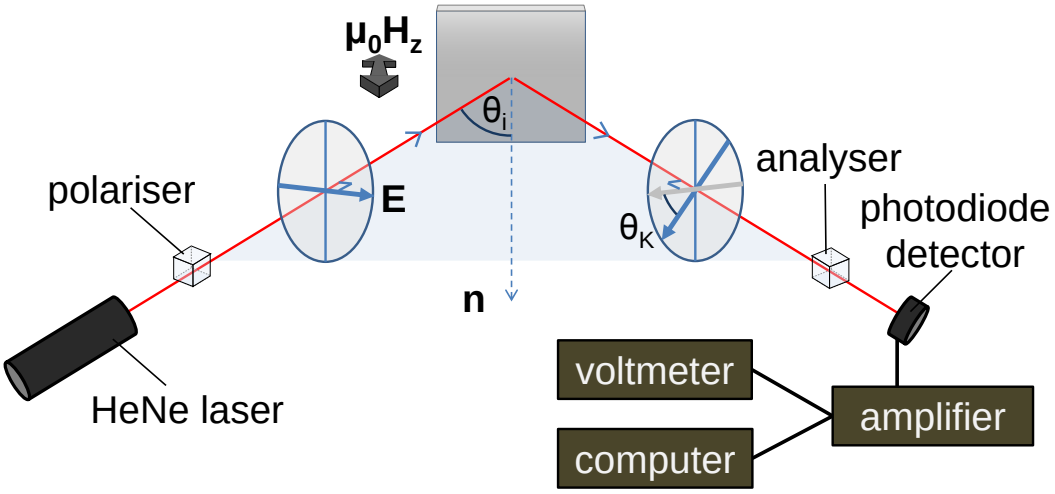


**Figure 3.11:** The diagram shows the main optical and electronic components used for polar MOKE measurements. The polarisation of light is rotated on reflection from a perpendicularly magnetised thin film. The analyser is a polariser set at close to $90^o$ to the first polariser.

expressing the dielectric displacement as

$$\boldsymbol{D} = \epsilon(\boldsymbol{E} + iQ_V \boldsymbol{m} \times \boldsymbol{E}), \tag{3.14}$$

where $\boldsymbol{E}$ is the electric field vector of the incident radiation and $\boldsymbol{m}$ is the unit vector of the sample magnetisation [74]. The electric field of the incident light interacts with electrons in the sample causing oscillating currents parallel to the polarisation. The Lorentz force $\boldsymbol{m} \times \boldsymbol{E}$ in Equation 3.14 deflects the electrons, giving the currents a component perpendicular to the magnetisation and polarisation directions, so that the electric field of the reflected light is rotated and gains an ellipticity.

The magneto-optical Kerr effect has been used in this work to measure magnetic hysteresis loops and to image magnetic domains. Two separate sets of equipment were used: a laser MOKE was used to take magnetic hysteresis loops for sample characterisation and a Kerr microscope was used to image magnetic domains and take hysteresis loops. Both were used in the polar MOKE geometry.

The basic anatomy of both the laser MOKE and the Kerr microscope is broadly the same. A schematic of the laser MOKE, demonstrating the principle of the technique is shown in Figure 3.11, while a schematic of the Kerr microscope and its optics is shown in Figure 3.12. Light, from a HeNe Laser or white LED, passes through a polariser. The linearly polarised light interacts with the electrons in a magnetised sample so that the

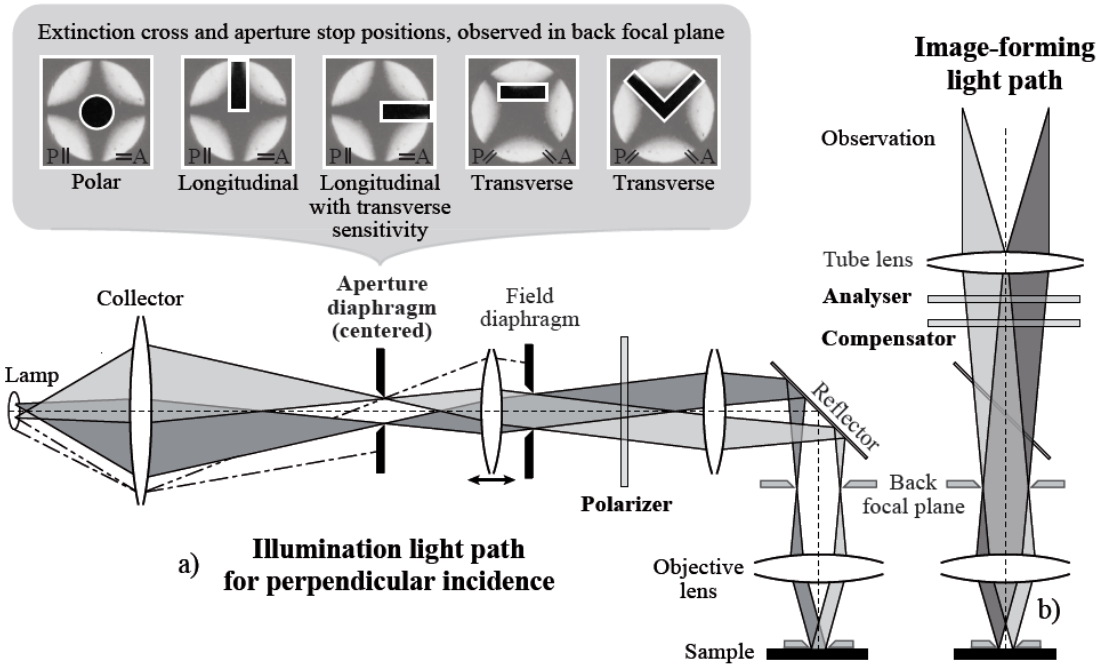


**Figure 3.12:** The diagram shows the light paths and image formation in a Kerr microscope. a) The light from the LED lamp passes through a polariser before being reflected through the objective lens and onto the sample. At the aperture diaphragm the aperture is adjusted to select the region of the polarisation cross needed for polar, longitudinal or transverse Kerr measurements. b) The light reflected from the sample passes back through the objective and straight up to the analyser and compensator before being detected by the CCD camera. The diagram is reproduced from Ref [75].

reflected light has its polarisation rotated. The analyser (or analyser and compensator in the case of the Kerr microscope) polarises the light at close to $90^o$ to the initial polarisation, thus isolating the signal due to the change in polarisation. The intensity of this signal is measured by a photodiode detector or CCD camera. A MOKE measurement is sensitive to changes in the magnetisation, rather than the absolute value of the magnetisation.

### 3.4.3 Laser MOKE

The laser MOKE (Figure 3.11) uses a HeNe laser with wavelength of 633 $nm$ and a power below 15 $mW$. The polariser is set to produce P-polarised light, with the electric field vector in the plane of incidence. The components can be arranged to measure longitudinal MOKE with the applied magnetic field in-plane and the angle of incidence at $\theta_i \sim 30^o$. For

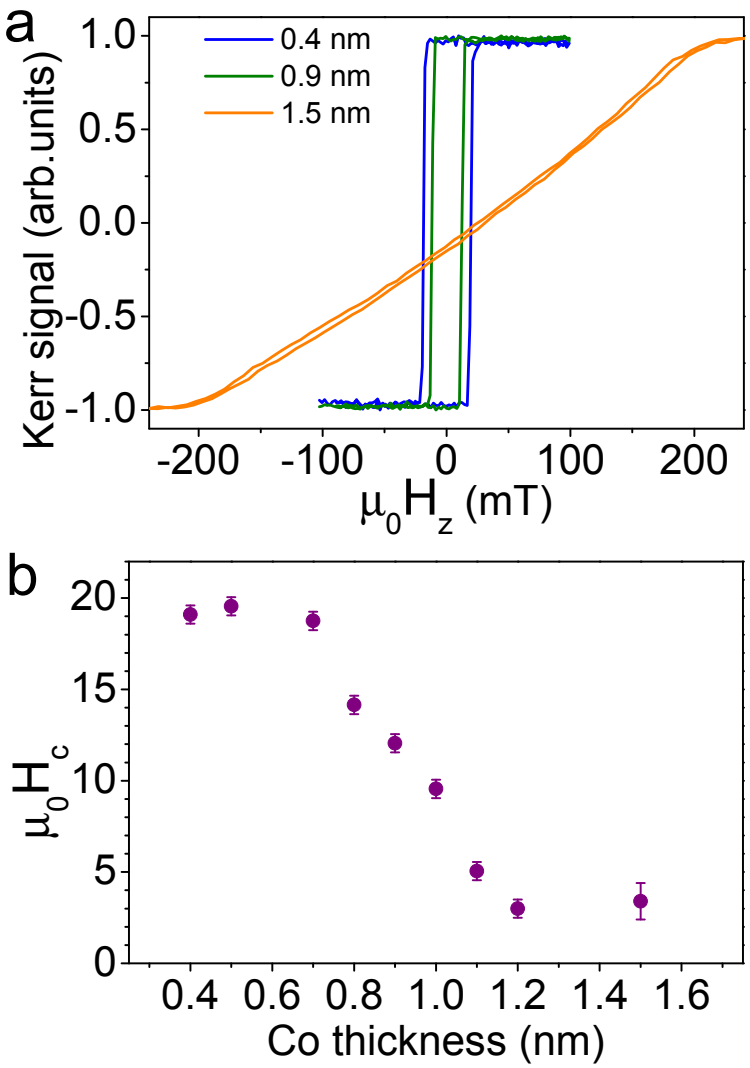


**Figure 3.13:** a) Polar MOKE hysteresis loops of Pt/Co/Pt with varying thicknesses of Co. b) The coercive fields of polar MOKE hysteresis loops of Pt/Co/Pt thin films are plotted to show the dependence on Co thickness. The applied field is out-of-plane in each measurement.

this work polar MOKE was used with the field applied out-of-plane. A mirror directed the polarised light through a hole in one pole piece of the electromagnet so that the light was incident at $\theta_i = 0^o$. Magnetic fields of up to 600 $mT$ can be applied by a water cooled electromagnet with iron pole pieces. Reflected light passes through the analyser and is detected by a photodiode. This produces a current, which is converted into an amplified voltage signal by the amplifier. The signal can be read off from a voltmeter or recorded by

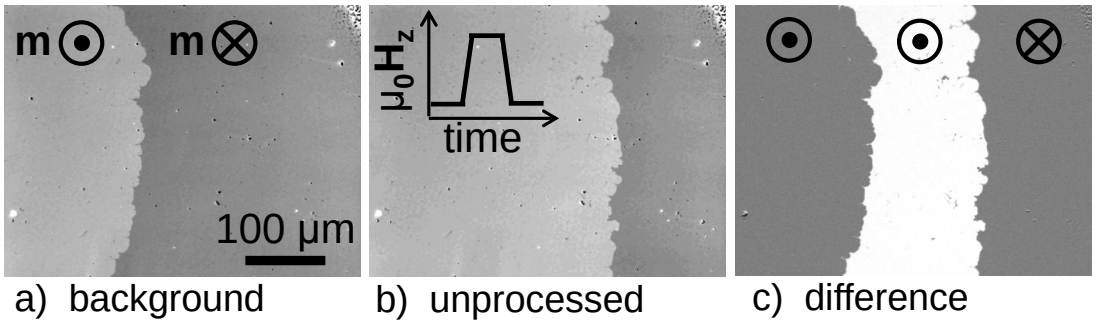


**Figure 3.14:** A sequence of polar Kerr microscope images used to measure domain wall motion are shown. a) An image of the initial domain wall position is recorded. b) A magnetic field pulse (see inset) moves the domain wall and another image is recorded. c) The background image is subtracted from the unprocessed image to give the difference image, in which the bright contrast is the region swept out by the domain wall as it is displaced from left to right. In the first two images the dark contrast signifies magnetisation pointing into the page and the bright contrast is the reversed part of the film where the magnetisation is pointing out of the page.

the DAQ card of a computer to produce hysteresis loops.

The laser MOKE was used to characterise magnetic thin films. MOKE hysteresis loops of Pt/Co/Pt thin films are shown in Figure 3.13a. These loops were used to assess the thicknesses of Co required for PMA. The loops with Co thicknesses of t = 0.4 and 0.9 $nm$ are square and fully remanent at applied fields of 0 $mT$, demonstrating that these films have PMA. The thicker film with t = 1.5 $nm$ has very little remanence at 0 $mT$ so has in-plane anisotropy. PMA tends to decrease with increasing film thickness (see Chapter 4), and this is reflected to some degree in the trend of decreasing coercive field with film thickness in Figure 3.13b. The thickness of Co in Pt/Co(t)/Pt films above which PMA no longer dominates is around t = 1.1 $nm$.

### 3.4.4 Wide-field Kerr microscopy

The Kerr microscope was used to image domains, measure domain wall velocity and take magnetic hysteresis loops. Hysteresis loops of the change in greyscale can be measured of either the whole image or a selected region. The microscope has a moveable and rotatable sample stage and interchangeable electromagnets powered by a Kepco power supply. The perpendicular magnet coil is water-cooled with no magnetic core or pole pieces.

Figure 3.12 shows the path of the light from the white LED through the optics to the

sample and then to the camera. For polar MOKE, the centre of the polarisation cross (i.e. light incident and reflected at $0^o$) is selected using the aperture. The greyscale images recorded by the CCD camera contain information seen in standard light microscope images, as well as a contribution to the intensity of light reflected from ferromagnetic material due to the Kerr effect. Parts a and b of Figure 3.14 show Kerr images with contrast between oppositely magnetised regions of a Pt/Co/Pt film with PMA.

To measure domain wall velocity, a domain is first nucleated and expanded with a pulse of out-of-plane field. An image is recorded of the static position of the domain wall (Figure 3.14a), then a magnetic field pulse is applied to move the domain wall and a second image is recorded (Figure 3.14b). The difference between these two images (Figure 3.14c) shows the region swept out by the domain wall. The average displacement (and associated standard error) of the domain wall is measured in pixels and converted to a velocity using a conversion from pixels to micrometers and the length of the field pulse. By taking the difference between two images, any features not due to a change in the magnetisation are removed and the contrast between domains is improved.

## 3.5 Summary

Methods of preparation, characterisation and measurement of Pt/Co thin films have been discussed. Thin films were deposited by dc magnetron sputtering, with some films patterned into Hall bars. Thin films of Pt/Co were found to have PMA for Co thicknesses of around 1.1 $nm$ and below, and to have a magnetisation of 1.29 $MA/m$. Suitable thin films were coupled to piezoelectric transducers and the strain in the Pt/Co versus the piezoelectric voltage was characterised. The strain was transmitted effectively through the epoxy resin and glass between the transducers and the thin films. PMA, perpendicular magnetic hysteresis loops and domain wall velocity were measured for Pt/Co films with a range of Co thicknesses on biaxial and uniaxial transducers. The following Chapters describe some of these measurements in more detail and present results of the effects on the measured properties of strain from the piezoelectric transducers.

# Chapter 4

Anisotropy change with strain in Pt/Co/Pt thin films

## 4.1 Introduction

This chapter presents results of magnetic anisotropy change in ultra-thin Pt/Co/Pt under strain from uniaxial and biaxial piezoelectric transducers. The magnetic anisotropy is measured using a method based on the extraordinary Hall effect (EHE). The details of the anisotropy measurements are described and the magnetisation dynamics during the measurements are examined using Kerr microscopy. The effect of strain on the anisotropy of Pt/Co/Pt is characterised and the magnetostriction constant is measured.

## 4.2 Samples

Ta(4.5nm)/Pt(2.5nm)/Co(t)/Pt(1.5nm) multilayers were deposited by dc magnetron sputtering onto 150 $\mu m$ thick glass substrates at room temperature. The multilayers were patterned into 50 $\mu m$ wide Hall bars and the glass substrates with Hall bar devices on top were bonded with epoxy resin to piezoelectric transducers. Hall bars with Co thicknesses of t = 0.85, 0.95, 1.0 $nm$ were bonded to biaxial transducers and Hall bars with Co thicknesses of t = 0.95, 1.0 $nm$ were bonded to uniaxial transducers. The samples for the uniaxial and biaxial transducers were grown in different vacuum cycles. Figure 4.1 shows the sample structure.

Voltages of between -30 $V$ and 150 $V$ can be applied to the transducers to induce strain. Applying a positive voltage to a biaxial transducer creates a biaxial compression in the plane of the sample and a corresponding tensile strain out-of-plane. For a uniaxial transducer at a positive voltage, the tensile strain is in the plane of the device along the x axis, as defined in Figure 4.1. There is a corresponding compressive strain in the y and z directions (see Chapter 3 for strain details).

## 4.3 Anisotropy Measurements

To assess the effect of piezo-induced strain on the magnetic anisotropy energy of the Pt/Co/Pt films, measurements of anisotropy field were carried out by monitoring the EHE signal during in-plane magnetic field sweeps. The size of the EHE resistance gives a measure of the component of the magnetisation pointing out of the plane and can be used to determine PMA [70]. The magnetic anisotropy field is the field required to coherently rotate the magnetisation from the easy axis (out-of-plane) to the hard axis (in-plane). A

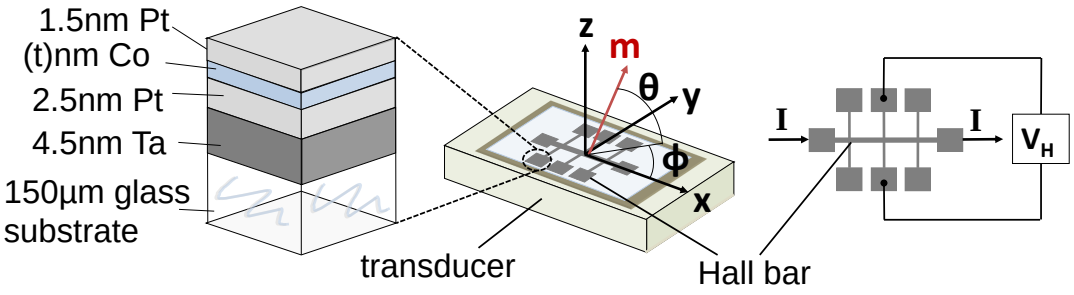


**Figure 4.1:** Schematic of a Hall bar on a transducer showing the sample structure and measurement geometry.

low field range over which the magnetisation rotates coherently is demonstrated using Kerr microscopy.

A schematic of the measurement geometry is shown in Figure 4.1. A current of 1 $mA$ was passed along the Hall bar (x) and the Hall voltage monitored in an orthogonal in-plane direction (y) via one of the cross structures. To make a measurement, the plane of the device was first precisely aligned to an in-plane magnetic field by rotating the sample around the x axis until the Hall signal was as close to zero as possible during a field sweep along the y axis, as shown in Figure 4.2. An out-of-plane field was then applied using a permanent magnet to saturate the magnetisation of the Pt/Co/Pt. Following this, an in-plane field was swept along the y axis from 0 $mT$ to 700 $mT$ and the Hall resistance measured as the magnetisation rotated from out-of-plane (maximum Hall signal) to in-plane (zero Hall signal). Figure 4.3 shows examples of the normalised EHE data obtained. Initially (up to 60 $mT$ in the case of Figure 4.3) $m_z$ follows a parabola as expected if the magnetisation were to rotate coherently. As the field increases beyond 60mT, $m_z$ deviates from the parabola, as the magnetisation breaks up into domains. The magnetisation is eventually saturated in the plane, and the path $m_z$ would have followed if the magnetisation had continued to rotate coherently is rejoined. The low field regime (up to 60 $mT$) where the moment rotates coherently is extrapolated, following the dashed lines in Figure 4.3, to obtain the anisotropy field $H_k$, which is defined as the point where the extrapolated coherent rotation crosses $m_z = 0$. Proper alignment of the field to the plane of the device ensured that the films were truly saturated along an in-plane axis, allowing for direct comparison of $H_k$ between samples.

Once the anisotropy field is known, the effective anisotropy constant can be calculated

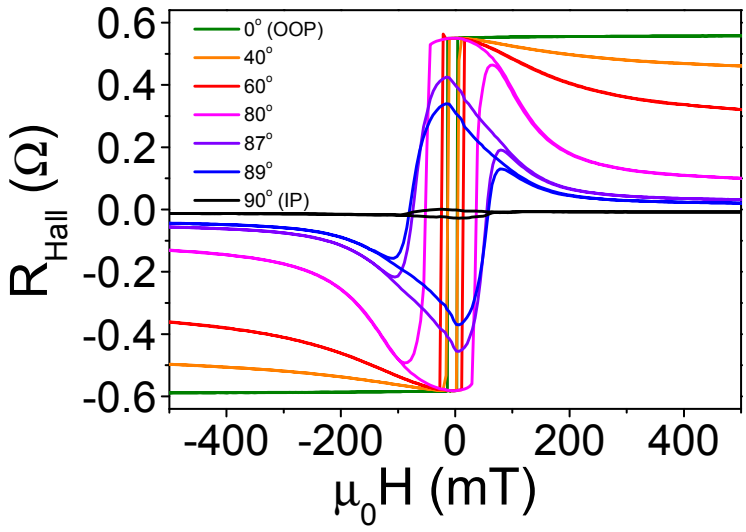


**Figure 4.2:** EHE resistance hysteresis loops of Pt/Co(0.95nm)/Pt on a uniaxial transducer are shown with the magnetic field applied at a range of angles between out-of-plane $\theta = 0^o$ and in-plane $\theta = 90^o$. As the sample is tilted further towards an in-plane applied field, the out-of-plane component of the field decreases giving rise to a smaller out-of plane component of the magnetisation. When the sample is fully aligned to the in-plane field, the change in the Hall signal over the field sweep is minimal. The large difference between $\theta = 90^o$ and $\theta = 89^o$ demonstrates how sensitive the measurement is to misalignment.

from

$$K_{eff} = \frac{1}{2}\mu_o M_s H_k, \tag{4.1}$$

where $M_s$ is the saturation magnetisation of the Pt/Co/Pt thin film, measured by SQUID VSM as (1.29±0.08)×$10^6$ $A/m$ (see Chapter 3).

To understand the magnetisation dynamics during the EHE measurement process, the same field protocol was applied to a Pt/Co(1.0nm)/Pt sample in a Kerr microscope (set to be sensitive to the polar Kerr effect) while images were recorded. Figure 4.3 shows the images taken at fields corresponding to the numbered items on the EHE plot. At 0 $mT$ the Kerr image is bright and uniform, showing that the magnetisation is saturated out-of-plane. As the in-plane field is increased the image becomes darker due to the drop in the polar Kerr signal as the $m_z$ component of the magnetisation gets smaller. The image remains uniform, indicating that the magnetisation is rotating coherently. As the field is increased further, this is no longer the case; the image now has bright and dark patches of $\sim$2 $\mu m$, where small up and down canted domains have formed in order to lower the energy of

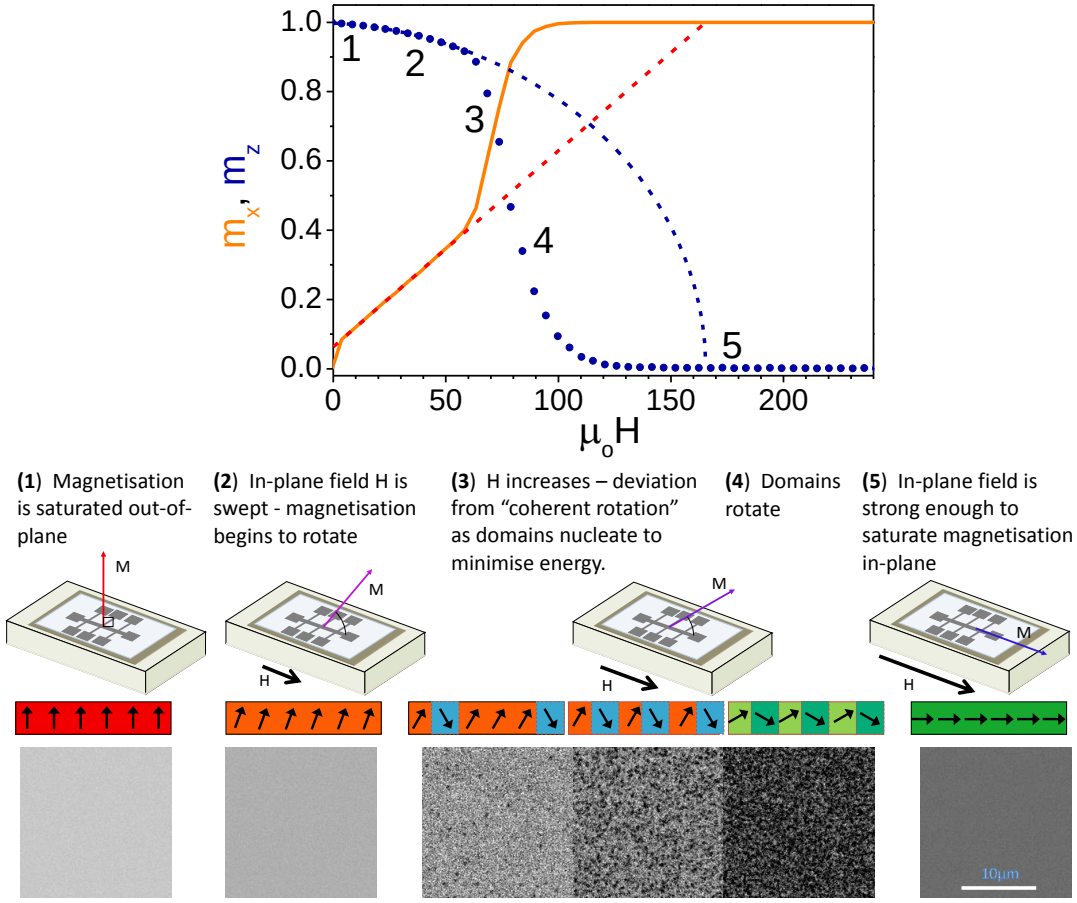


**Figure 4.3:** Rotation of magnetisation in Pt/Co(1.0nm)/Pt on a uniaxial transducer from out-of-plane to in-plane. The plot at the top of the figure shows the normalised EHE data representing the out-of-plane magnetisation component $m_z$ (blue circles) and the in-plane component $m_x$ (solid orange line) derived from this assuming that the total magnetisation $m = \sqrt{m_x^2 + m_z^2} = 1$ throughout the measurement. The dashed lines are a simulation of coherent moment rotation for the $m_z$ (blue dash) and $m_x$ (orange dash) components. The lower part of the figure shows Kerr effect images (the scale bar on the right hand side is 10$\mu$m) and cartoons of the magnetisation rotation process corresponding to the numbered points in the plot. The magnetisation initially rotates coherently before breaking into domains.

the system. The EHE signal drops more rapidly as more canted domains form, until the in-plane field is strong enough to rotate the magnetisation of the whole system in to the plane, shown by the image regaining uniformity. The images demonstrate that the low field EHE does represent a coherent rotation of the magnetisation in the film.

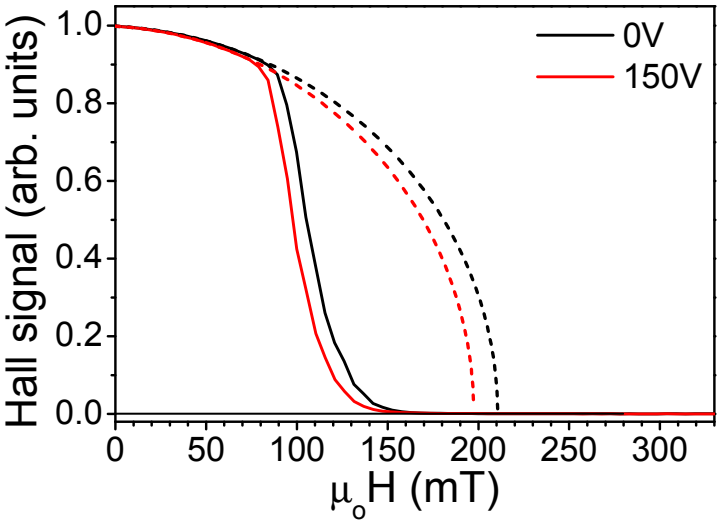


**Figure 4.4:** The normalised EHE signal in a Pt/Co(0.95nm)/Pt Hall bar on a biaxial transducer is plotted against applied in-plane field, as the magnetisation is pulled from out-of-plane to in-plane, with the transducer at a voltage of 0 $V$ (solid black line) and 150 $V$ (solid red line). The dashed lines are extrapolated from the coherent rotation regime at low applied fields. The intercept of a dashed line with a Hall signal of 0 gives the ainsotropy field.

## 4.4 Anisotropy change with strain

Strain adds a magnetoelastic contribution to the magnetic anisotropy. The anisotropy constant change is expected to be

$$\Delta K = \frac{3}{2}\lambda\varepsilon Y, \tag{4.2}$$

where $\lambda$ is the magnetostriction constant, $\varepsilon$ is the strain and Y is the Young's modulus. The effect of strain from biaxial and uniaxial transducers is examined in this section.

### 4.4.1 Biaxial transducers

The biaxial transducers give a biaxial in-plane strain that can be thought of as a uniaxial out-of-plane strain. Applying a voltage to these transducers is expected to produce a change in PMA. Figure 4.4 shows the difference in the EHE during in-plane field sweeps between the transducer at 0 $V$ and 150 $V$ for Pt/Co(0.95nm)/Pt. There is a clear reduction of the anisotropy when 150 $V$ is applied. The measurement of anisotropy field was carried out with the in-plane field applied along the y axis ($90^o$ to the current in the Hall bar)

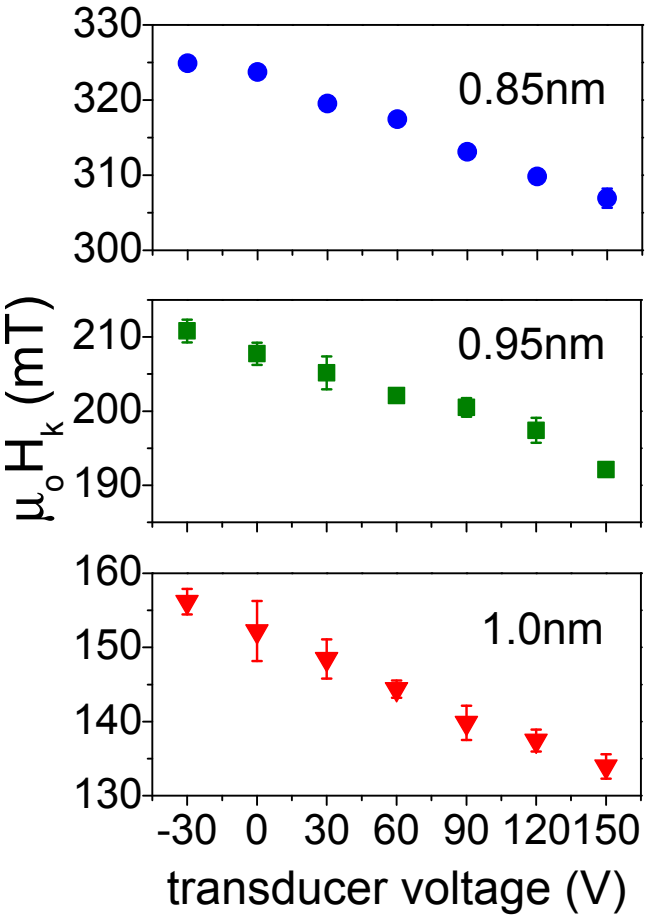


**Figure 4.5:** The magnetic anisotropy field is plotted against biaxial transducer voltage for Pt/Co(t)/Pt thin films (t = 0.85, 0.95, 1.0nm). Each data point is the average of three measurements and the error bars are standard errors on the mean values.

for transducer voltages beginning from 0 $V$, then going from -30 $V$ to 150 $V$ in 30 $V$ steps, and returning to 0 $V$. The anisotropy field is plotted against transducer voltage for Pt/Co(t)/Pt with t = 0.85, 0.95 and 1.0 $nm$ in Figure 4.5. The anisotropy reduces linearly with applied transducer voltage, showing a change of $\sim$20 $mT$ over the available voltage range for all three thicknesses of Co. The higher anisotropy for the compressive out-of-plane strain at -30 $V$ confirms that the change is due to strain.

The magnetic anisotropy constants were calculated using Equation 4.1. The anisotropy constant at 0 $V$, shown in the inset of Figure 4.6, decreases as the Co layer thickness increases, from (210 $\pm$ 10) $kJ/m^3$ for 0.85 $nm$ and (134 $\pm$ 8) $kJ/m^3$ for 0.95 $nm$, to (98 $\pm$

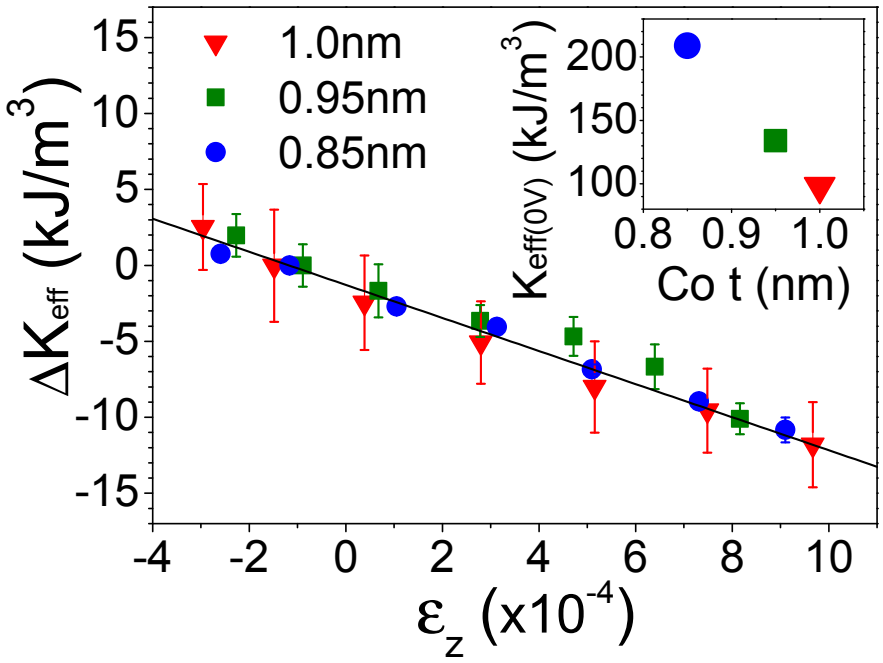


**Figure 4.6:** The change in the PMA constant $K_{eff}$ of Pt/Co(t)/Pt (t = 0.85, 0.95, 1.0 $nm$) due to out-of-plane strain $\varepsilon_z$ induced by biaxial transducers. The solid line is a fit of the data to Equation 4.2. The inset gives the anisotropy constants of the three unstrained films against Co thickness. The error bars in the inset are smaller than the data points.

7) $kJ/m^3$ for 1.0 $nm$. The reduction in $K_{eff}$ indicates that the Co thickness consistently increases, and that the sub-nanometer precision of the thickness scale is valid. The anisotropy constants measured are consistent with 200 $kJ/m^3$ obtained previously for Pt/Co(1.0nm) multilayers [18] and with 400 $kJ/m^3$ obtained for Pt(4nm)/Co(0.5nm)/Pt(2nm) [32].

Figure 4.6 shows the change in the PMA of the Pt/Co/Pt plotted against the tensile out-of-plane strain $\varepsilon_z$ (see Chapter 3 for strain measurement details). The change per unit of strain is the same for the three Co thicknesses. We find a magnetostriction constant of (-3.5 $\pm$ 0.2) $\times 10^{-5}$ from a least squares fit of the change in anisotropy to Equation 4.2 with Y taken to be the average of the Young's moduli of bulk Co and Pt (180 $GPa$) [18].

The measured magnetostriction constant is slightly lower than the bulk Co value of $\lambda =$ -5 $\times 10^{-5}$, and does not change with the Co thickness. The magnetostriction of CoPt alloys falls from positive values at high Pt concentrations to negative values at low Pt concentrations, coming close to -3.5$\times 10^{-5}$ for a $Co_{90}Pt_{10}$ alloy [76]. The negative magnetostriction constant that we measure therefore indicates that there is little intermixing at the Pt/Co

interface. In contrast to a study of Pt/Co multilayers by Hashimoto and co-workers, which found a significant interface contribution to the magnetostriction [18], the independence of the magnetostriction from the Co thickness shows that the Pt/Co/Pt magnetostriction arises mostly from the bulk-like Co volume. The PMA and magnetostriction are both related to the magnetocrystalline anisotropy energy, which arises from spin-orbit coupling and the crystal field [19]. Strain distorts the electron orbitals of the Co atoms. The distortion in the bulk-like Co orbitals has, in the Pt/Co/Pt measured here, a larger effect on the magnetic anisotropy than the distortion of the hybridised Co 3d and Pt 5d orbitals that determine the out-of-plane component of the anisotropy. Under piezoelectric strain, the out-of-plane surface anisotropy remains the same, while the in-plane bulk anisotropy changes.

### 4.4.2 Uniaxial transducers

Uniaxial transducers induce an anisotropic in-plane strain, as well as a small out-of-plane strain, in the Pt/Co/Pt. The anisotropy fields of the Pt/Co(t)/Pt (t = 0.95, 1.0 $nm$) on uniaxial transducers were measured at transducer voltages between -30V and 90V, with the in-plane magnetic field applied at a range of angles $\phi$ = 0$^o$ to 90$^o$ to the current flow. Unlike the biaxial transducers, where the anisotropy field of the Pt/Co/Pt varies with transducer voltage in the same manner regardless of the angle between the current and the applied field, the change in anisotropy field for Pt/Co/Pt on uniaxial transducers is different depending on the angle $\phi$. Figure 4.7 shows the measured anisotropy fields at $\phi$ = 0$^o$ and 90$^o$ for the two Pt/Co(t)/Pt samples on uniaxial transducers (t = 0.95, 1.0 $nm$). The behaviour of the two films is similar – the measured anisotropy field reduces along $\phi$ = 0$^o$ and increases along $\phi$ = 90$^o$ as the transducer voltage increases.

The measured magnetic anisotropy constants $K$ were calculated from the measured anisotropy fields using Equation 4.1. The measured anisotropy constants, with the transducers at -30 $V$, 0 $V$, 30 $V$, 60 $V$ and 90 $V$, are plotted against $\cos(2\phi)$ in Figure 4.8, where $\phi$ is the in-plane angle from the direction of current flow in the Hall bars defined in Figure 4.1. At 0 $V$ the measured $K$ is close to being constant with angle, so magnetic anisotropy in the plane is low. Applying -30 $V$ causes the measured $K$ to become slightly larger along $\phi$ = 0$^o$ and slightly smaller along $\phi$ = 90$^o$. When a positive transducer voltage of 30 $V$ is the applied, the measured $K$ becomes slightly smaller along $\phi$ = 0$^o$ and slightly larger along $\phi$ = 90$^o$. Increasing the positive voltage increases the difference along these two directions, until at 90 $V$ there is a strong variation in the measured $K$ with angle.

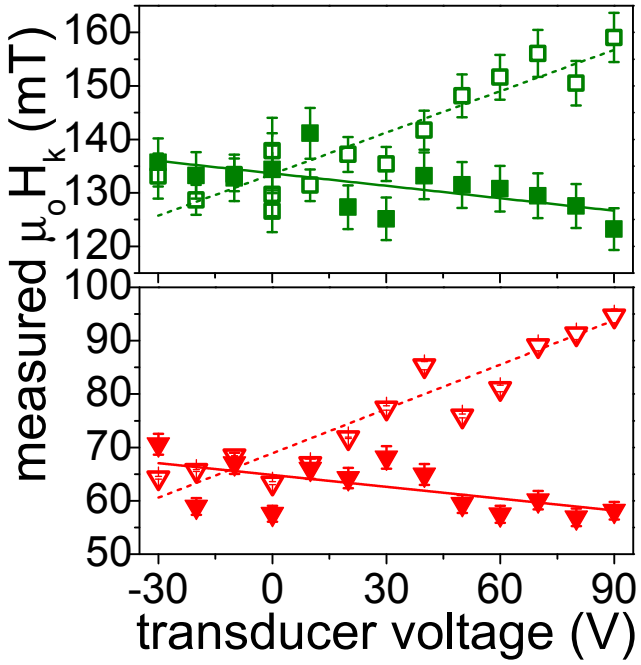


**Figure 4.7:** The measured magnetic anisotropy field is plotted against uniaxial transducer voltage for Pt/Co(t)/Pt thin films (t = 0.95, 1.0nm). The solid shapes are the data taken with the in-plane field applied along $\phi$=0$^o$ (as defined in the inset of Figure 4.4) and the open shapes are data taken with the in-plane field applied along $\phi$=90$^o$. The error bars are derived from the errors on the least squares fits to the raw data. The solid and dashed lines are linear, least squares fits to the solid and open points, respectively.

Strain from the uniaxial transducers gives rise to an in-plane anisotropy in Pt/Co/Pt, which would ordinarily have only PMA. In order to see how the PMA is affected, and to find the magnitude of the induced in-plane anisotropy, the expression given in Equation 2.3 for the magnetic anisotropy energy density of a system with a secondary uniaxial anisotropy axis is used. Setting $\theta = 90^o$ gives the anisotropy energy when the magnetisation has been saturated in-plane

$$E_{K_{IP}} = K_{measured} = K_z + K_{IP}\cos(2\phi), \tag{4.3}$$

where $K_z$ is the PMA constant and $K_{IP}$ is the anisotropy constant in the plane.

The measured anisotropy constants plotted against $\cos(2\phi)$ in Figure 4.8 were fitted with a least squares algorithm to Equation 4.3 to give the solid lines shown in the plots. The gradient gives the in-plane anisotropy constant and the intercept gives the out-of-plane anisotropy constant. The in-plane anisotropy energy contours, drawn using values from the

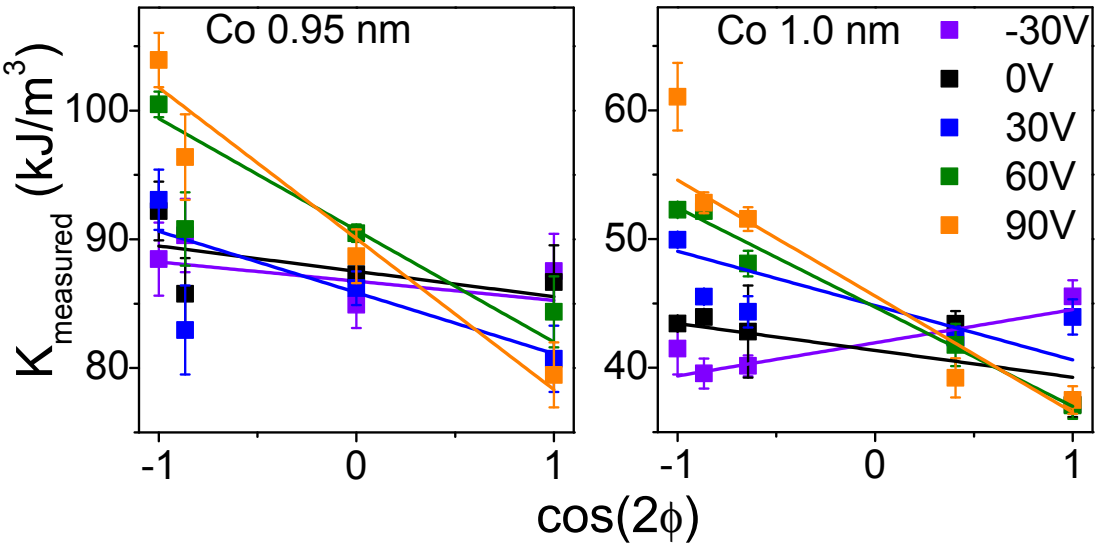


**Figure 4.8:** Measured anisotropy constants for Pt/Co(t)/Pt hall bars on uniaxial piezoelectric transducers set at voltages between -30 and 90 $V$ are plotted against $\cos(2\phi)$, where $\phi$ is the in-plane angle from the direction of current flow in the Hall bars. The Co thicknesses are labelled on the plot. The points are the data and the lines represent least squares fits to the data of Equation 4.3 for each transducer voltage.

fits, are shown in Figures 4.9a and 4.10a for the Pt/Co(t)/Pt Hall bars with t = 0.95, 1.0 $nm$. Straining the Pt/Co/Pt induces an in-plane anisotropy $K_{IP}$ of $\sim$10$kJ/m^3$; as tensile strain is applied along x for positive transducer voltages, the energy cost of aligning the magnetisation along x reduces, making this axis easier, while the y axis becomes harder under a corresponding compression.

At 0V, the PMA constants were (88 $\pm$ 1) $kJ/m^3$ for 0.95 $nm$ and (41.3 $\pm$ 0.9 )$kJ/m^3$ for 1.0 $nm$. These values are lower than the 0V values for the samples on biaxial transducers, but have a similar trend of decreasing anisotropy with increasing Co thickness. At positive voltage the z axis is compressed and the PMA increases. In Figures 4.9b and 4.10b the out-of-plane anisotropy constant increases with strain, but the change is smaller than the change in in-plane anisotropy.

Plotting the change in the anisotropy constants $\Delta K_z$ and $\Delta K_{IP}$ against the strain $\varepsilon_z$ and $\varepsilon_x$ allows for comparison with the magnitude of change in the PMA of Pt/Co/Pt on biaxial transducers. Figure 4.11 shows this for the two thicknesses of Co studied (t = 0.95, 1.0nm), along with a line showing the result of the fit to $\Delta K_z$ on the three biaxial Pt/Co/Pt samples. The uniaxial data generally follow this line closely. The similarity of

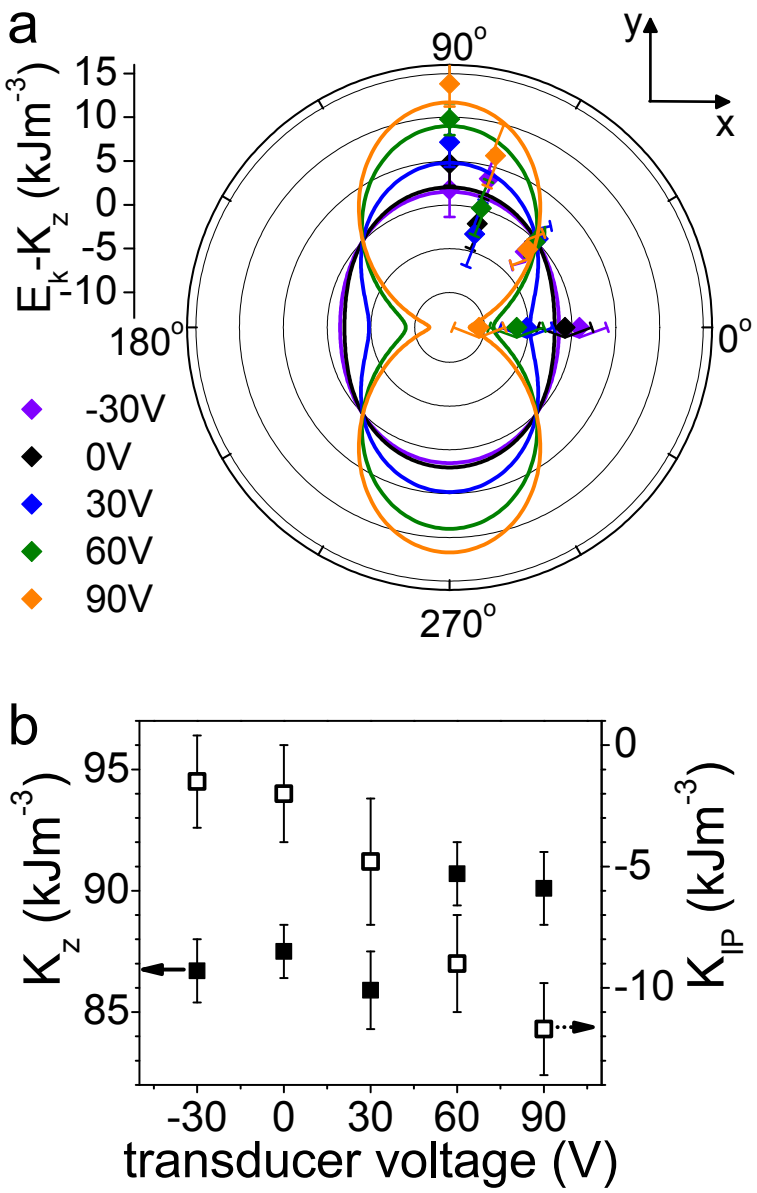


**Figure 4.9:** The in-plane and out-of-plane magnetic aniostropy energies, which were separated by fitting the data in Figure 4.8, are shown for Pt/Co(0.95nm)/Pt on a uniaxial transducer at voltages between -30V and 90V. a) The solid diamonds are the in-plane magnetic anisotropy energies $(E_k - K_z)$ plotted against the angle of the applied in-plane field ($\phi$=0$^o$ is the x axis and current direction). The solid lines are extrapolated using parameters from fits to the measured anisotropy data to Equation 4.3. b) The anisotropy constants extracted from the fits to Equation 4.3 are plotted against transducer voltage.

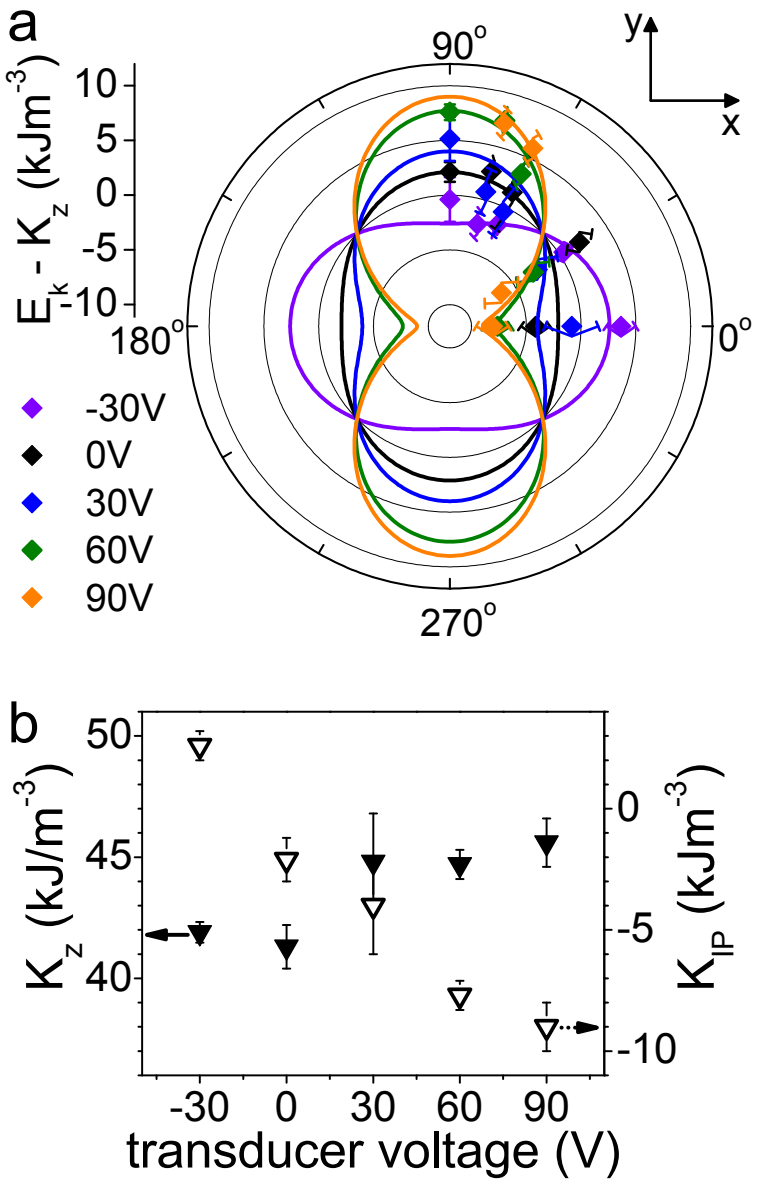


**Figure 4.10:** The in-plane and out-of-plane magnetic aniostropy energies, which were separated by fitting the data in Figure 4.8, are shown for Pt/Co(1.0nm)/Pt on a uniaxial transducer at voltages between -30V and 90V. a) The solid diamonds are the in-plane magnetic anisotropy energies $(E_k - K_z)$ plotted against the angle of the applied in-plane field ($\phi$=0$^o$ is the x axis and current direction). The solid lines are extrapolated using parameters from fits to the measured anisotropy data to Equation 4.3. b) The anisotropy constants extracted from the fits to Equation 4.3 are plotted against transducer voltage.

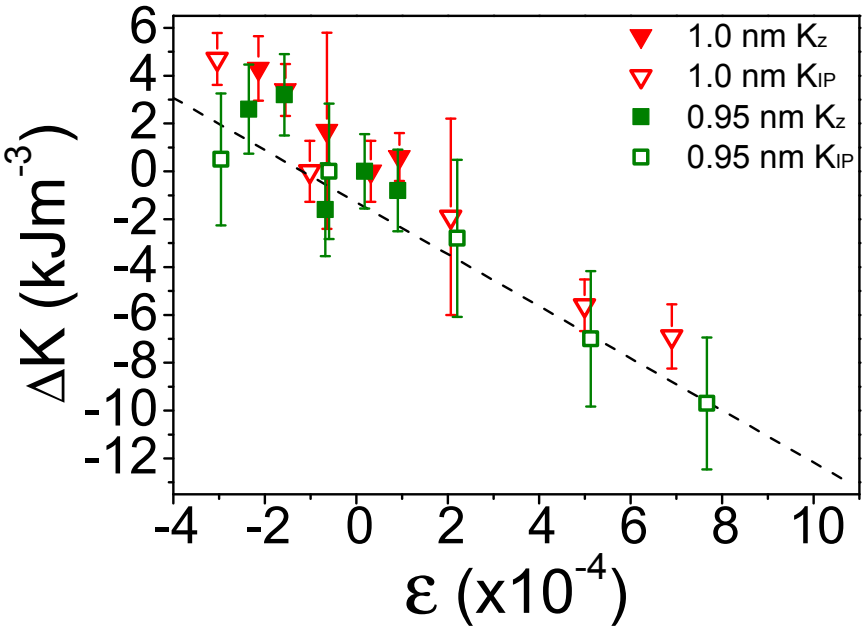


**Figure 4.11:** The changes in the magnetic anisotropy constants $K_z$ and $K_{IP}$ are plotted against the strain in the z and x directions respectively for Pt/Co(t)/Pt on uniaxial transducers (t = 0.95, 1.0nm). The dashed line is the fit to Equation 4.2 from Figure 4.6 showing the change in magnetic anisotropy for the Pt/Co/Pt on biaxial transducers for comparison.

the gradients of the data in the uniaxial plots to the gradient of the line from the biaxial plot shows that the magnetostriction constant (derived from the gradient using Equation 4.2) is the same along the x, y and z axes (see Chapter 3 for strain measurement details).

## 4.5 Summary

The magnetic anisotropy of Pt/Co/Pt thin films with PMA has been measured using a method based on the EHE. The behaviour of the magnetisation during magnetic field sweeps used for this measurement was characterised using Kerr microscopy. A coherent rotation regime at low applied magnetic fields was identified, which can be fitted to extract the anisotropy field.

Measurements of the change of magnetic anisotropy of Pt/Co/Pt under strain induced by biaxial and uniaxial transducers showed that tensile strain along a given axis lowers the magnetic anisotropy constant. The magnetostriction constant of Pt/Co(t)/Pt was measured to be $\lambda$ = -3.5$\times 10^{-5}$ on biaxial transducers for Co thicknesses of t = 0.85, 0.95, 0.1 $nm$. The change in magnetic anisotropy with strain was found to be due to bulk-like Co atoms, rather than the interface with Pt. Measurements on uniaxial transducers showed that the magnetostriction constant is isotropic and that an in-plane anisotropy can be established under anisotropic in-plane strain.

# Chapter 5

Measuring the Dzyaloshinskii-Moriya interaction

## 5.1 Introduction

The Dzyaloshinskii-Moriya interaction (DMI) is an anisotropic exchange interaction that promotes chiral spin structures such as Néel domain walls. In thin magnetic films with PMA, the presence of a DMI term manifests as an effective in-plane magnetic field within domain walls, perpendicular to the wall direction. The strength of the DMI field can be measured by seeing changes in domain wall velocity under applied in-plane bias fields. This chapter will describe the measurement technique and present results of DMI fields for thin films of Pt/Co/X (where X is Pt, Ir or Ir/Pt) with a range of Co thicknesses. The effect of using different out-of-plane fields to drive the domain walls and the effect of strain from biaxial transducers on these measurements is also explored.

## 5.2 Measuring DMI using the creep regime

Measurements of DMI from the field driven expansion of bubble domains under applied in-plane fields have been demonstrated in Pt/Co thin films by a number of different investigators [15; 16; 28; 57]. In these studies the domain wall motion is in the creep regime, so the domain wall velocity is expected to follow the creep law given in Equation 2.20 with a modification $\Gamma$ from the domain wall energy in an in-plane field. The velocity is given by

$$v = v_o \exp\left[-\frac{U_c}{kT}\left(\frac{H_{dep}}{H}\Gamma\right)^{1/4}\right], \tag{5.1}$$

where $\Gamma = \frac{\gamma_{DW}(H_{IP})}{\gamma_{DW}(H_{IP}=0)}$ is the ratio of the domain wall energy in an applied in-plane field to the energy in zero in-plane field. The field-dependent domain wall energy term (given in Equations 2.18 and 2.19) includes the DMI field and is different depending on whether the domain wall is truly in the Néel configuration

$$\gamma_{NW} = \gamma + 2K_D\delta - \pi\delta\mu_0 M_s|H_{IP} + H_{DMI}|$$

or retains some Bloch character

$$\gamma_{BNW} = \gamma - \frac{\delta(\pi\mu_0 M_s)^2}{8K_D}(H_{IP} + H_{DMI})^2.$$

Figure 5.1a shows the magnetisation directions within different domain wall types, while Figure 5.1b shows bubble domains expanding under applied in-plane fields, along with the direction of the DMI field within the domain walls. For these measurements the field is

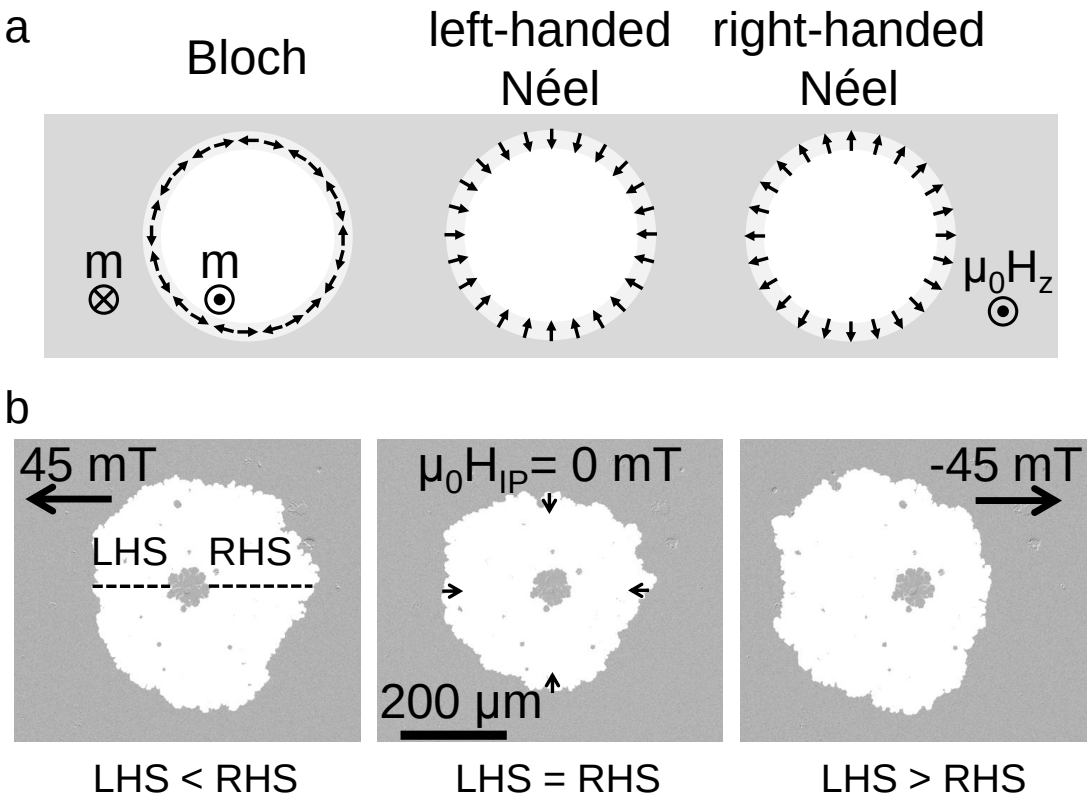


**Figure 5.1:** Bubble domains with magnetisation pointing up out-of-plane surrounded by a domain with magnetisation pointing down into-plane. a) Diagrams of bubble domains with arrows showing the magnetisation directions within domain walls of different structures. In Bloch walls the magnetisation points along the wall, in Néel walls the magnetisation is perpendicular to the wall. The Bloch wall contains sections of both chiralities, whereas Néel walls are either left-handed or right-handed. b) Kerr images of bubble domains used in DMI measurements. The central dark area is the original reversed domain and the bright area shows the expansion of the bubble under a pulse of out-of-plane magnetic field. The central image shows a symmetric bubble that has expanded with no in-plane bias field, with black arrows showing the direction of the DMI field that acts on the magnetisation within the domain walls to promote a Néel type wall. The images to the sides are bubbles that have expanded under an in-plane field in addition to the perpendicular driving field.

always applied along the x axis and velocities are measured parallel and anti-parallel to the field, as defined in the figure. The DMI field acts within a domain wall to promote a Néel component in the wall magnetisation, as shown in Figure 5.1. If there is no DMI ($H_{DMI} = 0$) the wall will be Bloch type at $H_{IP} = 0$ with an energy $\gamma = 4\sqrt{AK_{eff}}$, and the variation of the factor $\Gamma$ and the velocity with $H_{IP}$ will be the same on the RHS and

LHS of the bubble domain. For the case where $H_{DMI} \neq 0$, there is an effective in-plane DMI field that acts exclusively within the domain wall, countering the shape anisotropy $K_D$ associated with Néel walls. The magnetisation within the wall will then have some component that aligns to the DMI field. If the DMI field is large enough to fully overcome the shape anisotropy $K_D$, the wall will be fully Néel type, with the wall magnetisation arranged as in Figure 5.1.

Applying $H_{IP}$ results in a different $\Gamma$ dependence for the RHS and LHS, depending on the chirality of the Néel component in the wall. Since the DMI field points in opposite directions on the LHS and RHS of the bubble domain wall, $H_{IP}+H_{DMI}$ will vary differently with $H_{IP}$ for the RHS and LHS, causing $\Gamma$ and therefore the velocity to be different. For a wall that is Bloch when no in-plane field is applied ($H_{DMI} = 0$), the velocity versus in-plane applied field curves will rise symmetrically around $H_{IP} = 0$, since the Bloch-Néel wall energy gives

$$\gamma - \frac{\delta(\pi\mu_0 M_s)^2}{8K_D}(-H_{IP})^2 = \gamma - \frac{\delta(\pi\mu_0 M_s)^2}{8K_D}(+H_{IP})^2,$$

thus the curves for the RHS and LHS of the domain wall bubble will be the same. For a wall with some Néel component at zero applied in-plane field ($H_{DMI} \neq 0$), the velocity versus in-plane field curves will be shifted on the applied field axis by a value equal to the DMI field, since

$$\gamma - \frac{\delta(\pi\mu_0 M_s)^2}{8K_D}(-H_{IP} + H_{DMI})^2 \neq \gamma - \frac{\delta(\pi\mu_0 M_s)^2}{8K_D}(+H_{IP} + H_{DMI})^2.$$

The shift will be in opposite directions for the RHS and LHS of the bubble domain since the DMI field points radially in or out so has the opposite sign on these two sides. Figure 5.2 shows how the velocity of the LHS and RHS walls of a bubble domain with some Néel character depend on applied in-plane field. The curves are shifted in opposite directions along the $H_{IP}$ axis so that they are not symmetric around zero field. The DMI field is the field where the velocity is lowest. The minima of both curves, LHS and RHS, are identified by fitting the data to Equation 5.1 using the form with Bloch-Néel domain wall energy. Where the data fit well to the model around the minimum (as in Figure 5.2) the DMI field from the fit coincides with the minimum of the curve. The magnitudes of the values for the RHS and LHS are averaged to give the magnitude of the measured DMI field and the sign is determined by the direction of the shift of the RHS curve (positive when the RHS minimum is at a positive in-plane applied field, and negative when the RHS minimum is at a negative in-plane applied field).

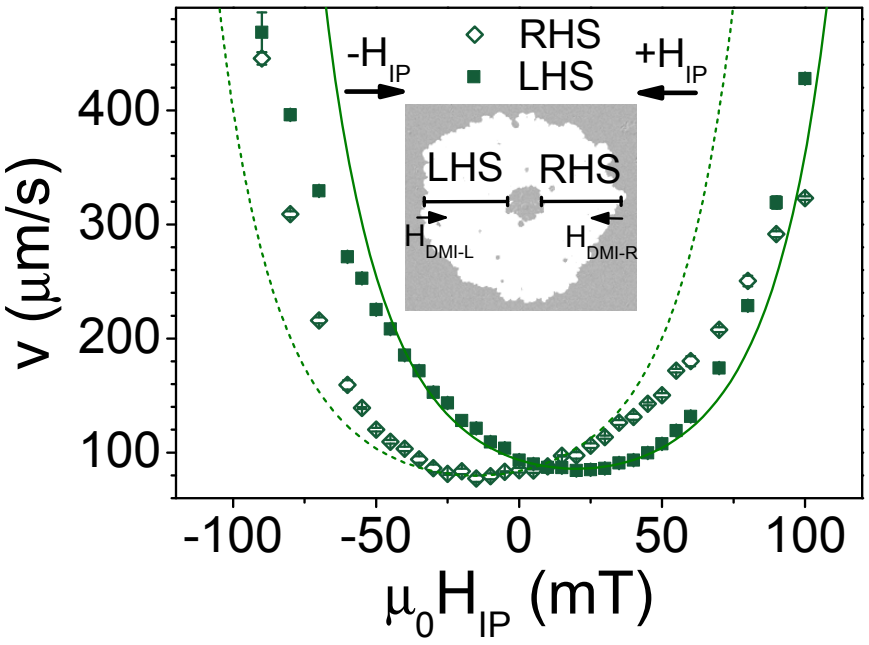


**Figure 5.2:** The magnitude of the domain wall velocity in Pt/Co(0.89nm)/Ir is plotted against in-plane bias field for the right hand side (RHS) and left hand side (LHS) of the bubble domain shown in the inset. The points are the data and the lines are least squares fits of the velocities at low fields to the creep model given in Equation 5.1. The domain wall is driven by a perpendicular field of $\mu_0 H_z = 11.2\ mT$. The bias field points towards the right of the inset for negative values and to the left for positive values of $\mu_0 H_{IP}$. These directions and the directions of the DMI field in the RHS and LHS domain walls are marked. The velocity error bars are the standard errors from averaging three or more velocities.

### 5.2.1 Samples

The thin films studied in this section were deposited by dc magnetron sputtering onto thin glass substrates and bonded to biaxial piezoelectric transducers, as described in Chapters 3 and 4. Four thin films were studied in order to examine the effect of different capping layers on the DMI, consisting of Ta(3.9nm)/Pt(4.2nm)/Co(t)/X, where X is Ir(6nm), Ir(0.3nm)/Pt(4.2nm) or Pt(4.2nm) with t = 0.89, 0.78 $nm$. The three Hall bar patterned films (Ta(4.5nm)/Pt(2.5nm)/Co(t)/Pt(1.5nm) with t = 0.85, 0.95, 1.0 $nm$) used for magnetic anisotropy measurements in Chapter 4, were also measured.

### 5.2.2 Experimental set-up and field alignment

A Kerr microscope was used to measure domain wall difference images, like those shown in Figure 5.1b, where the bright contrast is the area swept out by an expanding bubble domain. The dark area in the centre of this ring is the original reversed domain, while the dark area around the outside of the bright ring is the unreversed magnetisation. The out-of-plane fields needed to saturate the film, nucleate a reverse domain, then expand the bubble were applied with a perpendicular coil wound around a water-cooled brass pillar on top of which the sample was mounted. The top of the perpendicular coil and the sample were positioned between the pole pieces of an in-plane magnet. To make a measurement, the reverse domain is nucleated with just an out-of-plane field, then the in-plane field is applied continuously while the out-of-plane field is pulsed to expand the bubble.

In order to ensure that there is no additional out-of-plane field component, the in-plane bias field must be carefully aligned to the plane of the sample. A tilt of $0.1^o$ gives an extra contribution to $\mu_0 H_z$ of $\pm 0.2\ mT$ at $\pm 100\ mT$, so even with this small misalignment, there is a difference in driving field of 0.4 $mT$ between positive and negative in-plane fields of the same magnitude. Since velocity varies exponentially with $H_z$, the resulting velocity difference through a sweep of misaligned $\mu_0 H_{IP}$ can skew the shape of the curve, making the minimum difficult to identify.

In some cases, the field can be aligned by the same method used to align to an in-plane field for EHE measurements shown in Chapter 4. The in-plane field is swept while the out-of-plane signal (in this case using the polar Kerr effect rather than the EHE) is monitored. This is repeated with the magnet tilt adjusted until the change in signal during a field sweep is minimised. This method is more difficult when using MOKE rather than EHE because the Faraday effect in the objective lens gives a linear contribution to the signal that can be significant, and varies as the in-plane magnet is moved during the alignment. It is also only effective for films with an anisotropy field below the 280 $mT$ available from the in-plane magnet in this configuration. For most samples, the field was aligned by taking images of the domain wall displacement at large positive and negative in-plane fields for a given driving field and pulse time (e.g. $\mu_0 H_{IP} = \pm 80\ mT$, $\mu_0 H_z = 10\ mT$ pulsed for 1 $s$). The film is aligned when the total displacement on both sides of the bubble ($d_{total} = d_{RHS} + d_{LHS}$) is the same for positive and negative $\mu_0 H_{IP}$. Once the in-plane field is aligned the sample is left in place and measurements of DMI can be done while varying parameters such as driving field and transducer voltage.

## 5.3 Effect on DMI of driving field and biaxial strain

The DMI field was measured for different driving fields and under strain from biaxial transducers to investigate the effect these parameters have on the measured DMI field.

### 5.3.1 Driving field

To measure the domain wall creep velocity, an out-of-plane field must be applied to drive the domain wall motion. A Pt/Co(0.89nm)/Ir film on a biaxial transducer was measured with different driving fields. Figure 5.3 shows velocity versus in-plane bias field on the LHS and RHS of a bubble domain with four different driving fields between 10.06 and 11.21 $mT$. Increasing the driving field increases the domain wall velocity, as expected from the creep law (Equation 5.1), and also increases the steepness of the curve. The curves were fitted to Equation 5.1 to identify the minima, which give the DMI fields at each out-of-plane driving field. Figure 5.4 confirms that there is no significant change in the measured DMI field with driving field. The mean value is $\mu_0 H_{DMIav} = (16 \pm 1)\ mT$, where the error is the standard error.

For higher out-of-plane driving fields, the change of domain wall velocity with in-plane bias field is more pronounced, meaning that the minimum of the curve might be easier to determine, making higher driving fields better for measuring DMI. However, higher fields increase the likelihood of nucleating other bubble domains in the field of view of the microscope, so the driving field used must be a balance between being high enough to produce a pronounced $v$ versus $H_{IP}$ plot and not nucleating other domains which can interfere with the initial bubble.

The velocity versus in-plane field curves in Figure 5.3 fit well to the creep model with a Bloch-Néel wall energy around the minima, but deviate at higher fields. The creep model gives curves that are always symmetric around the DMI field at the minimum, whereas the measured curves appear tilted, with the velocity increasing much more steeply on one side than the other. To further investigate the effect of the in-plane field on the domain wall creep motion, the creep law was fitted to $\ln v$ versus $(\mu_0 H_z)^{-1/4}$ for each in-plane bias field and the gradients $(\mu_0 H_{dep})^{1/4} U_c/kT$ and intercepts of these are shown in Figure 5.5a. These data are limited by only having four out-of-plane driving fields and not covering a large range of velocities. However, the values of the creep parameters with no in-plane field applied are consistent with values from fits over a much larger field range with velocities spanning several orders of magnitude (see Chapter 6), so some tentative conclusions can

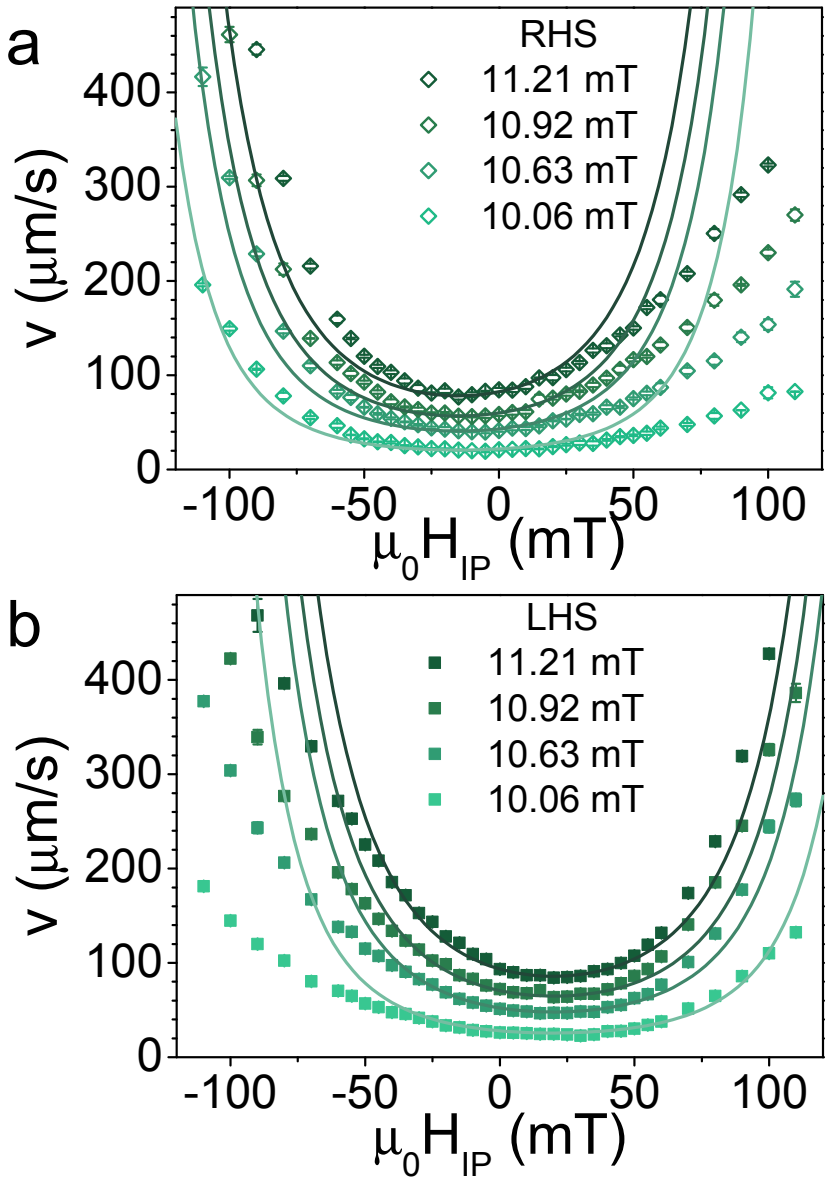


**Figure 5.3:** The magnitude of the domain wall velocity in Pt/Co(0.89nm)/Ir is plotted against in-plane bias field for a) the right hand side (RHS) and b) the left hand side (LHS) of a bubble domain. The domain walls are driven by the perpendicular fields $\mu_0 H_z$ given in the legends. The points are the data and the lines are least squares fits of the velocities at low fields to the creep model given in Equation 5.1.

be drawn from examining whether the parameters are affected by applying in-plane fields. Both of the parameters vary in a very similar way with $\mu_0 H_{IP}$: they increase as the field

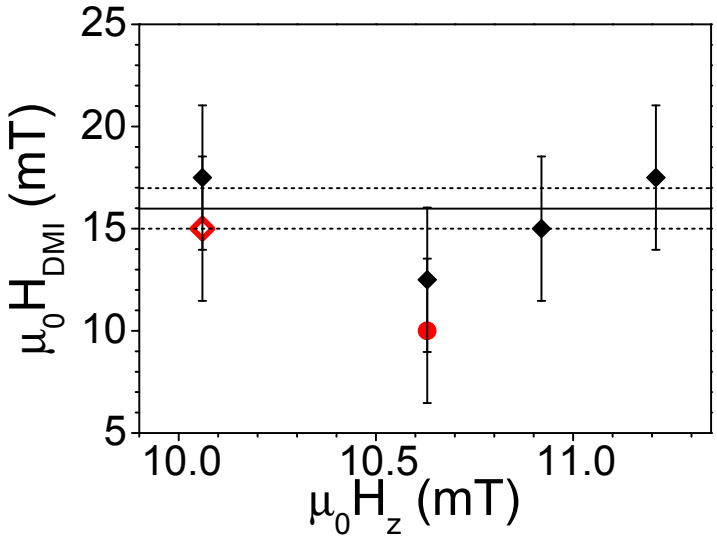


**Figure 5.4:** The DMI field in Pt/Co(0.89nm)/Ir is plotted against different perpendicular driving fields. The diamonds represent points taken before applying voltage to the transducer and the circle is a point taken during a sweep of the transducer voltage from -30 $V$ to 150 $V$. Between measuring the data for the open diamond point and the closed diamond points the in-plane field was re-aligned to the sample plane. The error bars are from the spacing between data points on the $v$ against $\mu_0 H_{IP}$ plots. The solid line is the average DMI field taken over the black symbols and the dashed lines show the standard errors on this value.

goes from negative, through zero, to positive, and the error bars are much larger at higher fields. Figure 5.5b shows that the $\ln v$ versus $(\mu_0 H_z)^{-1/4}$ plots for higher bias fields tend to deviate from linear behaviour, suggesting a move away from the creep regime or a small misalignment in the in-plane bias field. Since the kinks in the $\ln v$ versus $(\mu_0 H_z)^{-1/4}$ plots seem to turn the opposite way depending on whether the bias field is positive or negative, a small misalignment of the field is the most likely cause. In Figure 5.4 there are two values of DMI field measured at 10.06 $mT$, before and after realigning the in-plane field. The difference between these points is small compared to the spread of measurements at different fields and the error bars, showing that small differences in alignment do not change the measured DMI significantly.

For the velocity on the LHS of the bubble domain the creep parameters are almost constant with in-plane fields between -0.05 $T$ and 0.03 $T$, while the RHS parameters vary greatly over this range. The differences between the parameters on either side of the bubble and across applied bias fields may be caused by significant variations in the local pinning

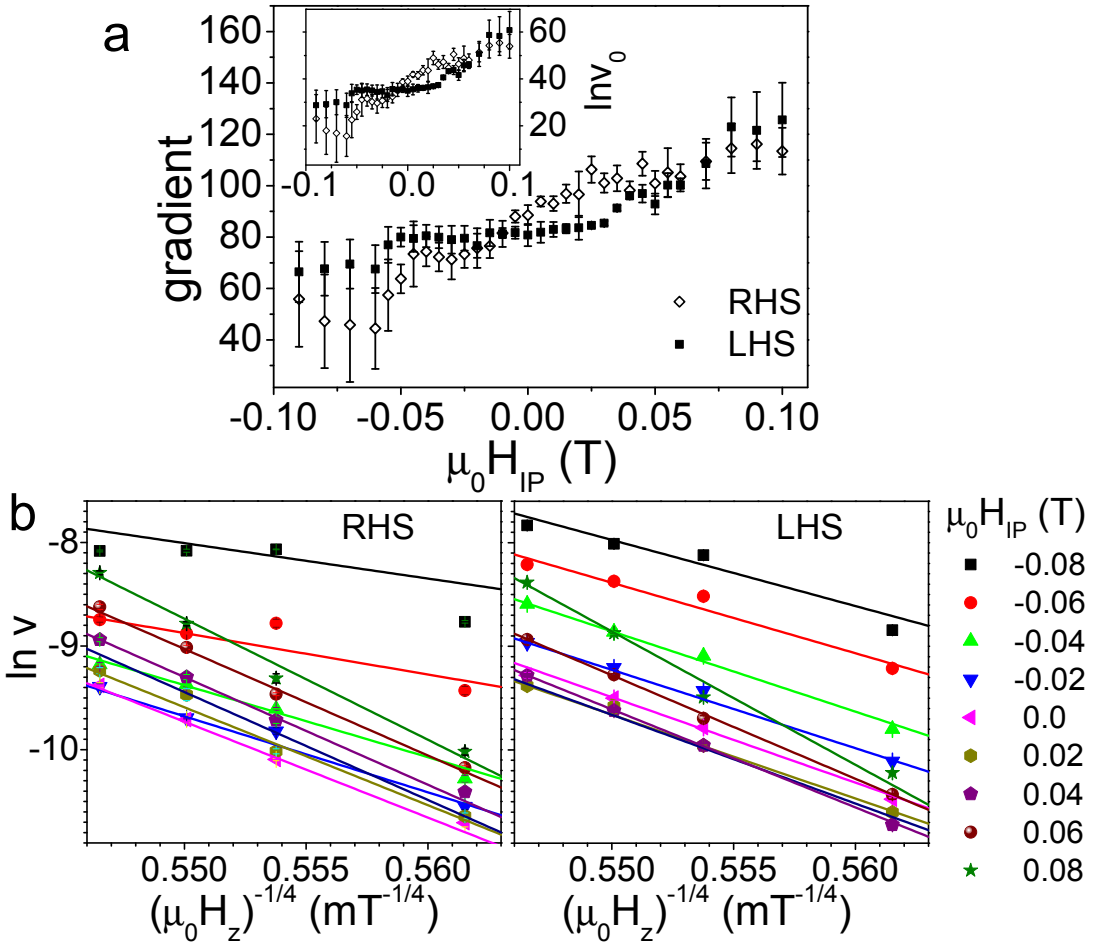


**Figure 5.5:** Domain wall creep parameters and velocities (taken from Figure 5.3) in Pt/Co(0.89nm)/Ir are shown. a) The domain wall creep parameters (the gradients $(\mu_0 H_{dep})^{1/4} U_c/kT$ and intercepts $lnv_0$) from linear least squares fits to the natural logarithm of the magnitude of the domain wall velocity $lnv$ versus the out-of-plane field $(\mu_0 H_z)^{-1/4}$ (where $\mu_0 H_z$ = 11.21, 10.92, 10.63, 10.06 $mT$) are plotted against in-plane bias field. b) Examples of the $lnv$ versus $\mu_0 H_z^{-1/4}$ plots for a range of in-plane fields on the RHS and LHS of bubble domains.

energy landscape. The regions where bubbles are most likely to nucleate at low out-of-plane fields tend to be rich in defects. As the bubble expands and the domain wall moves through the film it will be pinned more strongly and move more slowly in some areas, and can be seen to move faster in other areas. The in-plane field determines how far a domain wall moves for a certain field pulse, so that at higher in-plane fields the wall moves through more of the film, sampling more pinning sites, and close to the DMI field the wall moves

less far, sampling less of the film. These variations in pinning around the domain nucleation site, along with the different distances moved by the domain walls give an explanation for the observed variation of creep law parameters with in-plane bias field. Since the creep law seems to hold for applied in-plane bias fields close to the minima of the $v$ versus $\mu_0 H_{IP}$ plots, the measured DMI fields should be unaffected by deviations at higher applied fields.

### 5.3.2 Biaxial strain

The effect of strain from the transducer on the DMI measurement of Pt/Co(0.89nm)/Ir was investigated. Figure 5.6 shows the velocity versus in-plane bias field on the LHS and RHS of a bubble domain with the transducer at -30, 0, 100 and 150 $V$. The driving field was 10.6 $mT$ for all the data points in these plots. The effect of strain from the transducer is to increase the domain wall velocity for both sides of the bubble (this effect will be discussed in detail in Chapter 6). There is a small increase in the velocity change with in-plane field under tensile out-of-plane strain, but the minima of the curves do not change significantly. Figure 5.7 shows the DMI fields identified from the curves plotted against applied transducer voltage. The changes in the $v$ versus $\mu_0 H_{IP}$ plots under strain are similar to the changes seen for different fields, with no significant differences in the measured DMI fields. The average DMI field for different strains is $\mu_0 H_{DMIav} = (15 \pm 2)\ mT$, which is consistent with the average over different driving fields shown in Figure 5.4 ($\mu_0 H_{DMIav} = (16 \pm 1)\ mT$).

The $v$ versus $H_{IP}$ curves for Pt/Co(0.89nm)/Pt were also measured under strain. Figure 5.8 shows the $v$ versus $\mu_0 H_{IP}$ curves with the biaxial transducer at 0 and 150 $V$. The data in 5.8a and b were taken in different sessions so the alignment and in-plane direction of the bias field may be different, causing a small difference in velocity at $\mu_0 H_{IP} = 0\ mT$. The same difference in features can be seen here as in Pt/Co(0.89nm)/Ir: the curve shifts up as the velocity increases under strain, the difference at higher in-plane fields is more pronounced, but the velocity minima are in the same positions, giving the same DMI field.

These measurements show that the DMI field can be measured from the velocity minima of $v$ versus $\mu_0 H_{IP}$ curves with no significant influence from out-of-plane driving field, and that the DMI field is not affected by strain from the biaxial piezoelectric transducers.

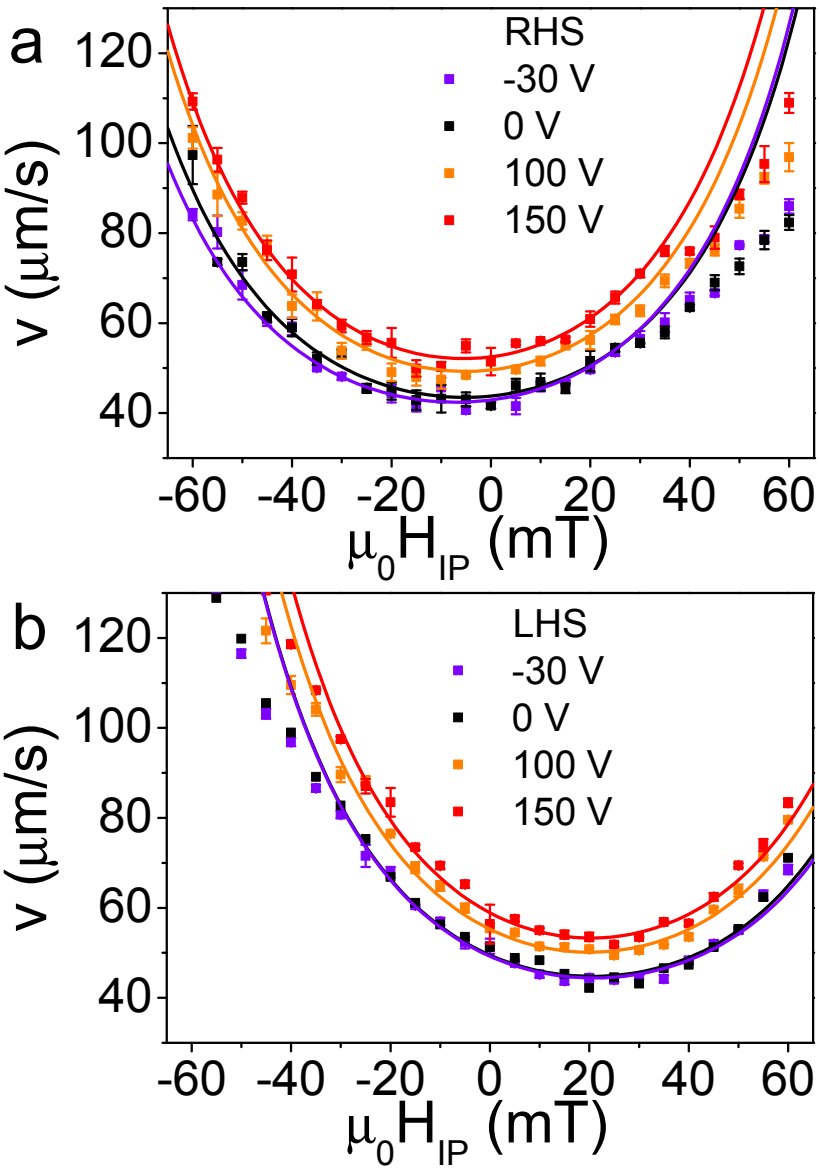


**Figure 5.6:** The magnitude of the domain wall velocity in Pt/Co(0.89nm)/Ir is plotted against in-plane bias field for a) the right hand side (RHS) and b) the left hand side (LHS) of a bubble domain. The thin film is bonded to a transducer to which voltages of between -30 $V$ and 150 $V$ have been applied to induce strain. The domain walls are driven by a perpendicular field of $\mu_0 H_z = 10.6\ mT$. The points are the data and the lines are least squares fits of the velocities at low fields to the creep model given in Equation 5.1.

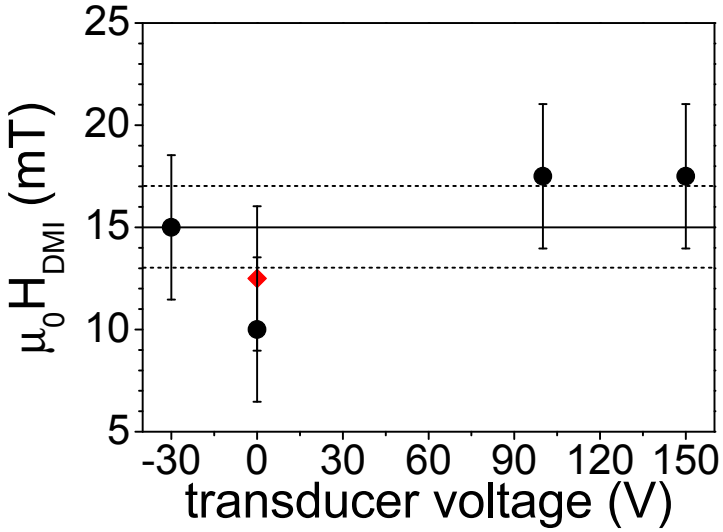


**Figure 5.7:** The DMI field in Pt/Co(0.89nm)/Ir is plotted against applied transducer voltages. The diamond represents a point taken before applying voltage to the transducer and the circles are points taken during a sweep of the transducer voltage from -30 $V$ to 150 $V$. The error bars are from the spacing between data points on the $v$ against $\mu_0 H_{IP}$ plots.The solid line is the average DMI field taken over the black symbols and the dashed lines show the standard errors on this value.

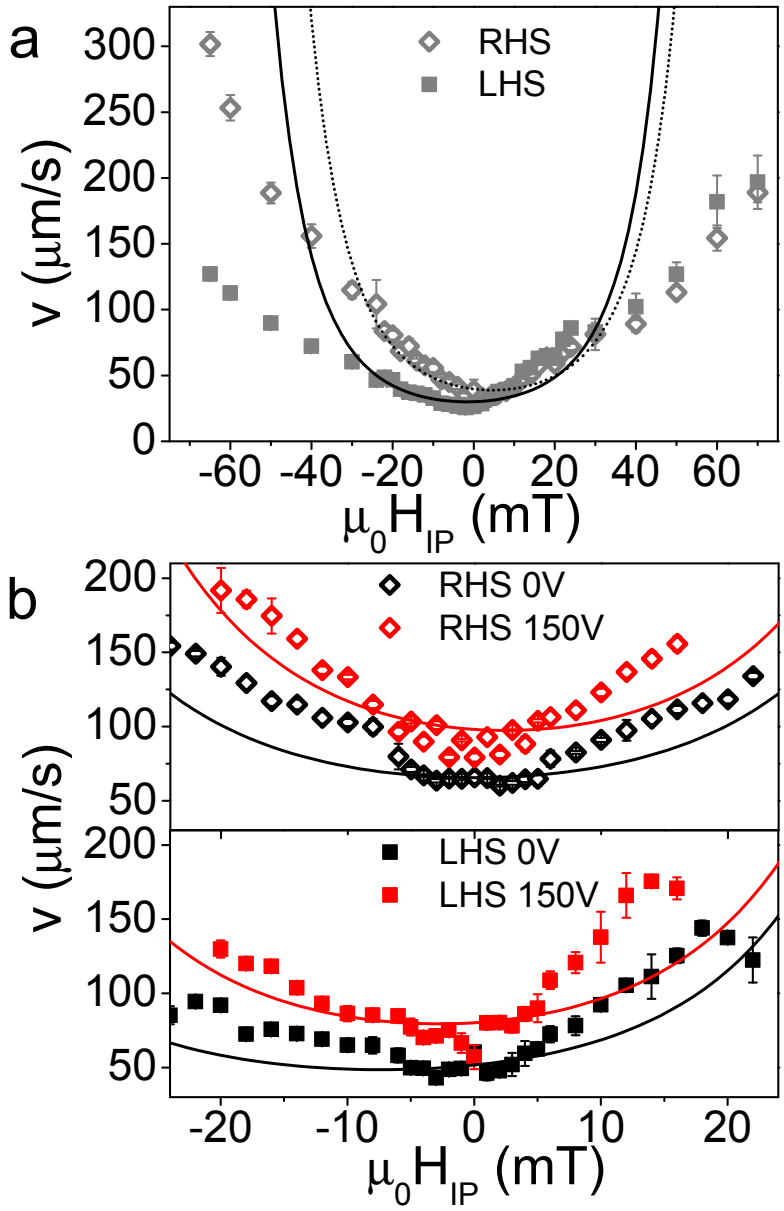


**Figure 5.8:** The magnitude of the domain wall velocity in Pt/Co(0.89nm)/Pt is plotted against in-plane bias field for the right hand side (RHS) and the left hand side (LHS) of a bubble domain. The domain walls are driven by a perpendicular field of $\mu_0 H_z = 14.4\ mT$. a) The RHS and LHS are plotted together against a large range of bias fields. b) The RHS and LHS are plotted on separate axes to compare the effect of holding the transducer at 0 $V$ and 150 $V$. The points are the data and the lines are least squares fits of the velocities at low fields to the creep model given in Equation 5.1. Since the data do not fit well to the model, the DMI field is taken at the centre of the minimum in the velocity curve.

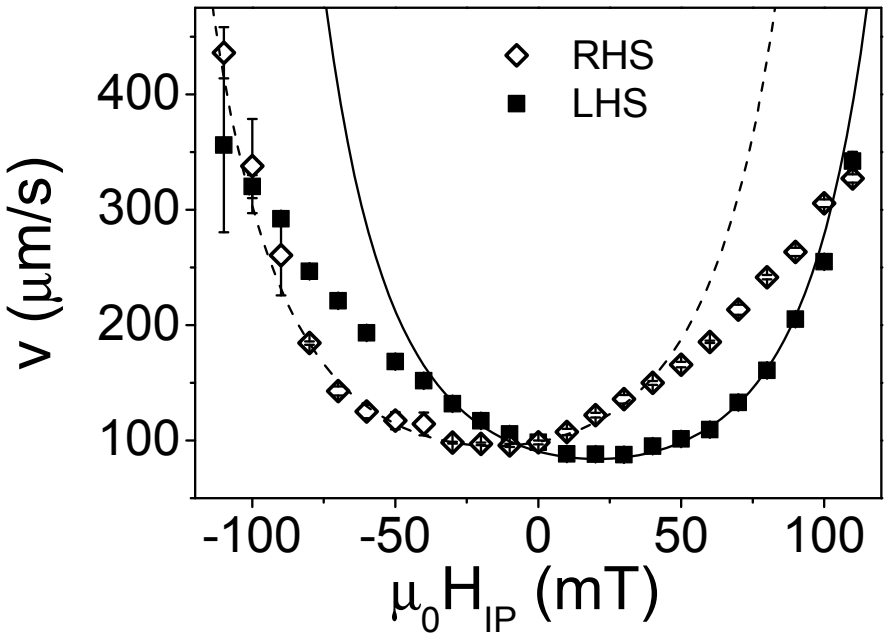


**Figure 5.9:** The magnitude of the domain wall velocity in Pt/Co(0.78nm)/Ir is plotted against in-plane bias field for the right hand side (RHS) and the left hand side (LHS) of a bubble domain. The domain walls are driven by a perpendicular field $\mu_0 H_z = 11.5\ mT$. The points are the data and the lines are least squares fits of the velocities at low fields to the creep model given in Equation 5.1.

## 5.4 Effect on DMI of varying Co thickness and capping layers

The DMI field was measured in Pt/Co thin films with different Co thicknesses and capping layers. The asymmetry between LHS and RHS velocity is discussed for the different films and the domain wall structure (Bloch or Néel) is deduced.

### 5.4.1 Velocity versus bias field curves and velocity asymmetry

Domain wall velocity versus in-plane field curves were measured for Pt/Co(0.89nm)/X for X=Ir, Ir/Pt and Pt, and for Pt/Co(0.78nm)/Ir. The films capped with Ir or Ir/Pt exhibit very similar behaviour. The $v$ versus $\mu_0 H_{IP}$ curves shown in Figures 5.2, 5.9 and 5.10 all have the RHS minimum at negative $\mu_0 H_{IP}$ and the LHS minimum at positive $\mu_0 H_{IP}$, giving a positive sign to the DMI. All the curves fit well to Equation 5.1 at low fields, with a smooth and approximately parabolic shape, although they are not quite symmetric around

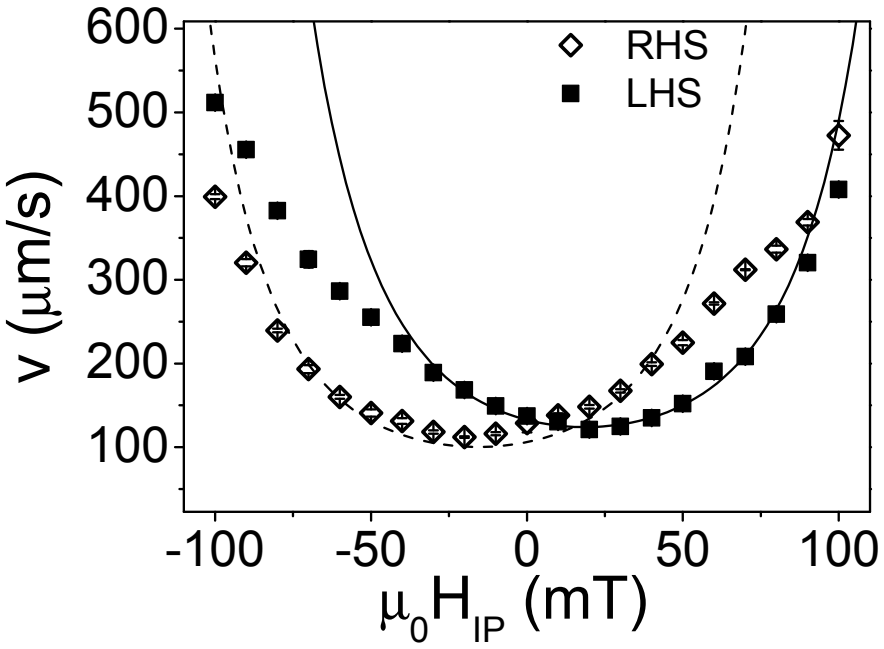


**Figure 5.10:** The magnitude of the domain wall velocity in Pt/Co(0.89nm)/Ir/Pt is plotted against in-plane bias field for the right hand side (RHS) and the left hand side (LHS) of a bubble domain. The domain walls are driven by a perpendicular field $\mu_0 H_z = 9.5\ mT$. The points are the data and the lines are least squares fits of the velocities at low fields to the creep model given in Equation 5.1.

their minima (i.e. one side of the curve rises away from the minimum faster) and they deviate from the fitted model at higher applied in-plane fields.

The domain wall velocity versus in-plane field curves for Pt/Co/Pt films differ from the films capped with Ir. The RHS and LHS curves for Pt/Co(0.89nm)/Pt both have an approximately flat region centred close to $\mu_0 H_{IP} = 0$, and above $\pm 5\ mT$ the velocity increases almost linearly. The patterned Pt/Co(t)/Pt films (t = 0.85, 0.95, 1.0 $nm$) have $v$ versus $\mu_0 H_{IP}$ curves (shown in Figure 5.11) that vary in shape, but with all the curves rising steeply away from zero on one side of the minimum (rising at positive field for the LHS and negative field for the RHS) and the velocity remaining low with increasing field on the other side. This feature is particularly marked in the t = 0.85 and 0.95 $nm$ films. The creep model fits well for the t = 0.85 $nm$ Co film over most of the measured field range, while the t = 0.89, 0.95 and 1.0 $nm$ Co films do not follow the model well. Comparing the shapes of velocity versus in-plane field curves for the thin films with the values for measured DMI fields shown in Figure 5.12, the films with larger DMI (the Ir and Ir/Pt capped films

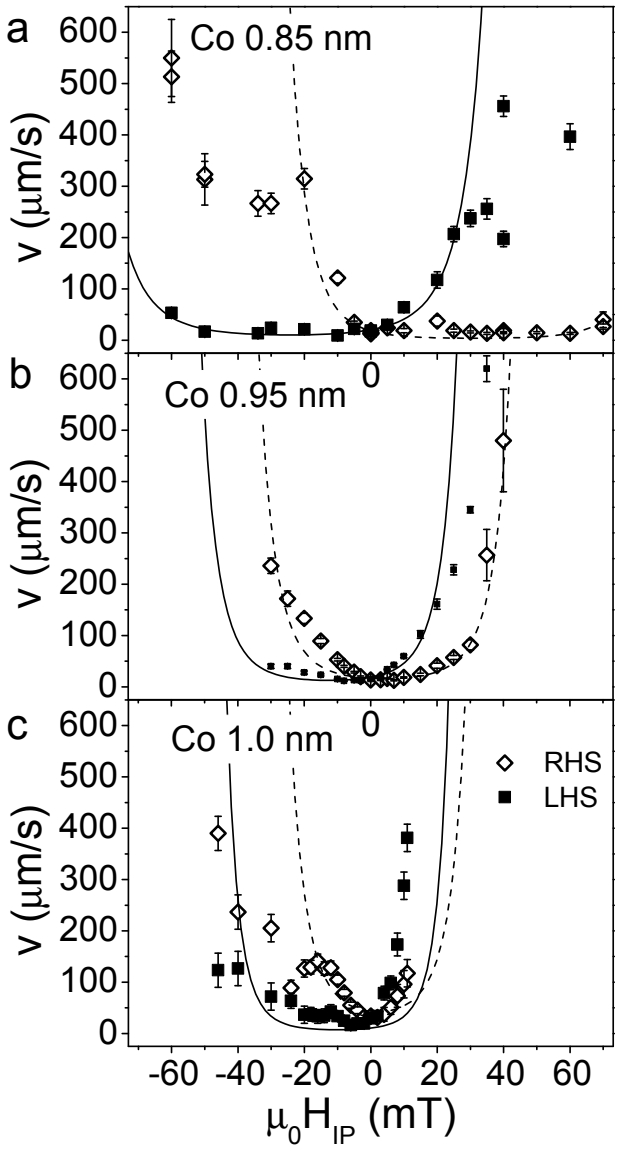


**Figure 5.11:** The magnitude of the domain wall velocity in patterned Pt/Co(t)/Pt films (t is marked on the plots) is plotted against in-plane bias fields for the right hand side (RHS) and the left hand side (LHS) of bubble domains in small areas of sheet film in a and b, and domains expanding along the Hall bar in c. The domain walls are driven by perpendicular fields of a) $\mu_0 H_z = 14.4$ $mT$, b) $\mu_0 H_z = 10.6$ $mT$ and c) $\mu_0 H_z = 11.2$ $mT$. The points are the data and the lines are least squares fits of the velocities at low fields to the creep model given in Equation 5.1. Where the data does not fit well to the model (Co 0.95 $nm$ and Co 1.0 $nm$) the DMI field is extracted as the field where the velocity is lowest.

and the t = 0.85 $nm$ Pt capped film) behave as the creep law in Equation 5.1 predicts more closely and over a larger field range.

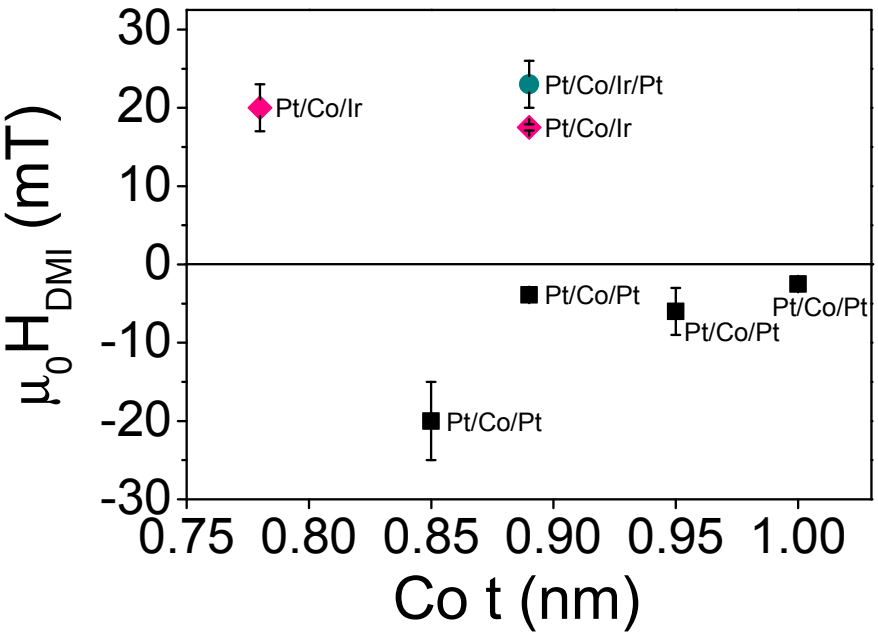


**Figure 5.12:** The DMI field in Pt/Co(t)/X (X = Ir, Pt or Ir/Pt) is plotted against Co thickness $t$. The error bars are from the spacing of the field steps in the $v$ versus $\mu_0 H_{IP}$ plots in the case where the curve minima are easy to define. In cases where the minima were hard to define the error bars are enlarged to reflect the ranges over which the minima could be positioned. The data points are labelled with the structures of the thin films.

The difference in the RHS and LHS velocity versus in-plane field curves can be studied further through the asymmetry, which is defined as the difference over sum of the RHS and LHS velocities

$$a = \frac{v_{RHS} - v_{LHS}}{v_{RHS} + v_{LHS}}, \tag{5.2}$$

where $v_{RHS}$ and $v_{LHS}$ are the magnitudes of the domain wall velocities on the RHS and LHS of the bubble. These velocities can also be calculated from the creep law (Equation 5.1) in order to fit the data to the model. The asymmetry eliminates symmetric effects from other properties of the film, such as the creep parameters (the gradient $(\mu_0 H_{dep})^{1/4} U_c/kT$ and intercept $lnv_0$) in the case where these are constant across the film and with applied in-plane fields, or where the RHS and LHS values have the same dependence on applied in-plane field.

Figure 5.13 shows the asymmetry for Pt/Co/Pt, Pt/Co/Ir and Pt/Co/Ir/Pt films. The asymmetry for Pt/Co(0.85nm)/Pt has a negative slope at low field then saturates at $a = 1$ at high fields, fitting well to the model derived from the creep law. The asymmetry for Pt/Co(0.89nm)/Pt is close to zero (meaning that $v_{RHS}$ and $v_{LHS}$ are similar) for positive applied fields, but increases away from $\mu_0 H_{IP} = 0$ at first for negative fields, then saturates at $a \approx 0.3$ at a field close to the minimum in the LHS velocity versus in-plane field curve. Since the asymmetry is close to zero, suggesting a very low DMI, the data do not fit well to Equation 5.2. The asymmetry of the t = 0.95 and 1.0 $nm$ Pt capped films has a similar shape to the t = 0.85 $nm$. The asymmetry fits well to Equation 5.2 at low fields, but for higher fields it saturates below $a = 1$. For the Ir and Ir/Pt capped films, the asymmetry fits well to the model for low fields, but reaches a maximum at approximately twice the DMI field, then reduces at higher positive or negative fields until the velocity on the RHS and LHS becomes similar around the limit of the measured field, even changing sign again in some measurements.

The differences between the measured asymmetry and the model based on the creep law suggest that the creep parameters change with field, as seen in Figure 5.5, or that there is some deviation from creep motion of 180$^o$ domain walls at high fields due to canting of the domain magnetisation or to Walker breakdown. However, the equations fit the data for low fields around the minima of the velocity versus in-plane field curves, showing that the model holds for the applied fields used to measured the DMI.

The variation of shapes exhibited by the $v$ versus $\mu_0 H_{IP}$ curves reflects the different curves measured by other investigators in similar thin films [15; 28; 57]. Most studies including $v$ versus $\mu_0 H_{IP}$ measurements have employed similar methods to that used here, taking the DMI from the minima in the curves, or fitting the expression given in Equation 5.1 to the data, although some have suggested alternative forms for the domain wall energy used in $\Gamma$ [77; 78]. Not all features in the different $v$ versus $\mu_0 H_{IP}$ curves have been explained by this simple model, which assumes that the in-plane field does not cant the magnetisation in the domains, and that the creep parameters ($lnv_0$ and the creep gradient) remain the same under applied in-plane field. Lavrijsen et al. have demonstrated for Pt/Co/Pt thin films [28] that the creep parameters can vary sharply even at small applied in-plane fields, and that the corresponding velocity versus in-plane field curves can take on forms that vary greatly from what is expected from the model, with peaks in the velocity near to $H_{IP} = 0$.

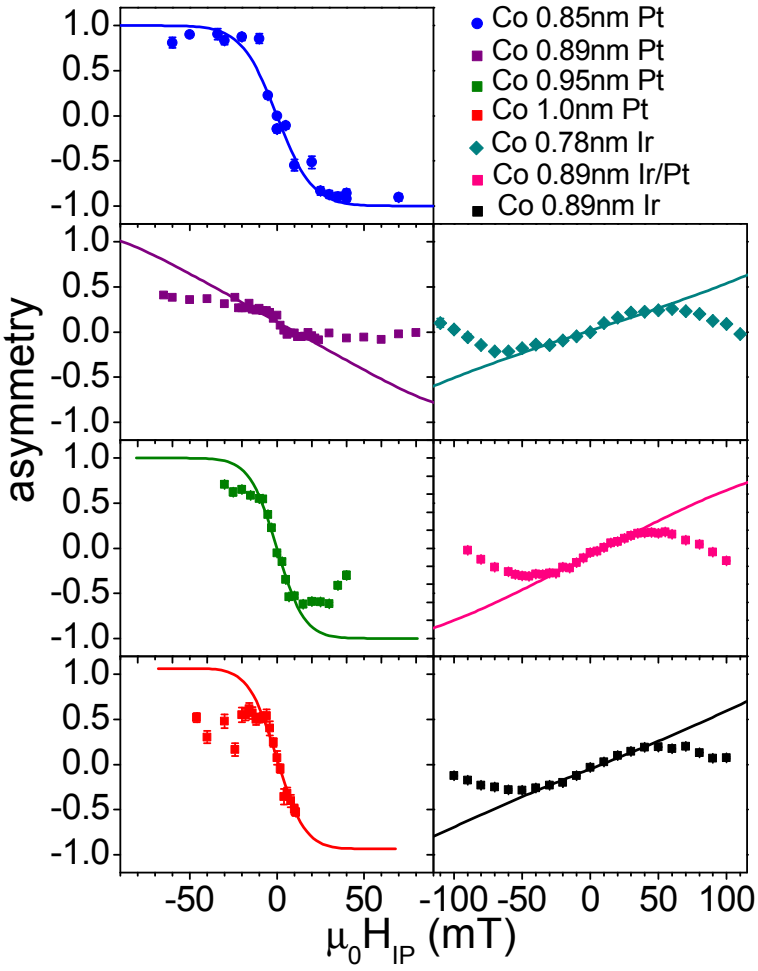


**Figure 5.13:** The asymmetry between right hand side (RHS) and left hand side (LHS) velocity (Equation 5.2) is plotted against in-plane bias field for Pt/Co/X films capped with Pt (right of figure), Ir or Ir/Pt (left of figure). The capping layers and Co thicknesses of the films are given in the legend and the t = 1.0, 0.95, 0.85 $nm$ samples are patterned, while the rest are sheet films. The points are the data and the lines are least squares fits to the creep model using Equation 5.2 where the velocities are calculated from Equation 5.1.

### 5.4.2 DMI fields and domain wall structure

The measured DMI fields for the films capped with Ir, Ir/Pt and Pt are plotted against Co thickness in Figure 5.12. Following Hrabec et al. [16], films capped with Ir and Ir/Pt have a positive DMI field, while films capped only with Pt have a negative DMI field. There is a slight trend in the Pt capped samples for smaller DMI fields at higher Co thicknesses. The Co thickness affects the strength of the PMA in Pt/Co films, shown by Figure 5.14a where the effective anisotropy constant is plotted against Co thickness for the films capped with Ir, Ir/Pt and Pt. The PMA was measured with polar MOKE and an in-plane applied field, using a similar procedure to that described in Chapter 4. The PMA generally decreases as Co thickness increases, and films capped with Ir or Ir/Pt have larger PMA than films capped with only Pt. Figure 5.14b shows the absolute value of the DMI field plotted against the effective anisotropy constant. The size of the DMI field is generally larger for films with higher PMA, although the trend is not strong. Some correlation between DMI field and PMA might be expected, since both are determined by the spin-orbit interaction and depend strongly on the Co interfaces.

A positive DMI promotes Néel walls with left-handed chirality, while a negative DMI promotes Néel walls with right-handed chirality. To fully transform a wall from Bloch to Néel, the wall shape anisotropy $K_D$ must be overcome, requiring an in-plane field of

$$\mu_0 H_{crit} = \mu_0 |H_{IP} + H_{DMI}| > \frac{4K_D}{\pi M_s} = \frac{2\mu_0 M_s t \ln 2}{\pi^2 \delta}. \tag{5.3}$$

Figure 5.15 shows this critical in-plane field and the absolute values of the measured DMI fields plotted against the ratio $t/\delta$. The domain wall width $\delta$ was calculated from $\delta = \sqrt{A/K_{eff}}$, where the exchange stiffness $A = 22\ pJ/m$ is taken from a calculated value for a similar Pt/Co(0.8nm)/Pt film in Ref. [22]. All except the Pt/Co(0.85nm)/Pt Hall bar have DMI field values below the critical field, meaning that without applying an in-plane bias field the DMI field is insufficient to make the domain walls fully Néel, so they remain Bloch-like. The Pt/Co(0.85nm)/Pt DMI field value sits just above the critical field so should be fully Néel, although it should be noted that the minima in the $v$ versus $\mu_0 H_{IP}$ curves for this sample were particularly difficult to determine, making the uncertainty in the DMI field large. Figure 5.15 shows that films with larger Co thicknesses or narrower domain wall widths require higher DMI fields for Néel walls to be possible. The Pt/Co films studied here are likely to have Bloch walls with a Néel component, or pure Bloch walls.

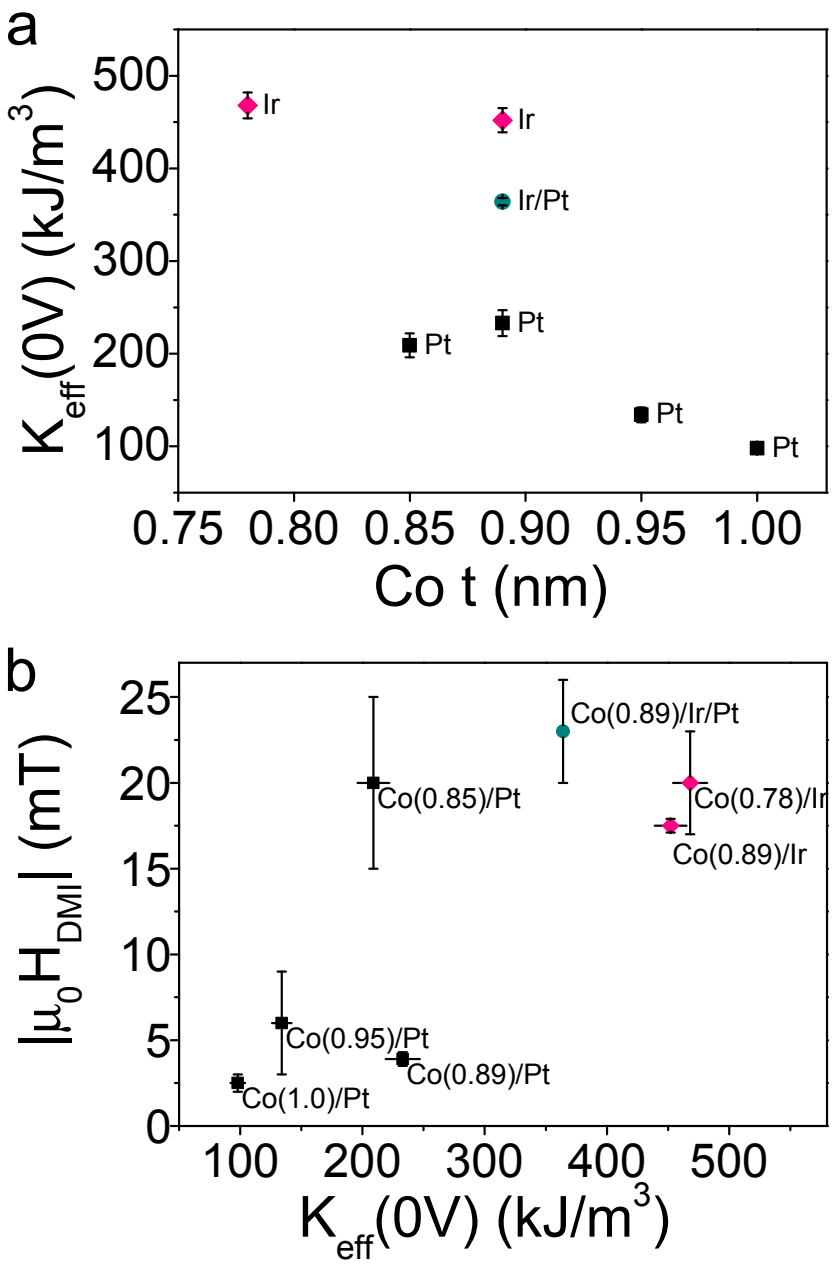


**Figure 5.14:** a) The effective anisotropy constants $K_{eff}$ of Pt/Co(t)/X (X = Ir, Pt or Ir/Pt) thin films are plotted against Co thickness $t$. b) The absolute value of the DMI field in Pt/Co(t)/X is plotted against $K_{eff}$. The data points are labelled with the Co thicknesses in $nm$ and capping layers of the thin films.

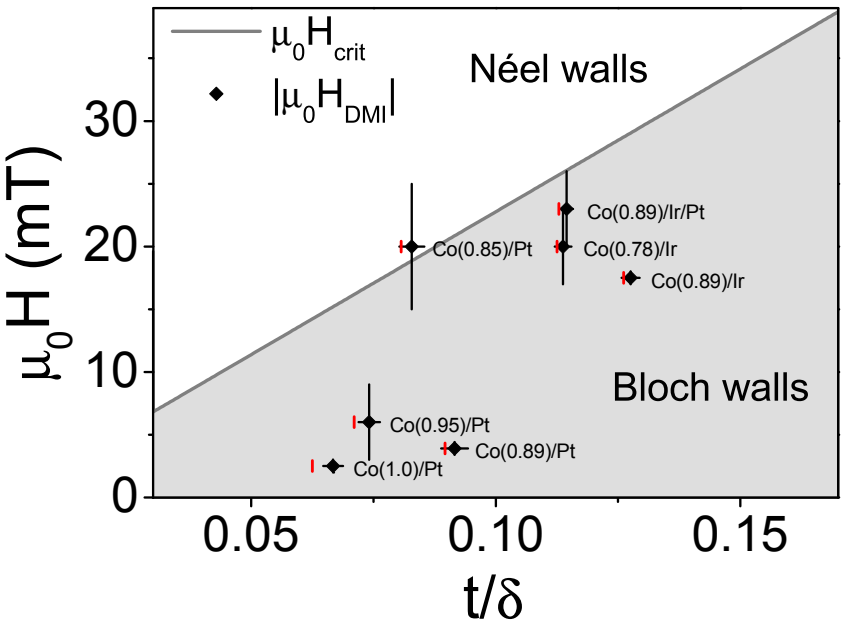


**Figure 5.15:** The critical in-plane field needed to transform a domain wall from Bloch to Néel type (Equation 5.3) is plotted against the ratio of film thickness to wall width $t/\delta$. The DMI fields for Pt/Co/X thin films with X = Ir, Ir/Pt or Pt are also shown, plotted against $t/\delta$ with the transducer at 0 V (black diamonds) and at 150 V (red lines). Films with data points in the grey region of the graph have measured DMI fields which are too small to give walls that are fully Néel. The data points are labelled with the Co thicknesses in $nm$ and capping layers of the thin films.

## 5.5 Summary

The DMI field has been measured for thin films of Pt/Co(t)/Ir (t = 0.78, 0.89 $nm$), Pt/Co(t)/Ir/Pt (t = 0.89 $nm$) and Pt/Co(t)/Pt (t = 0.85, 0.95, 1.0 $nm$). The velocity of domain walls on the right and left sides of bubble domains was measured under in-plane bias fields, and the DMI fields were extracted from the minima of these curves. The curves had different shapes and opposite asymmetry for films capped with Ir or Ir/Pt and films capped with Pt. All the films with Ir had a positive DMI field and the films capped with only Pt had a negative DMI field. A large enough positive DMI would give left-handed Néel walls and a large enough negative DMI would give right-handed Néel walls, although all but the Pt/Co(0.85nm)/Pt film had values of DMI field that were too small to fully transform the domain walls to Néel-type, so retain a predominantly Bloch-like form or have a combination of Bloch and Néel components. It was found that applying voltages to transducers coupled to the thin films to induce strain did not have a measurable effect on the DMI fields.

# Chapter 6

Magnetisation reversal and domain wall velocity change with strain in Pt/Co thin films

## 6.1 Introduction

In Chapter 4, it was shown that the magnetic anisotropy of Pt/Co(t)/Pt with t = 0.85-1.0 $nm$ can be modified by 10 $kJ/m^3$ by an out-of-plane tensile strain of 9x10$^{-4}$ from a biaxial transducer. In this chapter, the effect of strain, and the resulting anisotropy change, on magnetisation reversal is investigated. Strain-induced changes in magnetic anisotropy energy and hysteresis loops have been studied by other investigators in hybrid piezoelectric/ferromagnet heterostructures where the magnetic layer has either in-plane [36; 42; 43; 80–83] or perpendicular [39; 44; 84] magnetic anisotropy. Control of domain walls using the strain from a piezoelectric has been studied at room temperature in materials with in-plane anisotropy including FeGa thin films [82] , CoFeB [36] and CoFe [39] , and in (Ga,Mn)(As,P) with PMA at 90 K [45].

This chapter presents the changes in magnetic hysteresis loops of patterned Pt/Co/Pt multilayers under strain from biaxial transducers. The effect of strain from biaxial transducers on domain wall velocity in Pt/Co/X sheet and patterned films, where X is Ir, Ir/Pt or Pt, is investigated and discussed in the context of the structure and energy of domain walls.

## 6.2 Magnetisation reversal hysteresis loops in Pt/Co/Pt

The magnetisation reversal was studied by magnetic hysteresis loops using EHE and MOKE. The samples were Ta(4.5nm)/Pt(2.5nm)/Co(t)/Pt(1.5nm) (t = 0.85, 0.95, 1.0, 1.1 $nm$) multilayers, deposited onto 150 $\mu m$ thick glass substrates and patterned into 50 $\mu m$ wide Hall bars, and bonded with epoxy resin to biaxial piezoelectric transducers.

### 6.2.1 EHE hysteresis loops

The magnetisation reversal was first studied with EHE hysteresis loops. For Co thicknesses t of 0.85 $nm$, 0.95 $nm$ and 1.0 $nm$, the EHE signal was monitored while an out-of-plane magnetic field was swept from -30 $mT$ to +30 $mT$ and back, with a step size of 0.5 $mT$ around the magnetisation reversal. The 1.1 $nm$ Hall bar was measured with 5 $mT$ magnetic field steps around the coercive field, between -100 $mT$ and +100 $mT$. Figure 6.1 shows the hysteresis loops of the Pt/Co(t)/Pt Hall bars on biaxial transducers. For Co thicknesses t of 0.85 $nm$, 0.95 $nm$ and 1.0 $nm$ the hysteresis loops exhibit the square shape typical of an easy axis loop in a PMA material, with full remanence at 0 $mT$ and sharp switching

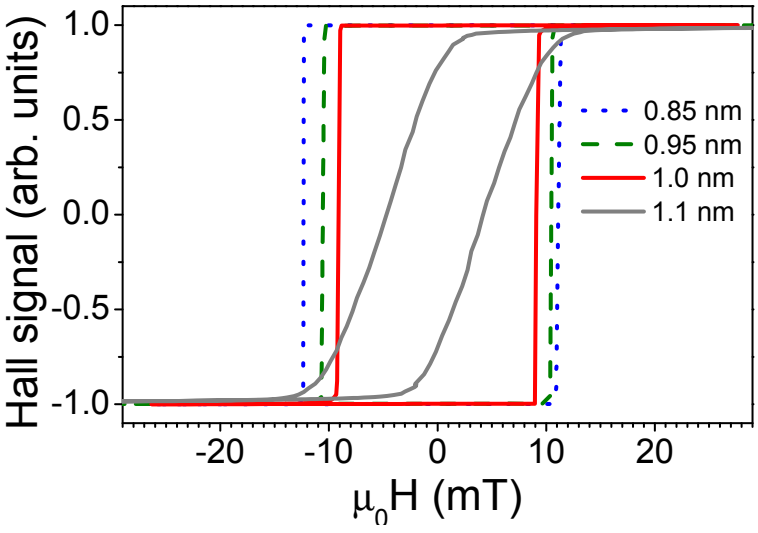


**Figure 6.1:** Normalised EHE hysteresis loops of Pt/Co(t)/Pt on biaxial transducers at 0 $V$ (t = 0.85, 0.95, 1.0, 1.1 $nm$). The magnetic field is applied perpendicular to the plane of the sample.

over a small range of applied field (1 $mT$ or less). The coercive field at 0 $V$ decreases as the Co thickness increases, with values of 11.7 $mT$, 10.2 $mT$ and 9.1 $mT$ for the t = 0.85 $nm$, 0.95 $nm$ and 1.0 $nm$ respectively. For 1.1 $nm$ of Co, the hysteresis loop has a much lower coercive field of 4.5 $mT$ and is not fully remanent at 0 $mT$, showing that it is at the reorientation transition between out-of-plane and in-plane magnetic anisotropy.

EHE hysteresis loops were taken with the biaxial transducers at a range of voltages between -30 $V$ and 150 $V$. The coercive fields were found at each voltage and the mean was taken over 5 magnetic field cycles. Figure 6.2 shows that the coercive fields of the four Pt/Co/Pt Hall bars decrease as a function of transducer voltage. The change in Pt/Co(0.85nm)/Pt with voltage is very small at only -0.15 $mT$, whereas the change for the thickest film Pt/Co(1.1nm)/Pt is much larger at -0.9 $mT$. Figure 6.3 shows that the absolute change in coercive field is proportional to the film thickness, with a larger reduction in coercive field as the films become thicker. The changes in coercive field are small compared to field step sizes, which contributes to some deviation from linear behaviour. The percentage change of 20 % in Pt/Co(1.1nm)/Pt is considerably larger than the change in the other three samples, which are all below 5 %.

When a voltage is applied to the biaxial transducers, the hysteresis loops of the three thinner Pt/Co/Pt samples remain square and fully remanent at 0 $mT$, with the nucleation field shifting by approximately the same field as the coercivity. The thicker Pt/Co(1.1nm)/Pt

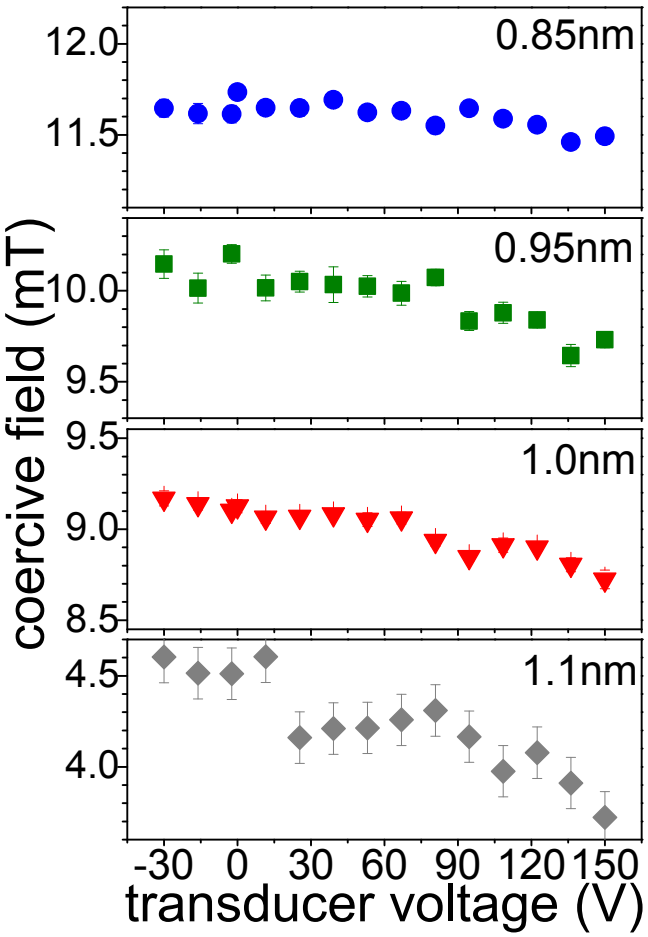


**Figure 6.2:** The coercive field of Pt/Co(t)/Pt on biaxial transducers measured using the EHE is plotted against transducer voltage for t = 0.85, 0.95, 1.0, 1.1 $nm$.The error bars are standard errors from averaging the coercive fields of 5 hysteresis loops All four panels have the same y scale.

becomes more canted as well as narrower when a positive voltage is applied to the transducer (Figure 6.4a). The squareness, measured as the ratio of the remanent EHE signal to the saturated EHE signal $R_{rem}/R_{sat}$, is shown as a function of transducer voltage in Figure 6.4b. The remanence reduces by 31% between 0 $V$ and 150 $V$, reducing the squareness from 0.65 of the saturated value to 0.45.

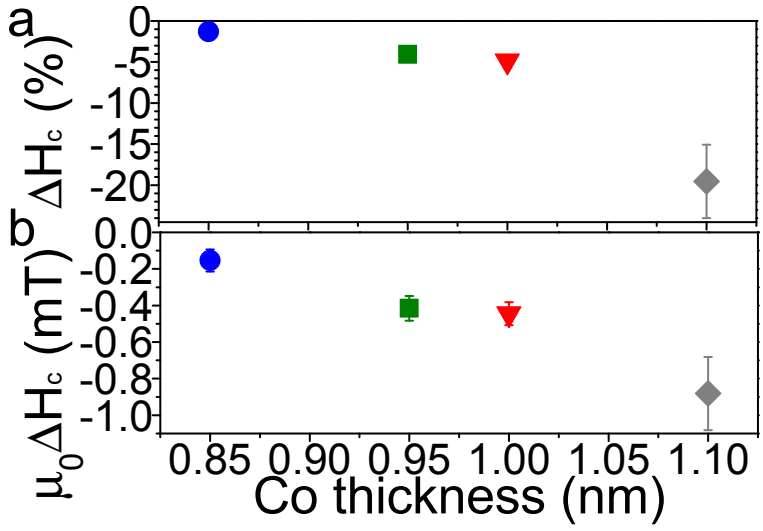


**Figure 6.3:** The absolute change and percentage change in the coercive field of Pt/Co(t)/Pt on biaxial transducers is plotted against Co thickness. The change is measured by EHE with out-of-plane applied magnetic field, between transducer voltages of 0 $V$ and 150 $V$.

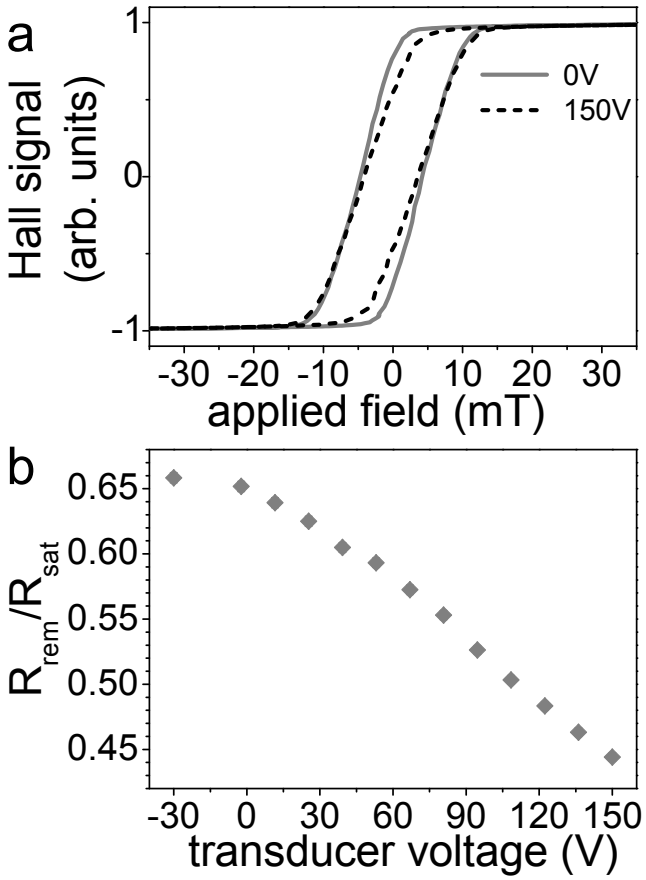


**Figure 6.4:** a) Out-of-plane EHE hysteresis loops of Pt/Co(1.1nm)/Pt on a biaxial transducer set at 0 $V$ and 150 $V$. b) Squareness of the EHE hysteresis loops (from extraordinary Hall resistances $R_{rem}/R_{sat}$) is plotted against transducer voltage for Pt/Co(1.1nm)/Pt on a biaxial transducer.

### 6.2.2 MOKE hysteresis loops

EHE hysteresis loop measurements showed how the coercive field and remanence of Pt/Co/Pt in the intersection of the Hall crosses changes as the PMA is modified by strain. Hysteresis loops were also measured using the Kerr microscope in polar MOKE configuration, with the biaxial stressors at 0 $V$ and 150 $V$. These measurements were taken over the regions used for domain wall velocity measurements in Pt/Co(t)/Pt (t = 0.85 $nm$, 0.95 $nm$ and 1.0 $nm$), to give the values of coercive field which will be used in Section 6.3.1 to calculate the domain wall pinning energy ratio. The sizes of the measured areas were up to 1.5×1.5 $mm^2$, in contrast to the smaller regions of 20×50 $\mu m^2$ at the Hall cross intersections measured using the EHE. The field was swept between -30 $mT$ and +30 $mT$ with a field step size of 0.1 $mT$ around the magnetisation reversal. The hysteresis loops are shown in Figure 6.5a and the coercive fields and changes between 0 $V$ and 150 $V$ are shown in Figure 6.5b. The coercive fields decrease with Co thickness but are higher than those measured using EHE. The difference between the two methods (EHE and MOKE) is due mainly to the difference in size and position of the measured area - the EHE samples only the area of the Hall bar between the arms used to measure the EHE voltage, whereas the Kerr microscope measures a much larger area.

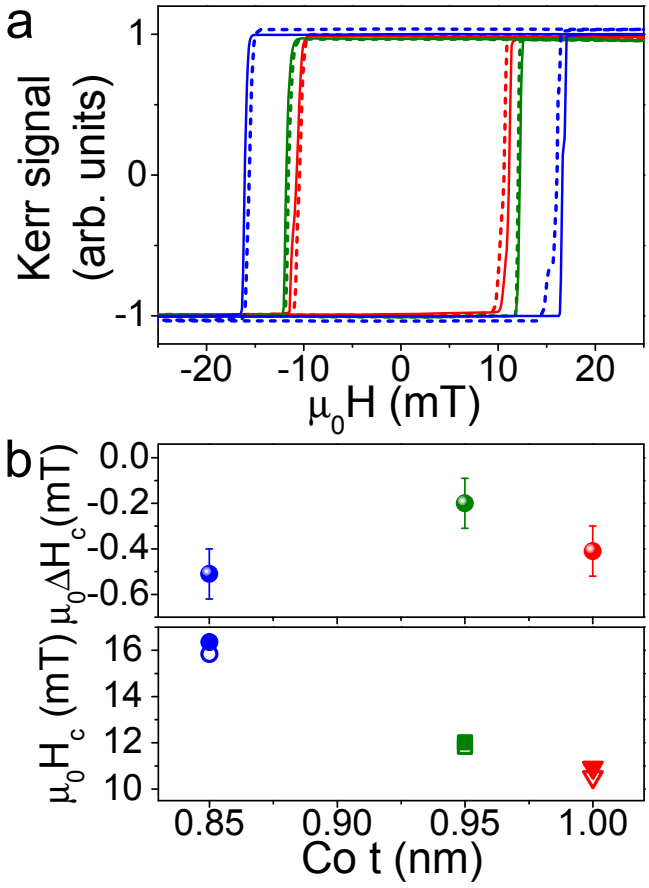


**Figure 6.5:** a) Out-of-plane hysteresis loops measured using the Kerr effect are shown for Pt/Co(t)/Pt on biaxial transducers at 0 $V$ (solid lines) and 150 $V$ (dashed lines) for Co thickness t of 1.0 $nm$ (red), 0.95 $nm$ (green) and 0.85 $nm$ (blue). b) Coercive field change and coercive field of Pt/Co(t)/Pt plotted against Co t. The coercive field $\mu_0 H_c$ is the mean of the values from 5 field cycles and is shown at 0 $V$ (filled shapes) and 150 $V$ (open shapes).

### 6.2.3 Pt/Co/Pt hysteresis loops under strain

Studying the magnetisation reversal through EHE and MOKE hysteresis loops shows that tensile out-of-plane strain of $\varepsilon_z = 9{\times}10^{-4}$ from a biaxial transducer reduces the coercivity of the Pt/Co/Pt with PMA by up to 5 %. The coercive field of Pt/Co/Pt at the reorientation transition between in-plane and out-of-plane magnetic anisotropy changed by 20 % and its remanence changed by 31 %.

The changes presented here can be compared to changes in hysteresis loops under strain of similar materials on piezoelectric substrates. Yang et al. [83] found changes in the coercive field and remanence of hysteresis loops from a CoPt alloy with in-plane aniostropy on a piezoelectric PMN-PT substrate which gave a biaxial strain of 0.17 %. With the field applied in-plane, the change in the coercivity was 26 %, which is slightly higher than the largest change seen here, and the change in the remanence was approximately 10 %, which is less than the change in the Pt/Co(1.1nm)/Pt Hall bar. Changes in the squareness of out-of-plane hysteresis loops from CoPd on piezoelectric substrates have been reported [44; 84]. In out-of-plane hysteresis loops of CoPd on PZT, which, like those for the Pt/Co(1.1nm)/Pt Hall bar, are not fully remanent, there is a maximum change in squareness between 0.9 and 0.6. Out-of-plane hysteresis loops of CoPd on PMN-PT change from being almost fully remanent with a squareness just below 1.0 to a squareness of 0.2. Lei et al. [85] studied the out-of-plane hysteresis loops of a PMA Pd/Co/Pd/Co/Pd/CoFeB/Pd multilayer on PMN-PT. The already low coercive field reduced by ∼50 % and the nucleation field changed from ∼1.5 $mT$ to ∼0.1 $mT$ when the maximum strain was applied.

The changes in the hysteresis loops of Pt/Co/Pt are generally smaller than previously reported changes for similar materials under piezoelectric strain. Comparing the results of Pt/Co/Pt, CoPt and CoPd, the largest changes in the magnetisation reversal under strain are seen in thicker films (the thicknesses of the CoPt and CoPd alloys are well above the Pt/Co/Pt thicknesses) with low magnetic anisotropy, coercivity or remanence.

The reduction of the coercive field under tensile strain in Pt/Co/Pt may be the result of two effects: the smaller nucleation field seen in the hysteresis loops, or a change in domain wall motion under strain. The following section investigates how the domain wall velocity in Pt/Co thin films is affected by PMA changes under strain.

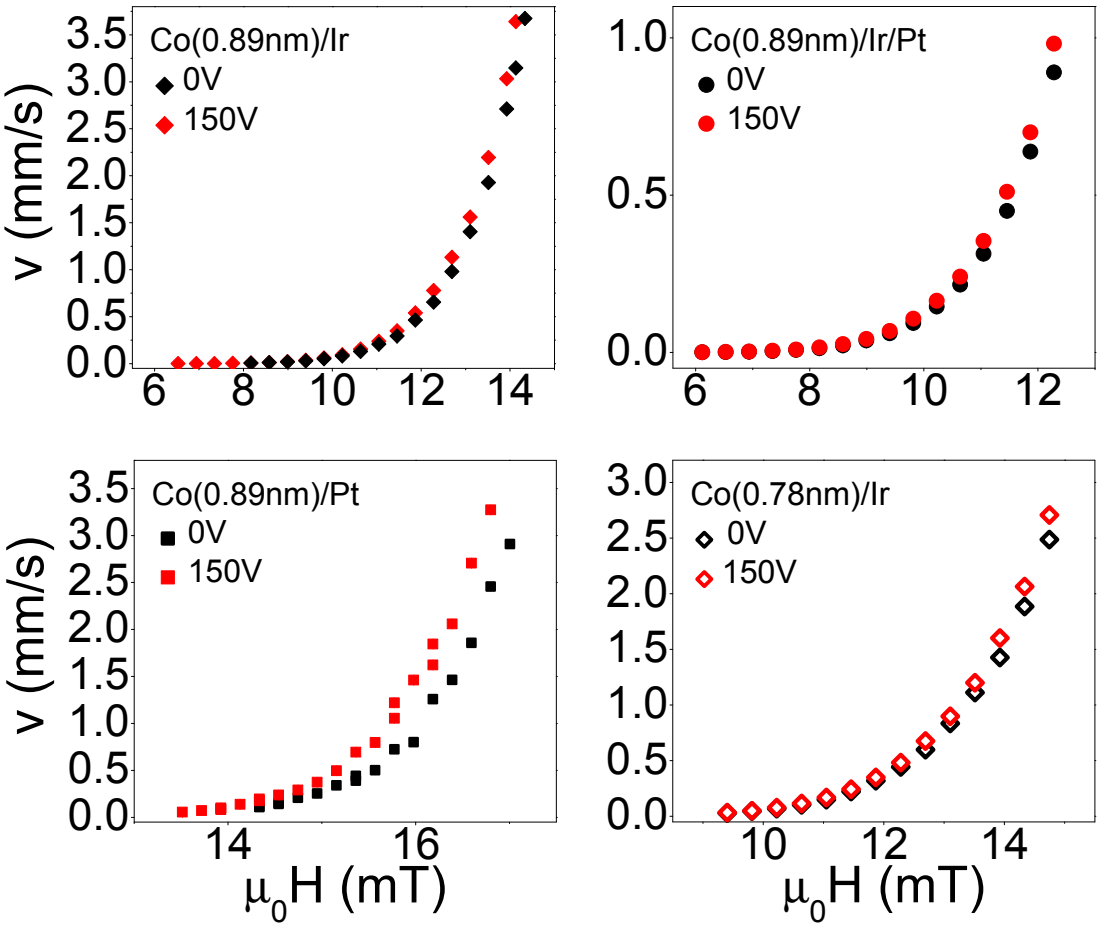


**Figure 6.6:** Domain wall velocity v plotted against applied out-of-plane field $\mu_o H$ for unstrained Pt/Co/X (black shapes) and Pt/Co/X under tensile out-of-plane strain induced by applying 150 $V$ to the piezoelectric transducers (red shapes). The Co thicknesses and the capping layers are given in the legends.

## 6.3 Effect of strain on domain walls in Pt/Co

The magnetisation reversal was investigated further by studying domain wall creep velocity using wide-field Kerr microscopy. The thin films studied in this section were deposited by dc magnetron sputtering onto thin glass substrates and bonded to biaxial piezoelectric transducers. Four sheet thin films were studied, consisting of Ta(3.9nm)/Pt(4.2nm)/Co(t)/X, where X is Ir(6nm), Ir(0.3nm)/Pt(4.2nm) or Pt(4.2nm) with t = 0.89, 0.78 $nm$. Three Ta(4.5nm)/Pt(2.5nm)/Co(t)/Pt(1.5nm) films with t = 0.85, 0.95, 1.0 $nm$, patterned into

Hall bar structures, were also measured.

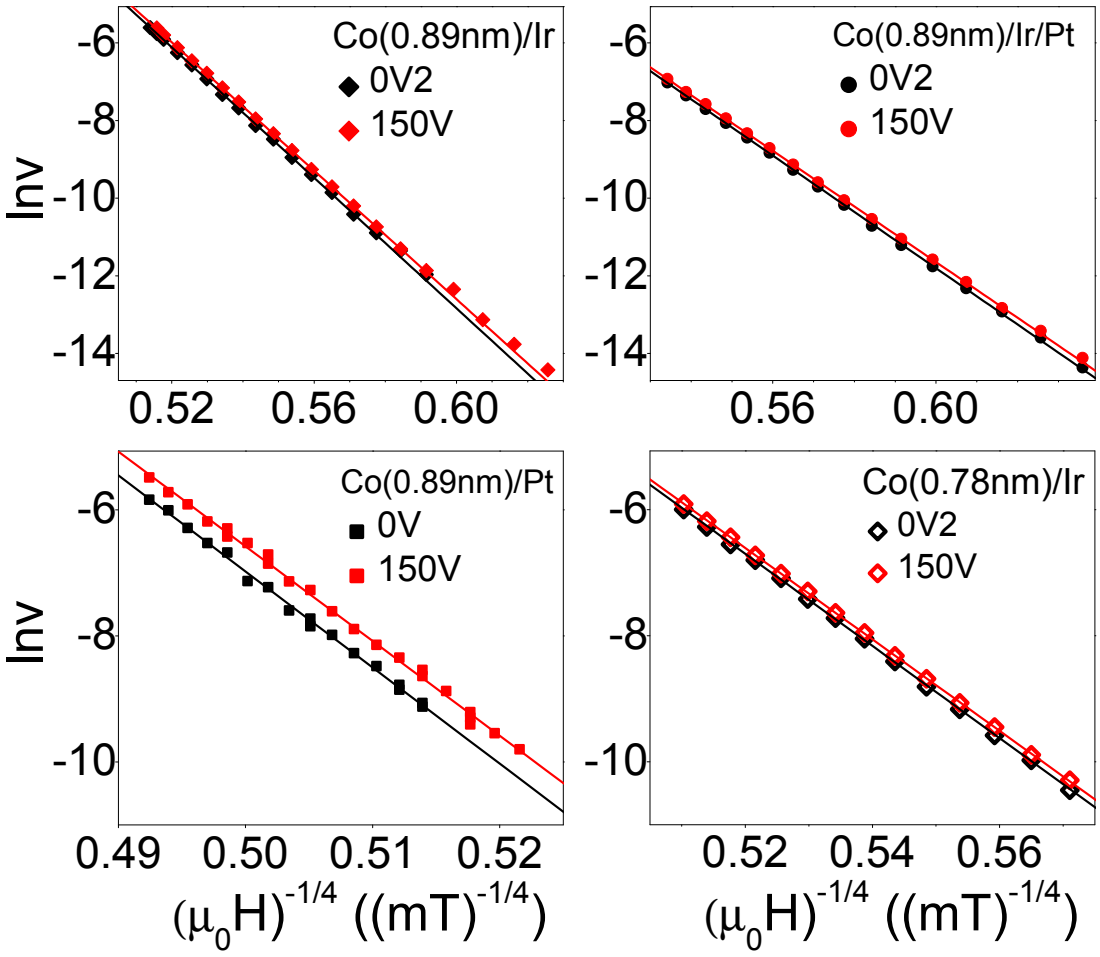


**Figure 6.7:** The natural logarithm of v plotted against $\mu_o H^{-1/4}$ (out-of-plane field) for unstrained films of Pt/Co/X (black shapes) and Pt/Co/X films under tensile out-of-plane strain induced by applying 150 $V$ to the biaxial transducers (red shapes). The Co thicknesses and the capping layers are given in the legends. The lines are least squares fits of the data to the creep law (Equation 2.20).

A short magnetic field pulse is used to nucleate a reverse domain, which occurs repeatably at the same few nucleation sites, and for patterned films can be either in the Hall bar or in a small region of sheet film. Nucleation occurs at a few sites and the domains expand so that an approximately straight domain wall moves into the field of view of the microscope [8]. An image is recorded, then another magnetic field pulse is applied to move the domain wall. Another image is recorded and the difference between the two images is

used to extract the distance the domain wall travels. This is divided by the length of the magnetic field pulse and the resulting velocity can be plotted against driving field. The uncertainties in the velocity values are derived from the standard errors in repeat readings of the distance the domain wall moves or the uncertainty due to the resolution of the image where that is larger. The lengths of the field pulses, defined at the full-width-half-maximum, were between 200 $ms$ and 20 $s$. The rise time was estimated by measuring the domain wall velocity for a range of pulse lengths from 1 $s$ to 20 $ms$. When the pulse length approaches the rise time, the time over which the magnetic field ramps up to the maximum applied value becomes significant, so that the distance moved by the domain wall during the rising and falling edges of the applied field pulse contributes to a difference in the measured velocity compared to values measured with longer pulse lengths. Increases in velocity values, above the uncertainties in the measurement, gave 100 $ms$ as the estimated rise time.

### 6.3.1 Domain wall creep motion in Pt/Co

The field driven domain wall creep velocity was measured in Pt/Co on biaxial transducers. Figures 6.6 and 6.8a show that the domain walls travel faster for a given field when 150 $V$ is applied to the transducer. Plotting the natural logarithm against $\mu_0 H^{-1/4}$ in Figures 6.7 and 6.8b shows that the data are linear, confirming that the motion is in the creep regime for all the Pt/Co Hall bars and sheet films studied. The data in Figures 6.7 and 6.8b were fitted to the creep law (Equation 2.20) with a least squares method.

#### Domain wall creep parameters under strain

The creep parameters can be extracted from fits to the creep law. The intercept of the fit with the vertical axis is $\ln v_o$ and the gradient of the line is the product $\mu_0 H_{dep}^{1/4} U_c / kT$. Figures 6.9 and 6.11a show how $\ln v_o$ changes with transducer voltage for the sheet films capped with Ir, Ir/Pt or Pt, and for the Pt/Co(1.0nm)/Pt Hall bar, respectively. Figures 6.10 and 6.11b show how the creep gradient changes with transducer voltage for the sheet films capped with Ir, Ir/Pt or Pt, and for the Pt/Co(1.0nm)/Pt Hall bar. Figure 6.12 shows the creep intercept $\ln v_o$ and gradient for the Pt/Co/Pt Hall bars against Co thickness for 0 $V$ and 150 $V$. The magnitudes of the intercept and gradient do not show a clear trend with Co thickness but there is a significant difference between the samples capped with Ir or Ir/Pt and those capped only with Pt. The intercepts and gradients of the Pt capped samples are approximately double that of those capped with Ir. This suggests that the

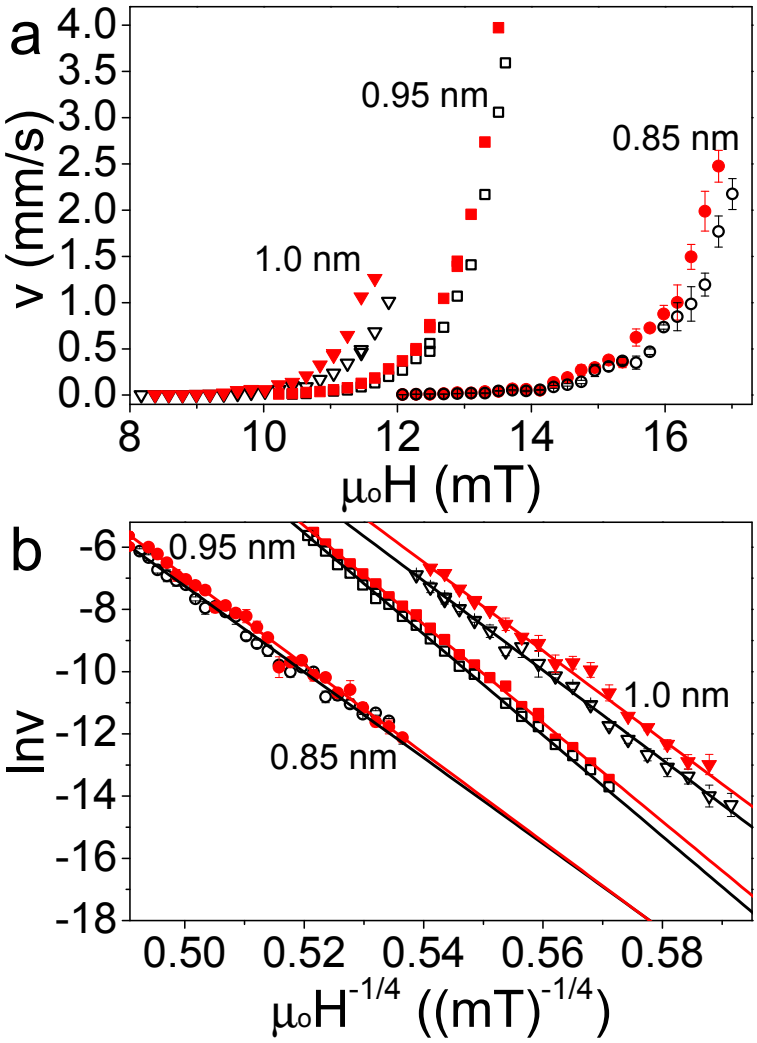


**Figure 6.8:** a) Domain wall velocity v plotted against out-of-plane applied field $\mu_o H$ and b) natural logarithm of v plotted against $\mu_o H^{-1/4}$. Both plots show data for unstrained Pt/Co(t)/Pt (black open shapes) and Pt/Co(t)/Pt under tensile out-of-plane strain induced by applying 150 $V$ to the biaxial transducers (red solid shapes), for t = 0.85 (circles), 0.95 (squares) and 1.0 $nm$ (triangles). The lines in b are least squares fits of the data to the creep law (Equation 2.20).

samples capped with Ir are more magnetically smooth than the films with Pt directly on top of the Co layer. This difference in pinning can also be seen in the Kerr microscope images. Generally the domain walls appear smoother for films with higher anisotropy and for films capped with Ir. Films with lower anisotropy tend to have increased wall roughness, with most domains having cauliflower-like edges, such as in Figure 5.1, and some of the Pt

capped films having domains with ragged, sometimes almost dendritic edges. The creep parameters are not strongly affected by strain: there is no measurable systematic change in these parameters with biaxial transducer voltage.

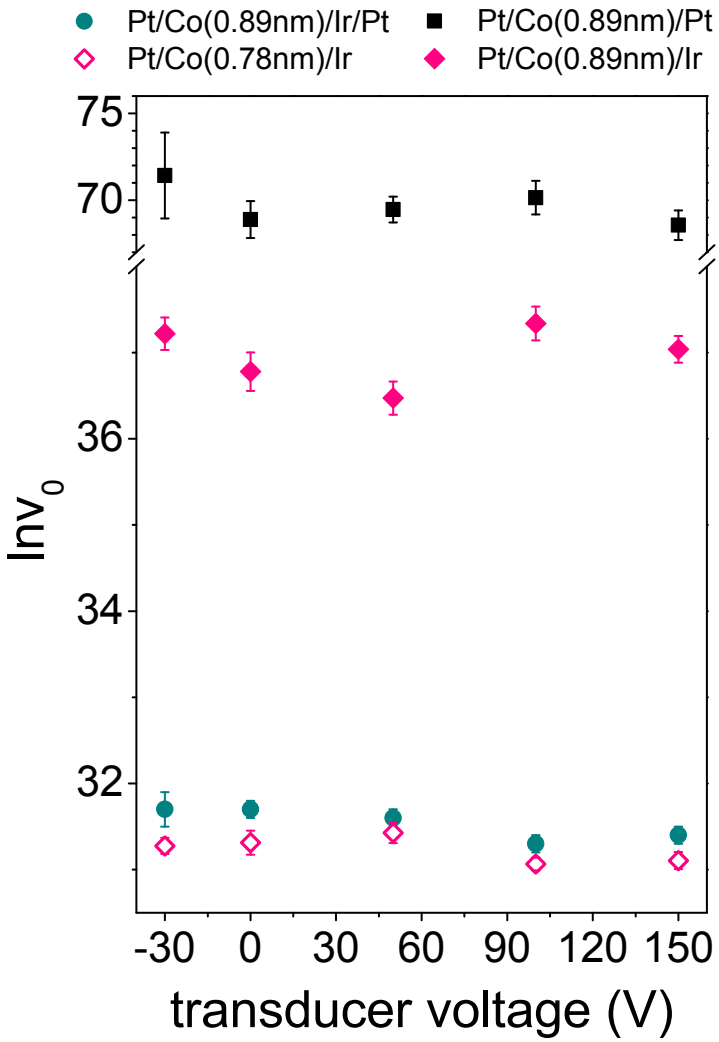


**Figure 6.9:** The creep parameter $\ln v_0$ derived from fits to the creep law (Equation 2.20) of data shown in Figure 6.7 is plotted against applied transducer voltage for Pt/Co(t)/X on biaxial transducers. The Co thicknesses and the capping layers of each of the films are given in the legend.

### Domain wall pinning under strain

Since we do not have a direct measure of $\mu_0 H_{dep}$, the pinning energy ratio $U_c/kT$ is extracted by assuming that $H_{dep} = H_c$ (measured by MOKE for the Hall bar samples only). This assumption accommodates a change with strain of $H_{dep}$ (proportional to the change in $H_c$), although a comparison of the values of $\mu_0 H_c$ (Figure 6.5) to the range of applied fields driving domain wall velocity (Figure 6.8a) shows this estimate of $H_{dep}$ to be too low; $\mu_0 H_c$ is within the range of fields that drive creep motion. The estimate of $H_{dep}$ produces an increased $U_c/kT$, but allows for a shift in $H_{dep}$ under strain equal to the shift in $H_c$. Figures 6.11 and 6.12 show the values of $U_c/kT$ for the Pt/Co/Pt Hall bars. At 0 $V$ it is found to be 69 $\pm$ 2 for 0.85 $nm$, 87 $\pm$ 2 for 0.95 $nm$ and 87 $\pm$ 1 for 1.0 $nm$. As these values are artificially inflated by the estimate of $H_{dep}$, they are somewhat larger than values found in similar polycrystalline Pt/Co/Pt films [22], and in epitaxial Pt/Co/Pt films [31].

There is very little variation in the pinning energy between 0 $V$ and 150 $V$ in any of the three Hall bar Co thicknesses. Figure 6.12 shows the pinning energy ratio $U_c/kT$ as a function of Co thickness in the strained and unstrained Pt/Co/Pt. It is difficult to completely exclude a change in the pinning energy or $\ln v_0$ as a function of strain because the velocity change data is taken over limited magnetic field ranges. However, given the size of the uncertainties and the variation in the gradient and intercept, in order to be unresolved by the measurements any change would have to be limited to just a few percent of the 0 $V$ value, which is much lower than the changes in domain wall velocity shown in the next section.

Although there is no measurable effect on the domain wall creep parameters, Figures 6.6 and 6.8a show a distinct increase in the domain wall velocity under strain from biaxial transducers. The creep parameters are related to the microstructure of the magnetic thin films, so any changes in that structure when the film is strained must be small in comparison to the overall change in the magnetic anisotropy energy. The gradient of the $\ln v$ creep slope is related to the height of the pinning energy barriers that the wall encounters as it moves through the film. The insensitivity to strain of the pinning in Pt/Co with PMA contrasts with studies of ferromagnetic/piezoelectric heterostructures with in-plane magnetic anisotropy where the pinning of domain walls was found to be important in controlling magnetisation reversal via strain [39; 82]. Changes in pinning have also been found in multilayers where the PMA is controlled by direct application of voltages across a stack

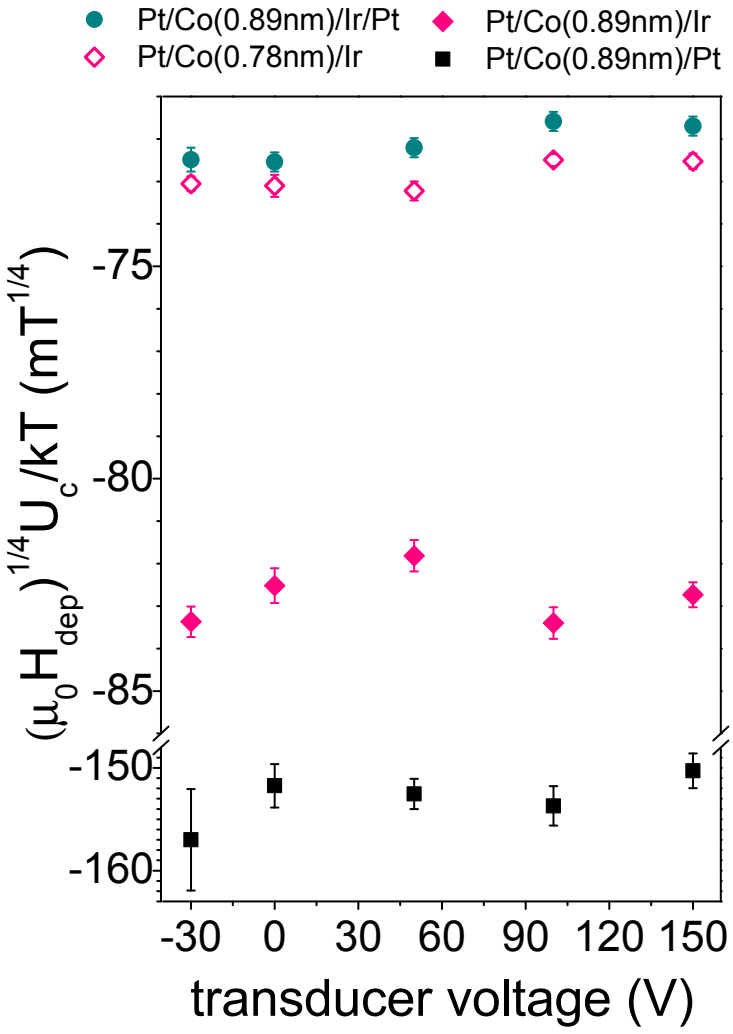


**Figure 6.10:** The creep parameter $\mu_0 H_{dep}^{1/4} U_c/kT$ derived from fits to the creep law (Equation 2.20) of data shown in Figure 6.7 is plotted against applied transducer voltage for Pt/Co(t)/X on biaxial transducers. The Co thicknesses and the capping layers of each of the films are given in the legend.

containing a ferromagnet/oxide interface such as Pt/Co/AlOx [86; 87]. This mechanism for modifying PMA involves charging at the Co/oxide interface, rather than accessing the properties of bulk-like Co atoms, as found here for strained Pt/Co/Pt.

If the domain wall pinning is not affected significantly in Pt/Co thin films on biaxial tansducers, it suggests that the roughness of the magnetic anisotropy energy landscape is

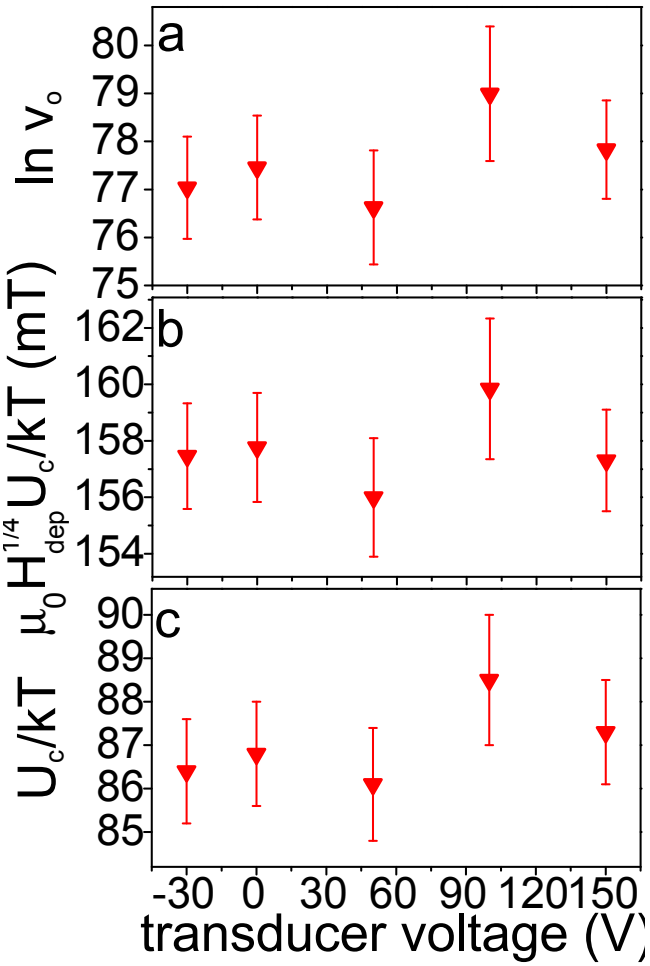


**Figure 6.11:** Parameters derived from fits to the creep law (Equation 2.20) of the creep data at a range of transducer voltages are plotted against transducer voltage for Pt/Co(1.0nm)/Pt on biaxial transducers. The plots show a) the intercept $\ln v_o$, b) the gradient $\mu_0 H_{dep}^{1/4} U_c/kT$ and c) the ratio of the pinning energy to the thermal energy $U_c/kT$.

not strongly influenced by strain, rather the height of the energy landscape is reduced as a whole when tensile out-of-plane strain is the applied to the Pt/Co thin films. The next section explores the effect of this change on the domain wall velocity.

### 6.3.2 Changes in domain wall velocity under strain

The domain wall velocity of Pt/Co thin films increases when positive voltage is applied to the transducers to given tensile out-of-plane strain. Figure 6.13 shows the change in

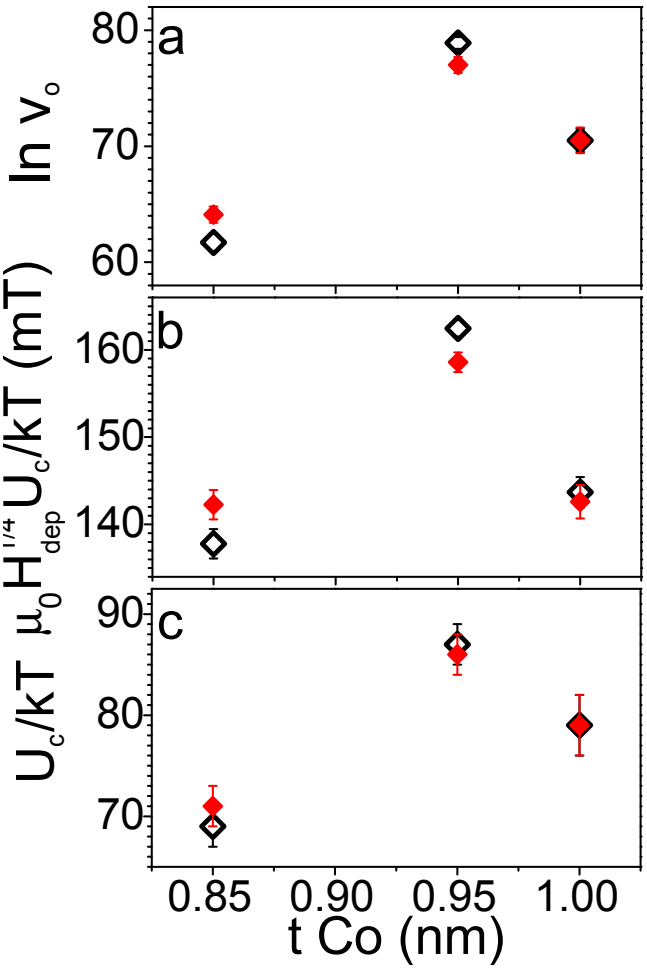


**Figure 6.12:** Parameters derived from fits to the creep law (Equation 2.20) of data shown in Figure 6.8 are plotted against Co thickness t for Pt/Co(t)/Pt on biaxial transducers at 0 $V$ (black, open diamonds) and 150 $V$ (red diamonds). The plots show a) the intercept $lnv_o$, b) the gradient $\mu_0 H_{dep}^{1/4} U_c/kT$ and c) the ratio of the pinning energy to the thermal energy $U_c/kT$.

domain wall velocity from 0 $V$ when -30 $V$, 50 $V$, 100 $V$ and 150V are applied to Pt/Co/X thin films where X is Ir, Ir/Pt or Pt. Figure 6.14 shows the velocity changes under strain from applying 150 $V$ to the biaxial transducers of the Pt/Co(t)/Pt Hall bars (t = 0.85, 0.95, 1.0 $nm$). All films show some variation within the velocity change at a given voltage, but the velocity change is otherwise constant with applied out-of-plane field. The values for the mean velocity changes across the applied field ranges are shown in Figure 6.15 for the Pt/Co/X sheet films and Figures 6.14 b and c for the Pt/Co/Pt Hall bars. When the applied transducer voltage is negative, the velocity tends to reduce, and when the

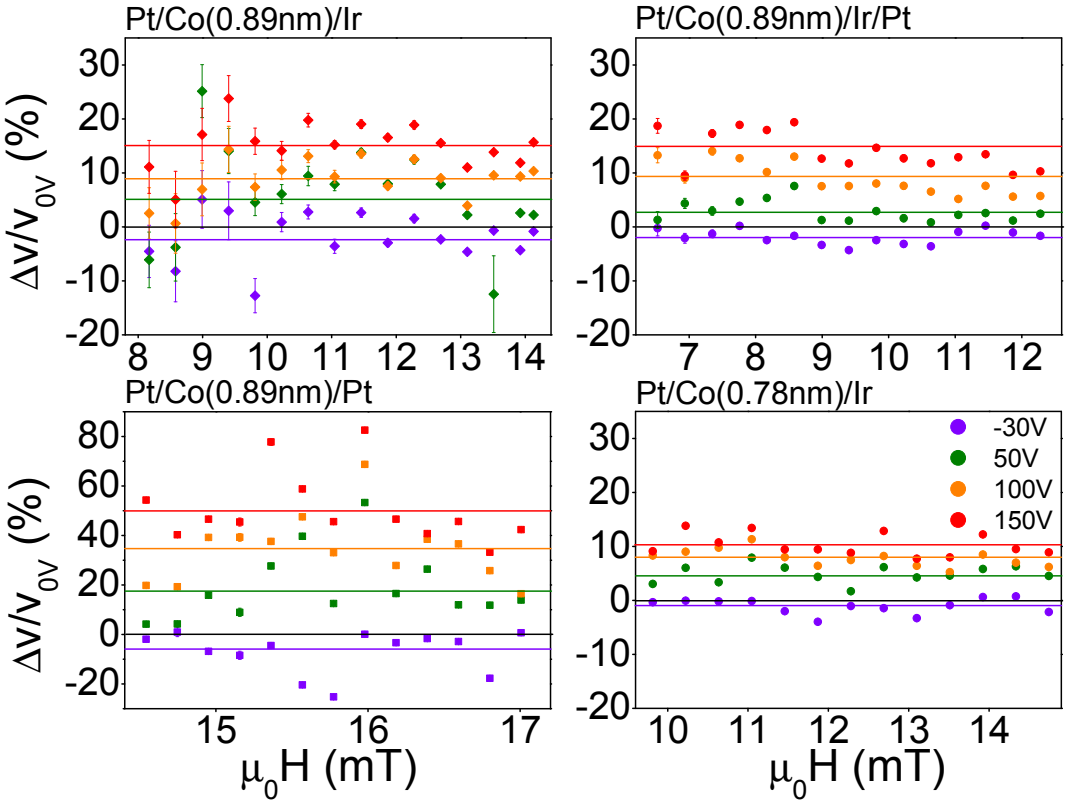


**Figure 6.13:** The percentage change between 0V and -30 $V$, 50 $V$, 100 $V$, 150V of the creep velocity of domain walls in Pt/Co(t)/X on biaxial transducers is plotted against applied out-of-plane magnetic field. The points are the data and the solid, coloured lines are guides to the eye at the mean velocity changes. The plots are labelled with the Co thicknesses and the capping layers.

applied transducer voltage is positive the velocity tends to increase, matching the sign of the changes in magnetic anisotropy due to strain in Pt/Co/Pt. Plotting the velocity change against transducer voltage for the sheet films and the Pt/Co(1.0nm)/Pt Hall bar shows that the creep velocity changes linearly with transducer voltage and tensile out-of-plane strain.

There is generally an increase in the maximum change in velocity with Co thickness, correlated with larger percentage changes in velocity for films with lower initial $K_{eff}$ at 0 $V$. The films capped with Ir or Ir/Pt have the lowest velocity changes at between 10 and 20 %, while the largest increases are in the Pt/Co(0.89nm)/Pt sheet film (50 %) and the Pt/Co(1.0nm)/Pt Hall bar (90 %).

These results can be compared to changes in creep velocity due to direct voltage application across Pt/Co/GdOx, where the mechanism for modifying PMA is related to charging

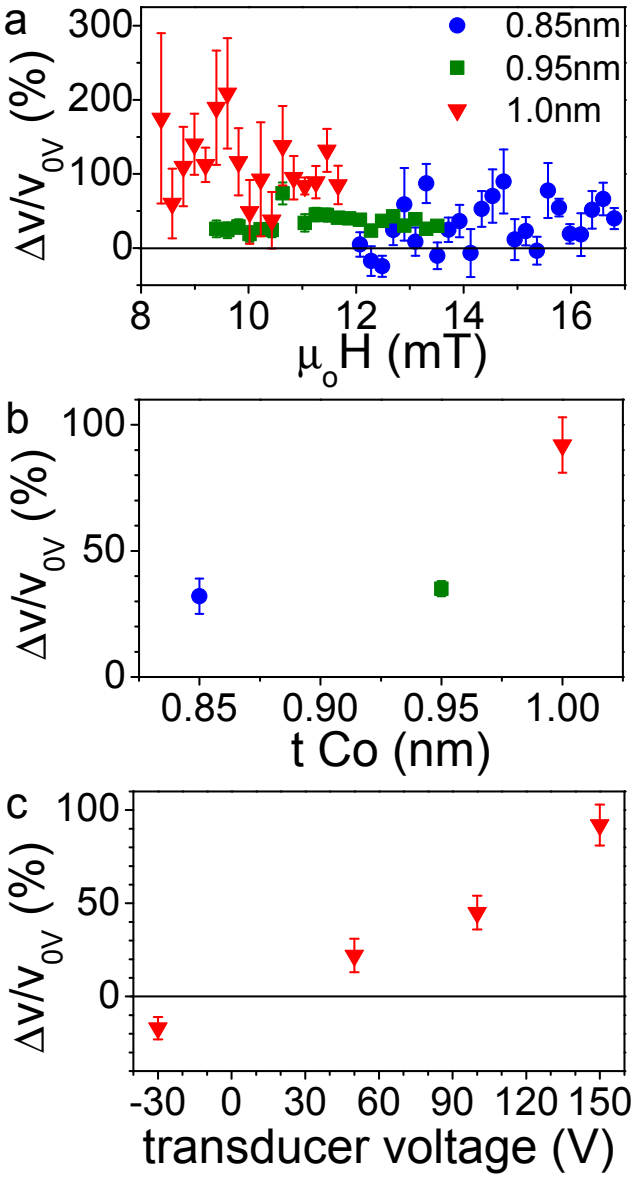


**Figure 6.14:** a) The percentage change between 0V and 150V of the creep velocity of domain walls in Pt/Co(t)/Pt (t is given in the legend) on biaxial transducers is plotted against applied magnetic field. b) The mean (across the applied field range) of the percentage change in velocity plotted against Co thickness t. c) The mean percentage change in the domain wall velocity in Pt/Co(1.0nm)/Pt is plotted against transducer voltage. The error bars are the standard errors on the mean values.

at the Co/oxide interface. The change in velocity was of comparable size to changes in

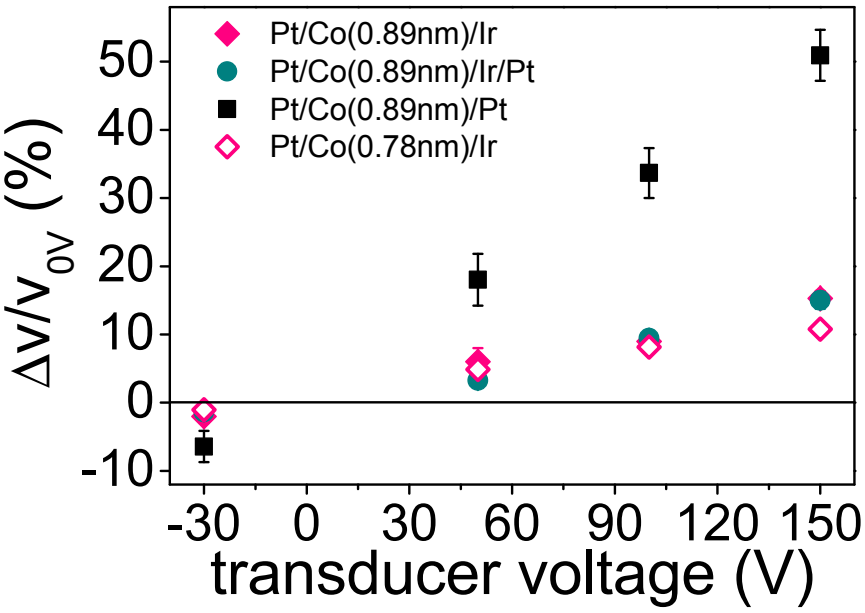


**Figure 6.15:** The mean percentage change (taken over the range of applied fields) from 0 $V$ of the creep velocity of domain walls in Pt/Co(t)/X on biaxial transducers is plotted against applied transducer voltage. The Co thicknesses and the capping layers of the films are given in the legend and the error bars are the standard errors on the mean values.

Pt/Co under strain, but was not constant with applied field, dropping from ∼35 % at low driving fields and low velocities to ∼15 % at high driving fields and high velocities [88]. Other systems based on voltage gating and interface charging of Co based multilayers have reported doubling of domain wall velocity [89], decreases of 10 times the ungated velocity [87] and changes in velocity of up to an order of magnitude [86]. The velocity changes in Pt/Co under strain are small compared to the changes from interface charging. However, the maximum strain from the piezoelectric transducers is small at ∼0.1 %, so it might be possible to further increase the velocity changes if a higher strain could be produced.

The domain wall velocity change shows some correlation with both $K_{eff}$ at 0 $V$ and $|\mu_0 H_{DMI}|$, with higher velocity changes when both parameters are low. Figure 6.16 shows the velocity changes at 150 $V$ plotted against the initial (0 $V$) $K_{eff}$ and the absolute value of the DMI field. As discussed in Chapter 5, $K_{eff}$ and $\mu_0 H_{DMI}$ show some weak correlation, since they are both derived from spin-orbit coupling at the Co/heavy metal interfaces. There are differences in how the velocity change depends on $K_{eff}$ and $|\mu_0 H_{DMI}|$, which suggests that both parameters have an effect on how the domain wall velocity behaves under strain.

To understand this further, the domain wall energy and structure, which depend on both $K_{eff}$ and $\mu_0 H_{DMI}$ will be discussed.

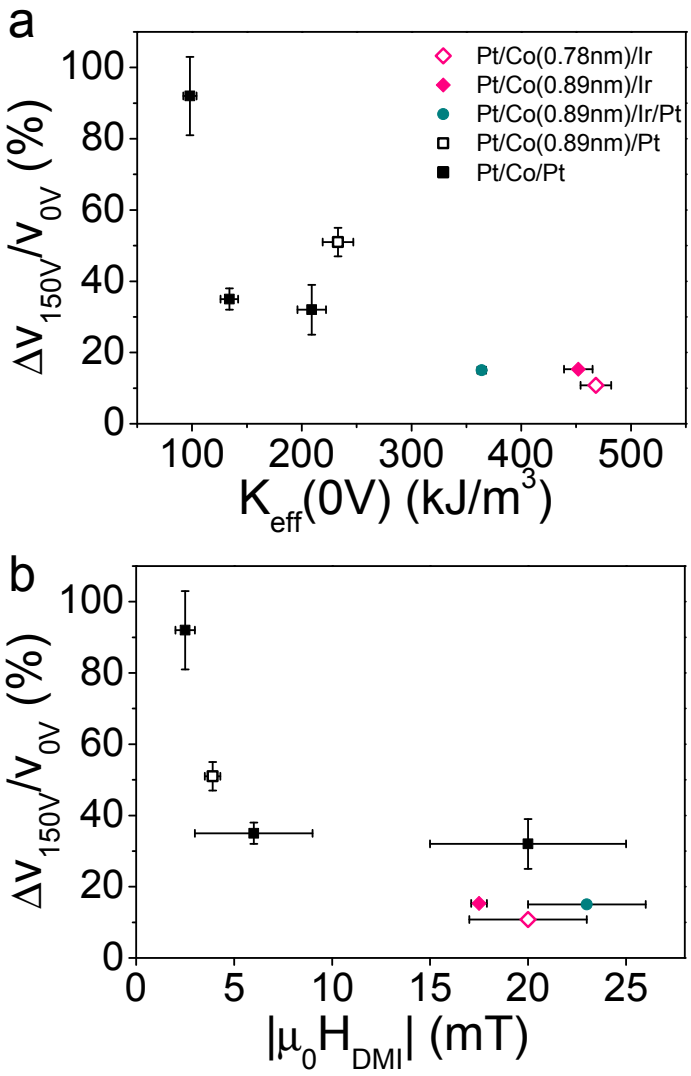


**Figure 6.16:** The percentage change of domain wall velocity in Pt/Co(t)/X between 0 $V$ and 150 $V$ applied to the biaxial transducers is plotted against a) the effective magnetic anisotropy at 0 $V$ and b) the absolute value of the DMI field. The film structures for both plots are given in the legend of a and the $\Delta v/v_{0V}$ error bars are the standard errors on the mean values.

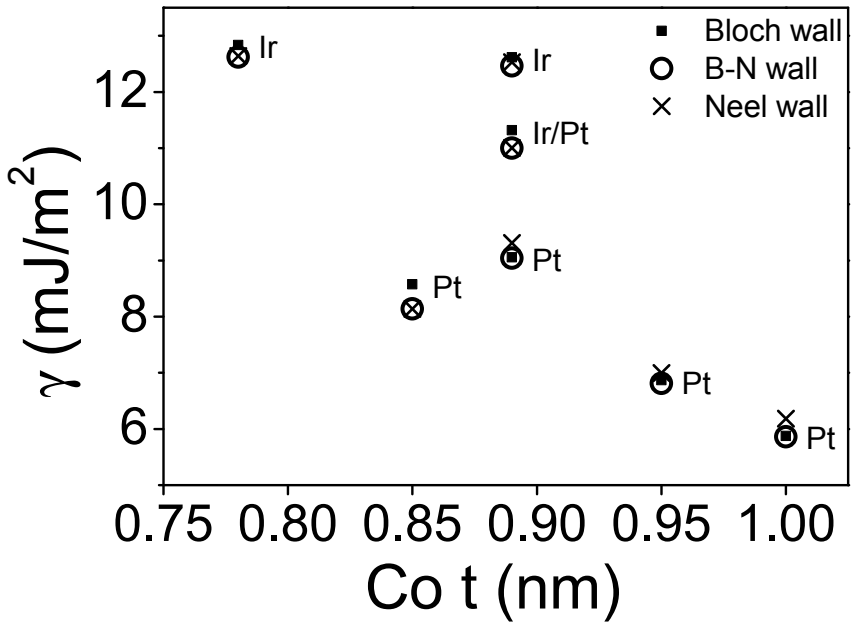


**Figure 6.17:** The energies of domain walls in Pt/Co(t)/X thin films (t = 0.78, 0.89 $nm$) and Pt/Co(t)/Pt Hall bars (t = 0.85, 0.95, 1.0 $nm$) are plotted against Co thickness t. For comparison, the energy has been calculated for walls that are fully Bloch, fully Néel or a combination (B-N), although the lowest energy wall type is favoured in each sample. The data points are labelled with the capping layers.

### 6.3.3 Domain wall structure and energy

The modification of PMA under tensile out-of-plane strain affects the domain wall velocity through changes to the structure and energy of the domain wall. As the tensile strain increases and the PMA is reduced, the domain wall width increases and the domain wall energy decreases. Therefore, reduced PMA lowers the energy barrier to elements of the film reversing as the domain wall moves, so for lower $K_{eff}$ there is a lower nucleation field and a higher domain wall velocity for a given out-of-plane magnetic field. The lower the initial PMA at 0 $V$, the larger the percentage change in domain wall velocity, which explains the general trend of larger velocity changes for thicker films, but is not sufficient to fully account for some of the variation seen between samples.

The structure and energy of a domain wall are influenced by the DMI as well as the PMA. In Chapter 5 it was shown that most of the thin films studied in this work are not pure Bloch walls, and have some Néel-like component. Figure 6.17 shows the energies of Bloch, Bloch-Néel and Néel domain walls for each of the thin films. In order to minimise the

energy of the system, the lowest energy wall type is favoured. Only the Pt/Co(0.89nm)/Pt sheet film and the Pt/Co(1.0nm)/Pt Hall bar have calculated wall energies where Bloch is the lowest energy wall type, while for all others Bloch-Néel is favoured (or Néel for the Pt/Co(0.85nm)/Pt Hall bar). Figure 6.18 shows that the percentage change in domain wall velocity at 150 $V$ is linear with the domain wall energy, and with the change in domain wall energy, for all Pt/Co films where Bloch-Néel or Néel wall types are favoured. The Pt/Co(0.89nm)/Pt sheet film and the Pt/Co(1.0nm)/Pt Hall bar have domain wall velocity changes that are considerably higher, at 50 % and 90 % change respectively, showing that the velocity of fully Bloch domain walls is more sensitive to strain-induced changes in the PMA than that of other wall structures.

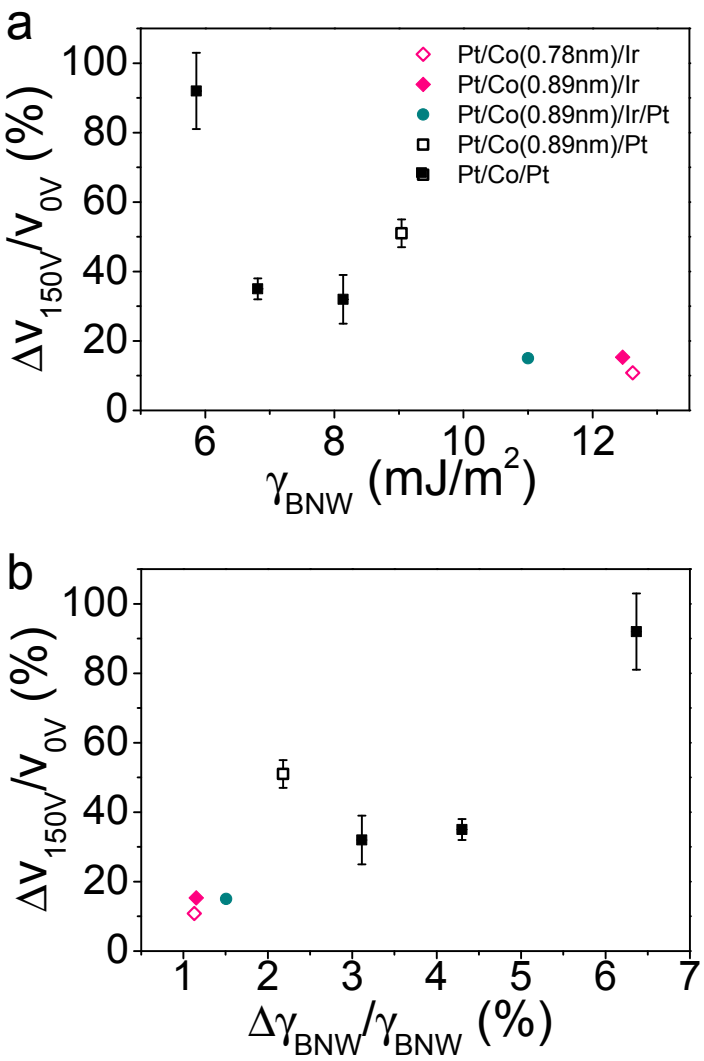


**Figure 6.18:** The percentage change of domain wall velocity in Pt/Co(t)/X between 0 $V$ and 150 $V$ applied to the biaxial transducers is plotted against a) the calculated domain wall energy at 0 $V$ and b) the estimated change in the domain wall energy between 0 $V$ and 150 $V$. The film structures for both plots are given in the legend of a.

## 6.4 Summary

In summary, lowering the PMA with strain from biaxial tranducers reduces the coercivity of out-of-plane hysteresis loops and increases the domain wall creep velocity of the Pt/Co thin films by between 10 % and 90 % in the range of fields applied. Plotting the domain wall velocity curves as $\ln v$ versus $\mu_0 H_{dep}^{-1/4}$ shows that the domain wall motion is in the creep regime for all measurements. Fitting the creep law to the data showed no measurable changes in the creep parameters ($\ln v_0$ and the pinning energy), which limits any changes caused by strain to below a few percent of the unstrained values. This shows that although the magnetic anisotropy energy landscape of a Pt/Co film is lowered by strain, it is not distorted significantly.

The proportional size of the change in domain wall velocity with strain depends on the domain wall structure and energy. Pt/Co films with lower PMA at 0 $V$ generally have lower domain wall energy and show a higher percentage change in domain wall velocity under strain. Within the set of films with a DMI field large enough to give the domain walls some Néel-like component, the domain wall velocity change is linear with domain wall energy and with domain wall energy change under strain. The films with the lowest DMI, which favours pure Bloch walls, have higher domain wall velocity changes with strain, with the velocity in Pt/Co(1.0nm)Pt almost doubling under strain from the biaxial transducer.

# Chapter 7

Conclusions

The effect of piezoelectric strain on the magnetic properties of thin films of Pt/Co has been explored. The context of the work and the theoretical concepts behind it have been explained and the relevant experimental methods have been described. The results of experiments investigating the magnetic anisotropy, DMI and magnetisation reversal of strained and unstrained Pt/Co thin films have been presented.

Thin films of Pt/Co can have in-plane or out-of-plane magnetic anisotropy depending on the balance of in-plane bulk magnetocrystalline anisotropy and the surface magnetocrystalline anisotropy, which is derived from spin-orbit coupling at the Co interfaces. Co is a magnetostrictive ferromagnet which can be strained to induce changes in its magnetic anisotropy. Pt/Co/Pt thin films were found to have PMA below a Co thickness threshold of 1.1 $nm$. The PMA of Pt/Co thin films increases as the Co thickness decreases. Out-of-plane strain of 9 $\times 10^{-4}$ from biaxial piezoelectric transducers modified the PMA of Pt/Co/Pt thin films by 10 $kJ/m^3$. The magnetostriction constant of Pt/Co/Pt was found to be -3.5$\times 10^{-5}$, and did not vary between films with different Co thicknesses, indicating that the anisotropy change was due to the bulk-like Co atoms. Out-of-plane hysteresis loops of Pt/Co/Pt on biaxial transducers were fully remanent at zero applied field for Co thicknesses below 1.1 $nm$. The coercive field increases as Co thickness decreases and the change in coercive field with applied biaxial strain is larger for films with thicker Co. Uniaxial transducers were used to give an in-plane strain in Pt/Co/Pt thin films, which causes a small modification to the PMA and induces an in-plane anisotropy.

The DMI was measured from domain wall creep velocity versus in-plane bias field curves in Pt/Co thin films capped with Ir, Ir/Pt or Pt. Films capped with Ir or Ir/Pt were found to have positive DMI fields and films capped with Pt only were found to have negative DMI fields. From the perpendicular anisotropy constants and DMI fields, the domain wall energies could be calculated and the wall structures could be determined. The films capped with Ir or Ir/Pt did not have DMI fields of sufficient magnitude to overcome the domain wall shape anisotropy and become fully Néel, so take an intermediate form with some Bloch and some left handed Néel component. Of the films capped only with Pt, one film has domain walls of an intermediate form with some Bloch and some right handed Néel component, one has a DMI field just above the threshold necessary for fully Néel walls to form and two films have DMI fields low enough that the domain wall energy favours a Bloch structure.

Domain wall creep motion was studied in Pt/Co thin films capped with Ir, Ir/Pt or Pt on biaxial transducers. The domain wall creep velocity of the Pt/Co thin films changed by

between 10 % and 90 % when 150 $V$ was applied to the transducers to give an out-of-plane tensile strain of 9 $\times 10^{-4}$. The domain wall motion was found to be in the creep regime for all of the measurements. The creep parameters ($\ln v_0$ and the pinning energy) were not found to change significantly when voltage was applied to the transducer, showing that the magnetic anisotropy energy landscape of the a Pt/Co film is lowered, but not distorted by the tensile out-of-plane strain.

The change in domain wall velocity under strain varied linearly with domain wall energy at 0 $V$, and with the domain wall energy change, for Pt/Co films with DMI fields large enough to give the domain walls some Néel-like component. For these films the change in domain wall velocity was below 40 %. Two of the Pt/Co/Pt films did not fit the same trend with domain wall energy and had much higher domain wall velocity change under strain (50 % and 90 %). These films had DMI fields low enough that the domain wall energy favoured a Bloch structure.

Domain wall creep velocity in Pt/Co thin films with PMA can be modified with strain by an amount related to the proportional change in the energy of the domain wall. The energy of a Bloch domain wall depends only on the magnetic anisotropy constant and the exchange stiffness, while the energy of walls with some Néel component also depends on the DMI field. Strain modifies the PMA of the Pt/Co but doesn't affect the DMI, therefore the velocity of Bloch walls is more sensitive to strain than Néel walls.

To continue the work of this project, one could extend the investigation of the effect of strain on field driven domain wall motion beyond the creep regime, or investigate the effect of strain on current driven domain wall motion. The effect of strain from uniaxial transducers on the DMI field as the in-plane anisotropy is modified could be studied.

Strain from piezoeletric transducers is a convenient way of using strain to tune the parameters of Pt/Co thin films. Multiferroic heterostructures that combine piezoelectric materials with PMA thin films have potential as devices for technological applications as well for studying the physics associated with magnetisation dynamics and magnetic domain walls.

# References


[1] D. Adams, *The Hitchhiker's Guide to the Galaxy*. London: Pan Macmillan, 1992. i

[2] C. Chappert, A. Fert, and F. N. Van Dau, "The emergence of spin electronics in data storage.," *Nature materials*, vol. 6, pp. 813–23, Nov. 2007. 2

[3] S. Parkin, M. Hayashi, and L. Thomas, "Magnetic domain-wall racetrack memory.," *Science*, vol. 320, pp. 190–194, 2008. 2, 5

[4] S.-W. Jung, W. Kim, T.-D. Lee, K.-J. Lee, and H.-W. Lee, "Current-induced domain wall motion in a nanowire with perpendicular magnetic anisotropy," *Applied Physics Letters*, vol. 92, no. 20, p. 202508, 2008. 2

[5] O. Boulle, G. Malinowski, and M. Kläui, "Current-induced domain wall motion in nanoscale ferromagnetic elements," *Materials Science and Engineering R*, vol. 72, pp. 159–187, 2011. 2, 3

[6] K. L. Wang, J. G. Alzate, and P. Khalili Amiri, "Low-power non-volatile spintronic memory: STT-RAM and beyond," *Journal of Physics D: Applied Physics*, vol. 46, no. 7, p. 074003, 2013. 2

[7] P. Chauve, T. Giamarchi, and P. Le Doussal, "Creep and depinning in disordered media," *Physical Review B*, vol. 62, no. 10, pp. 6241–6267, 2000. 3, 16, 17, 18

[8] S. Lemerle, J. Ferré, C. Chappert, V. Mathet, T. Giamarchi, and P. Le Doussal, "Domain Wall Creep in an Ising Ultrathin Magnetic Film," *Physical Review Letters*, vol. 80, no. 4, pp. 849–852, 1998. 3, 16, 17, 91

[9] J. Gorchon, S. Bustingorry, J. Ferré, V. Jeudy, a. B. Kolton, and T. Giamarchi, "Pinning-dependent field-driven domain wall dynamics and thermal scaling in an ul-

trathin Pt/Co/Pt magnetic film," *Physical Review Letters*, vol. 113, no. 2, p. 027205, 2014. 3, 16, 17, 18

[10] I. Dzyaloshinsky, "A thermodynamic theory of "weak" ferromagnetism of antiferromagnetics," *Journal of Physics and Chemistry of Solids*, vol. 4, pp. 241–255, 1958. 3, 15

[11] T. Moriya, "Anisotropic superexchange interaction and weak ferromagnetism," *Physical Review*, vol. 120, no. 1, pp. 91–98, 1960. 3, 15

[12] M. Heide, G. Bihlmayer, and S. Blügel, "Dzyaloshinskii-Moriya interaction accounting for the orientation of magnetic domains in ultrathin films: Fe/W(110)," *Physical Review B - Condensed Matter and Materials Physics*, vol. 78, no. 14, p. 140403(R), 2008. 3, 15, 16

[13] A. Thiaville, S. Rohart, E. Jué, V. Cros, and A. Fert, "Dynamics of Dzyaloshinskii domain walls in ultrathin magnetic films," *EPL (Europhysics Letters)*, vol. 100, no. 5, p. 57002, 2012. 13, 15, 16

[14] G. Chen, T. Ma, A. T. N'Diaye, H. Kwon, C. Won, Y. Wu, and A. K. Schmid, "Tailoring the chirality of magnetic domain walls by interface engineering," *Nature Communications*, vol. 4, p. 2671, 2013. 15, 16

[15] S.-G. Je, D.-H. Kim, S.-C. Yoo, B.-C. Min, K.-J. Lee, and S.-B. Choe, "Asymmetric magnetic domain-wall motion by the Dzyaloshinskii-Moriya interaction," *Physical Review B*, vol. 88, no. 21, p. 214401, 2013. 16, 58, 75

[16] A. Hrabec, N. A. Porter, A. Wells, M. J. Benitez, G. Burnell, S. McVitie, D. McGrouther, T. A. Moore, and C. H. Marrows, "Measuring and tailoring the Dzyaloshinskii-Moriya interaction in perpendicularly magnetized thin films," *Physical Review B*, vol. 90, p. 020402(R), 2014. 3, 4, 16, 58, 77

[17] P. F. Carcia, "Perpendicular magnetic anisotropy in Pd/Co and Pt/Co thin-film layered structures," *Journal of Applied Physics*, vol. 63, no. 10, p. 5066, 1988. 3, 10

[18] S. Hashimoto, Y. Ochiai, and K. Aso, "Perpendicular magnetic anisotropy and magnetostriction of sputtered Co/Pd and Co/Pt multilayered films," *Journal of Applied Physics*, vol. 66, no. 10, pp. 4909–4916, 1989. 3, 10, 49, 50

[19] N. Nakajima, T. Koide, T. Shidara, H. Miyauchi, H. Fukutani, A. Fujimori, K. Iio, T. Katayama, M. Nývlt, and Y. Suzuki, "Perpendicular magnetic anisotropy caused by interfacial hybridization via enhanced orbital moment in Co/Pt multilayers: magnetic circular x-ray dichroism study," *Physical Review Letters*, vol. 81, no. 23, pp. 5229–5232, 1998. 3, 10, 11, 21, 50

[20] S. Bandiera, R. C. Sousa, B. Rodmacq, and B. Dieny, "Enhancement of perpendicular magnetic anisotropy through reduction of Co-Pt interdiffusion in (Co/Pt) multilayers," *Applied Physics Letters*, vol. 100, no. 14, p. 142410, 2012. 3, 4

[21] K. Kyuno, J.-G. Ha, R. Yamamoto, and S. Asano, "Theoretical study on the strain dependence of the magnetic anisotropy of X/Co(X=Pt, Cu, Ag, and Au) metallic multilayers," *Journal of Applied Physics*, vol. 79, no. 9, pp. 7084–7089, 1996. 3, 11

[22] P. J. Metaxas, J. P. Jamet, A. Mougin, M. Cormier, J. Ferre, V. Baltz, B. Rodmacq, B. Dieny, and R. L. Stamps, "Creep and flow regimes of magnetic domain-wall motion in ultrathin Pt/Co/Pt films with perpendicular anisotropy," *Physical Review Letters*, vol. 99, no. 21, p. 217208, 2007. 3, 17, 18, 77, 95

[23] R. Lavrijsen, P. P. J. Haazen, E. Murè€, J. H. Franken, J. T. Kohlhepp, H. J. M. Swagten, and B. Koopmans, "Asymmetric Pt/Co/Pt-stack induced sign-control of current-induced magnetic domain-wall creep," *Applied Physics Letters*, vol. 100, no. 26, p. 262408, 2012. 4

[24] S. Bustingorry, A. B. Kolton, and T. Giamarchi, "Thermal rounding of the depinning transition in ultrathin Pt/Co/Pt films," *Physical Review B - Condensed Matter and Materials Physics*, vol. 85, no. 21, p. 214416, 2012.

[25] K.-W. Moon, D.-H. Kim, S.-C. Yoo, C.-G. Cho, S. Hwang, B. Kahng, B.-C. Min, K.-H. Shin, and S.-B. Choe, "Distinct Universality Classes of Domain Wall Roughness in Two-Dimensional Pt/Co/Pt Films," *Physical Review Letters*, vol. 110, no. 10, p. 107203, 2013. 17

[26] E. E. Ferrero, S. Bustingorry, A. B. Kolton, and A. Rosso, "Numerical approaches on driven elastic interfaces in random media," *Comptes Rendus Physique*, vol. 14, pp. 641–650, 2013. 18

[27] J. Ferré, P. J. Metaxas, A. Mougin, J.-P. Jamet, J. Gorchon, and V. Jeudy, "Universal magnetic domain wall dynamics in the presence of weak disorder," *Comptes Rendus Physique*, vol. 14, no. 8, pp. 651–666, 2013. 3, 17, 18

[28] R. Lavrijsen, D. M. F. Hartmann, A. van den Brink, Y. Yin, B. Barcones, R. a. Duine, M. a. Verheijen, H. J. M. Swagten, and B. Koopmans, "Asymmetric magnetic bubble expansion under in-plane field in Pt/Co/Pt: Effect of interface engineering," *Physical Review B*, vol. 91, no. 10, p. 104414, 2015. 4, 16, 58, 75

[29] M. S. Pierce, J. E. Davies, J. J. Turner, K. Chesnel, E. E. Fullerton, J. Nam, R. Hailstone, S. D. Kevan, J. B. Kortright, K. Liu, L. B. Sorensen, B. R. York, and O. Hellwig, "Influence of structural disorder on magnetic domain formation in perpendicular anisotropy thin films," *Physical Review B*, vol. 87, p. 184428, May 2013. 4

[30] J. H. Kim and S. C. Shin, "Interface roughness effects on the surface anisotropy in Co/Pt multilayer films," *Journal of Applied Physics*, vol. 80, no. 5, pp. 3121–3123, 1996.

[31] A. P. Mihai, A. L. Whiteside, E. J. Canwell, C. H. Marrows, M. J. Benitez, D. McGrouther, S. McVitie, S. McFadzean, and T. A. Moore, "Effect of substrate temperature on the magnetic properties of epitaxial sputter-grown Co/Pt," *Applied Physics Letters*, vol. 103, no. 26, p. 262401, 2013. 4, 18, 95

[32] J. H. Franken, H. J. M. Swagten, and B. Koopmans, "Shift registers based on magnetic domain wall ratchets with perpendicular anisotropy.," *Nature nanotechnology*, vol. 7, pp. 499–503, Aug. 2012. 4, 49

[33] R. Ramesh and N. a. Spaldin, "Multiferroics: progress and prospects in thin films.," *Nature materials*, vol. 6, pp. 21–29, 2007. 4

[34] C. A. F. Vaz, "Electric field control of magnetism in multiferroic heterostructures.," *Journal of Physics: Condensed Matter*, vol. 24, no. 33, p. 333201, 2012. 4

[35] R. Streubel, D. Köhler, R. Schäfer, and L. M. Eng, "Strain-mediated elastic coupling in magnetoelectric nickel/barium-titanate heterostructures," *Physical Review B*, vol. 87, no. 5, p. 054410, 2013. 4

[36] T. H. E. Lahtinen, K. J. A. Franke, and S. van Dijken, "Electric-field control of magnetic domain wall motion and local magnetization reversal.," *Scientific Reports*, vol. 2, p. 258, 2012. 5, 82

[37] T. Brintlinger, S.-H. Lim, K. H. Baloch, P. Alexander, Y. Qi, J. Barry, J. Melngailis, L. Salamanca-Riba, I. Takeuchi, and J. Cumings, "In situ observation of reversible nanomagnetic switching induced by electric fields.," *Nano Letters*, vol. 10, pp. 1219–1223, 2010. 5

[38] D. E. Parkes, L. R. Shelford, P. Wadley, V. Holý, M. Wang, a. T. Hindmarch, G. van der Laan, R. P. Campion, K. W. Edmonds, S. a. Cavill, and a. W. Rushforth, "Magnetostrictive thin films for microwave spintronics.," *Scientific reports*, vol. 3, p. 2220, July 2013. 5

[39] N. Lei, T. Devolder, G. Agnus, P. Aubert, L. Daniel, J.-V. Kim, W. Zhao, T. Trypiniotis, R. P. Cowburn, C. Chappert, D. Ravelosona, and P. Lecoeur, "Strain-controlled magnetic domain wall propagation in hybrid piezoelectric/ferromagnetic structures," *Nature Communications*, vol. 4, p. 1378, 2013. 5, 82, 95

[40] V. Novosad, Y. Otani, A. Ohsawa, S. G. Kim, K. Fukamichi, J. Koike, K. Maruyama, O. Kitakami, and Y. Shimada, "Novel magnetostrictive memory device," *Journal of Applied Physics*, vol. 87, no. 9, pp. 6400–6402, 2000. 5

[41] M. Buzzi, R. V. Chopdekar, J. L. Hockel, A. Bur, T. Wu, N. Pilet, P. Warnicke, G. P. Carman, L. J. Heyderman, and F. Nolting, "Single Domain Spin Manipulation by Electric Fields in Strain Coupled Artificial Multiferroic Nanostructures," *Physical Review Letters*, vol. 111, no. 2, p. 027204, 2013. 5

[42] C. Zhang, T. Ma, and M. Yan, "Induced additional anisotropy influences on magnetostriction of giant magnetostrictive materials," *Journal of Applied Physics*, vol. 112, no. 10, p. 103908, 2012. 5, 82

[43] T. Wu, A. Bur, P. Zhao, K. P. Mohanchandra, K. Wong, K. L. Wang, C. S. Lynch, and G. P. Carman, "Giant electric-field-induced reversible and permanent magnetization reorientation on magnetoelectric Ni/(011) [Pb(Mg1/3Nb2/3)O3](1-x)-[PbTiO3]x heterostructure," *Applied Physics Letters*, vol. 98, no. 1, p. 012504, 2011. 5, 82

[44] J.-H. Kim, K.-S. Ryu, J.-W. Jeong, and S.-C. Shin, "Large converse magnetoelectric coupling effect at room temperature in CoPd/PMN-PT (001) heterostructure," *Applied Physics Letters*, vol. 97, no. 25, p. 252508, 2010. 5, 82, 89

[45] E. De Ranieri, P. E. Roy, D. Fang, E. K. Vehsthedt, A. C. Irvine, D. Heiss, A. Casiraghi, R. P. Campion, B. L. Gallagher, T. Jungwirth, and J. Wunderlich, "Piezoelectric control of the mobility of a domain wall driven by adiabatic and non-adiabatic torques," *Nature Materials*, vol. 12, pp. 808–814, 2013. 5, 82

[46] R. Skomski, *Simple Models of Magnetism*. Oxford: Oxford University Press, 1 ed., 2012. 8, 9, 10, 11, 12, 14

[47] J. Coey, *Magnetism and Magnetic Materials*. Cambridge: Cambridge University Press, 1 ed., 2010. 10, 21

[48] D. Weller, Y. Wu, J. Stöhr, M. Samant, B. D. Hermsmeier, and C. Chappert, "Orbital magnetic moments of Co in multilayers with perpendicular magnetic anisotropy," *Physical Review B*, vol. 49, no. 18, pp. 12888–12896, 1994. 10

[49] D. Weller, J. Stöhr, R. Nakajima, A. Carl, M. G. Samant, C. Chappert, R. Mégy, P. Beauvillain, P. Veillet, and G. A. Held, "Microscopic origin of magnetic anisotropy in Au/Co/Au probed with X-ray magnetic circular dichroism," *Physical Review Letters*, vol. 75, no. 20, pp. 3752–3755, 1995. 10

[50] P. Bruno, "Tight-binding approach to the orbital magnetic moment and magnetocrystalline anisotropy of transition-metal monolayers," *Physical Review B*, vol. 39, pp. 865–868, 1989. 11

[51] M. T. Johnson, P. J. H. Bloemen, F. J. A. den Broeder, and J. J. de Vries, "Magnetic anisotropy in metallic multilayers," *Reports on Progress in Physics*, vol. 59, no. 11, pp. 1409–1458, 1996. 12

[52] G. Chen, A. T. N'Diaye, S. P. Kang, H. Y. Kwon, C. Won, Y. Wu, Z. Q. Qiu, and A. K. Schmid, "Unlocking Bloch-type chirality in ultrathin magnets through uniaxial strain," vol. 6, p. 6598, 2015. 15

[53] S. V. Tarasenko, A. Stankiewicz, V. V. Tarasenko, and J. Ferre, "Bloch wall dynamics in ultrathin ferromagnetic films," *Journal of Magnetism and Magnetic Materials*, vol. 189, pp. 19–24, 1998. 15

[54] M. Bode, M. Heide, K. von Bergmann, P. Ferriani, S. Heinze, G. Bihlmayer, a. Kubetzka, O. Pietzsch, S. Blügel, and R. Wiesendanger, "Chiral magnetic order at surfaces driven by inversion asymmetry.," *Nature*, vol. 447, no. 7141, pp. 190–193, 2007. 15

[55] A. Fert and P. M. Levy, "Role of anisotropic exchange interactions in determining the properties of spin-glasses," *Physical Review Letters*, vol. 44, no. 23, pp. 1538–1541, 1980. 15

[56] K.-S. Ryu, L. Thomas, S.-H. Yang, and S. Parkin, "Chiral spin torque at magnetic domain walls.," *Nature Nanotechnology*, vol. 8, pp. 527–533, 2013. 15

[57] D. Petit, P. R. Seem, M. Tillette, R. Mansell, and R. P. Cowburn, "Two-dimensional control of field-driven magnetic bubble movement using Dzyaloshinskii-Moriya interactions," *Applied Physics Letters*, vol. 106, no. 2, p. 022402, 2015. 16, 58, 75

[58] D. Lacour, M. Hehn, M. Alnot, F. Montaigne, F. Greullet, G. Lengaigne, O. Lenoble, S. Robert, and A. Schuhl, "Magnetic properties of postoxidized PtCoAl layers with perpendicular anisotropy," *Applied Physics Letters*, vol. 90, no. 19, p. 192506, 2007. 21

[59] W. J. Gong, W. Liu, X. H. Liu, S. Guo, J. N. Feng, B. Li, and Z. D. Zhang, "Tuning exchange bias in ferromagnetic/ferromagnetic/antiferromagnetic heterostructures [Pt/Co]/NiFe/NiO with in-plane and out-of-plane easy axes," *Journal of Applied Physics*, vol. 109, no. 4, p. 043906, 2011. 21

[60] M. Björck and G. Andersson, "GenX: an extensible X-ray reflectivity refinement program utilizing differential evolution," *Journal of Applied Crystallography*, vol. 40, pp. 1174–1178, 2007. 23

[61] Quantum Design, *Magnetic Property Measurement System SQUID VSM User Manual*. No. E0, San Diego: Quantum Design, Inc., e0 ed., 2010. 23

[62] L. Pickelmann, *Low voltage co-fired multilayer stacks , rings and chips for actuation*. Munich: Piezomechanik GmbH, 2012. 26

[63] Takuro Ikeda, *Fundamentals of Piezoelectricity*. Oxford: Oxford University Press, 1990. 26

[64] L. Pickelmann, *First Steps towards Piezoaction*. Munich: Piezomechanik GmbH, 2012. 26

[65] G. Kuczynski, "Effect of Elastic Strain on the Electrical Resistance of Metals," vol. 94, no. 1, pp. 61–64, 1954. 28

[66] J. Zhang, Y. Nagao, S. Kuwano, and Y. Ito, "Microstructure and temperature coefficient of resistance of platinum films," *Japanese Journal of Applied Physics*, vol. 36, no. Pt.1 No. 2, pp. 834–839, 1997. 30

[67] Y. Terada, K. Ohkubo, T. Mohri, and T. Suzuki, "Thermal conductivity in Pt-based alloys," *Journal of Alloys and Compounds*, vol. 285, pp. 233–237, 1999. 30

[68] E. H. Hall, "On a new Action of the Magnet on Electric Currents," *American Journal of Mathematics*, vol. 2, no. 3, pp. 287–292, 1879. 33

[69] E. H. Hall, "On the "rotational coefficient" in nickel and cobalt," *Philosophical Magazine Series 5*, vol. 12, no. 74, p. 157, 1881. 33

[70] D. P. Rosenblatt, M. Karpovski, and a. Gerber, "Monitoring magnetization reversal and perpendicular anisotropy by the extraordinary Hall effect and anisotropic magnetoresistance.," *Journal of Applied Physics*, vol. 108, no. 4, p. 043924, 2010. 33, 43

[71] N. Nagaosa, J. Sinova, S. Onoda, A. H. MacDonald, and N. P. Ong, "Anomalous Hall effect," *Reviews of Modern Physics*, vol. 82, no. April-June, pp. 1539–1592, 2010. 33, 34

[72] J. Kerr, "On rotation of the plane of polarization by reflection from the pole of a magnet," *Philosophical Magazine Series 5*, vol. 3, no. 19, pp. 321–343, 1877. 35

[73] M. Faraday, "On the magnetic affection of light, and on the distinction between the ferromagnetic and diamagnetic conditions of matter," *Philosophical Magazine Series 3*, vol. 29, no. 194, pp. 249–258, 1846. 35

[74] A. Hubert and R. Schäfer, *Magnetic Domains*. Berlin: Springer, 1998. 35, 36

[75] R. Schaefer, *Handbook of Magnetism and Advanced Magnetic Materials*. Wiley, 2007. 37

[76] J. A. Aboaf, S. R. Herd, and E. Klokholm, "Magnetic properties and structure of cobalt-platinum thin films," *IEEE Transactions on Magnetics*, vol. 19, no. 4, pp. 1514–1519, 1983. 49

[77] S. Pizzini, J. Vogel, S. Rohart, L. D. Buda-Prejbeanu, E. Jué, O. Boulle, I. M. Miron, C. K. Safeer, S. Auffret, G. Gaudin, and A. Thiaville, "Chirality-induced asymmetric magnetic nucleation in Pt/Co/AlOx ultrathin microstructures," *Physical Review Letters*, vol. 113, no. 4, p. 047203, 2014. 75

[78] M. Vanatka, J.-C. Rojas-Sanchez, J. Vogel, M. Bonfin, A. Thiaville, and S. Pizzini, "Velocity asymmetry of Dzyaloshinskii domain walls in the creep and flow regimes," *aXiv*, p. arXiv:1504.00933v1, 2015. 75

[79] E. Jué, C. K. Safeer, M. Drouard, A. Lopez, and P. Balint, "Chiral damping of magnetic domain walls," *arXiv*, p. 1504.04411v1, 2015.

[80] M. Weiler, A. Brandlmaier, S. Geprägs, M. Althammer, M. Opel, C. Bihler, H. Huebl, M. S. Brandt, R. Gross, and S. T. B. Goennenwein, "Voltage controlled inversion of magnetic anisotropy in a ferromagnetic thin film at room temperature," *New Journal of Physics*, vol. 11, no. 1, p. 013021, 2009. 82

[81] M. Liu, S. Li, Z. Zhou, S. Beguhn, J. Lou, F. Xu, T. Jian Lu, and N. X. Sun, "Electrically induced enormous magnetic anisotropy in Terfenol-D/lead zinc niobate-lead titanate multiferroic heterostructures," *Journal of Applied Physics*, vol. 112, no. 6, p. 063917, 2012.

[82] D. E. Parkes, S. A. Cavill, A. T. Hindmarch, P. Wadley, F. McGee, C. R. Staddon, K. W. Edmonds, R. P. Campion, B. L. Gallagher, and a. W. Rushforth, "Non-volatile voltage control of magnetization and magnetic domain walls in magnetostrictive epitaxial thin films," *Applied Physics Letters*, vol. 101, no. 7, p. 072402, 2012. 82, 95

[83] Y. T. Yang, Q. M. Zhang, D. H. Wang, Y. Q. Song, L. Y. Wang, L. Y. Lv, Q. Q. Cao, and Y. W. Du, "Electric field control of magnetic properties in CoPt/Pb(Mg1/3Nb2/3)O3-PbTiO3 heterostructure at room temperature," *Applied Physics Letters*, vol. 103, no. 8, p. 082404, 2013. 82, 89

[84] J.-W. Lee, S.-C. Shin, and S.-K. Kim, "Spin engineering of CoPd alloy films via the inverse piezoelectric effect," *Applied Physics Letters*, vol. 82, no. 15, p. 2458, 2003. 82, 89

[85] N. Lei, S. Park, P. Lecoeur, D. Ravelosona, C. Chappert, O. Stelmakhovych, and V. Holy, "Magnetization reversal assisted by the inverse piezoelectric effect in Co-Fe-B/ferroelectric multilayers," *Physical Review B*, vol. 84, no. 1, p. 012404, 2011. 89

[86] A. Schellekens, A. van den Brink, J. Franken, H. Swagten, and B. Koopmans, "Electric-field control of domain wall motion in perpendicularly magnetized materials," *Nature Communications*, vol. 3, p. 847, 2012. 96, 101

[87] A. Bernand-Mantel, L. Herrera-Diez, L. Ranno, S. Pizzini, J. Vogel, D. Givord, S. Auffret, O. Boulle, I. M. Miron, and G. Gaudin, "Electric-field control of domain wall nucleation and pinning in a metallic ferromagnet," *Applied Physics Letters*, vol. 102, no. 12, p. 122406, 2013. 96, 101

[88] U. Bauer, S. Emori, and G. S. D. Beach, "Voltage-gated modulation of domain wall creep dynamics in an ultrathin metallic ferromagnet," *Applied Physics Letters*, vol. 101, no. 17, p. 172403, 2012. 101

[89] Z. Huang, I. Stolichnov, a. Bernand-Mantel, J. Borrel, S. Auffret, G. Gaudin, O. Boulle, S. Pizzini, L. Ranno, L. Herrera Diez, and N. Setter, "Ferroelectric control of magnetic domains in ultra-thin cobalt layers," *Applied Physics Letters*, vol. 103, no. 22, p. 222902, 2013. 101